Disappearance of *Homo floresiensis* from Liang Bua alongside seasonal aridification of Flores 61,000-47,000 years ago

Michael K. Gagan[1,2,3,*], Linda K. Ayliffe[3], Nick Scroxton[3,4], Wahyoe S. Hantoro[5,2,1,†], Mika R. Puspaningrum[1,6], Gerrit D. van den Bergh[1], Heather Scott-Gagan[3], Scott A. Condie[7], R. Lawrence Edwards[8], Hai Cheng[9,10], Jian-xin Zhao[2], John C. Hellstrom[11], Alena K. Kimbrough[1,12], Matthew J. Gagan[13], Bambang W. Suwargadi[5], Joan A. Cowley[3], Bronwyn C. Dixon[3], Garry K. Smith[3], Neil Anderson[3,†], Henri Wong[14], Hamdi Rifai[15]

[1] Environmental Futures, School of Earth, Atmospheric and Life Sciences, University of Wollongong, Wollongong, NSW 2522, Australia

[2] School of the Environment, The University of Queensland, St Lucia, QLD 4072, Australia

[3] Research School of Earth Sciences, The Australian National University, Canberra, ACT 2601, Australia

[4] Irish Climate and Analysis Research Units, Department of Geography, Maynooth University, Maynooth, County Kildare, Irelend

[5] Research Center for Geotechnology, Indonesian Institute of Sciences (LIPI), Bandung 40135, Indonesia

[6] Palaeontology and Quaternary Geology Research Group, Bandung Institute of Technology, Bandung 40132, Indonesia

[7] CSIRO Oceans & Atmosphere, Hobart, TAS 7004, Australia

[8] Department of Earth and Environmental Sciences, University of Minnesota, Minneapolis, MN 55455, USA

[9] Institute of Global Environmental Change, Xi'an Jiatong University, Xi'an 710054, China

[10] State Key Laboratory of Loess and Quaternary Geology, Institute of Earth Environment, Chinese Academy of Sciences, Xi'an 710061, China

[11] School of Geography, Earth and Atmospheric Sciences, The University of Melbourne, Parkville, VIC 3010, Australia

[12] Securing Antarctica's Environmental Future, University of Wollongong, Wollongong, NSW 2522, Australia

[13] School of Electrical Engineering and Computer Science, The University of Queensland, St Lucia, QLD 4072, Australia

[14] Environmental Research and Technology Group, Australian Nuclear Science and Technology Organisation, Sydney, NSW 2234, Australia

[15] Department of Physics, Universitas Negeri Padang, Padang 25131, Indonesia

[†] Deceased

[*]Corresponding author: mgagan@uow.edu.au

Abstract

The cause of the disappearance of the primitive hominin, *Homo floresiensis*, from the Indonesian island of Flores ~50,000 years ago is a key question in palaeoanthropology. The potential roles of human agency and climate change continue to be debated, but the history of freshwater availability critical to survival at the type locality, Liang Bua, remains unknown. Although speleothem $\delta^{18}O$ is used widely as a proxy for monsoon rainfall, seasonal rainfall variations with contrasting $\delta^{18}O$ values can distort the record without altering mean annual rainfall. Here, we reconstruct summer and winter rainfall concurrent with *H. floresiensis* by combining speleothem Mg/Ca (a local rainfall proxy) with $\delta^{18}O$ (for rainfall seasonality). Geochemical modelling of the Mg-^{18}O system shows that *H. floresiensis* and its primary prey, *Stegodon*, experienced a protracted decline in mean annual rainfall from ~1,560 to 960 mm between 76,000 and 55,000 years ago. During the final occupation phase at Liang Bua 60,000–50,000 years ago, summer rainfall dropped to a record low of ~430 mm, indicative of limited recharge of river-bed watering points and dry-season water stress. These findings point to landscape aridification, and intensified human-faunal interaction around dwindling resources, as likely contributors to the abandonment of Liang Bua.

Introduction

In 2003, excavations in the Liang Bua rock shelter uncovered the skeletal remains of a previously unknown small-bodied hominin species, *Homo floresiensis*[1,2]. The *H. floresiensis* occupation interval was initially dated to 95–12 thousand years (ka) ago[2,3], raising the possibility of interaction with early modern humans (*Homo sapiens*) in Island Southeast Asia (ISEA), with implications for the extinction of the species. Following revisions to the site's stratigraphy and chronology, however, all *H. floresiensis* skeletal remains now date to 100–60 ka[4]. The associated stone artefact record and assemblage of large fauna typically found with *H. floresiensis* [*Stegodon florensis insularis* (pygmy elephant), *Leptoptilos robustus* (giant maribou stork), *Trigonoceps sp.* (vulture)] end at ~50 ka[5,6]. The revisions indicate that their disappearance from the record preceded modern human arrival at Liang Bua at ~46 ka, marked by a notable shift in the assemblage of raw materials for stone tool making[6]. Definitive evidence of a temporal overlap between modern humans and *H. floresiensis* elsewhere on Flores also is lacking, leaving compelling reasons to consider environmental change as a potential cause of the extirpation.

Freshwater availability is crucial for the survival of humans and large fauna[7,8]. The Liang Bua biome would have been shaped in part by the seasonally dry rainfall regime on Flores, and the timing and duration of the Indonesian-Australian summer monsoon. In particular, *S. florensis insularis*, the primary prey for *H. floresiensis,* weighed ~350–950 kg[5] and, like modern elephants, may have had limited tolerance for dry-season aridity[9]. At present, the Indo-Pacific Warm Pool (IPWP) drives deep atmospheric convection in ISEA and the seasonal distribution of rainfall is modulated by the latitudinal migration of the Intertropical Convergence Zone (ITCZ). About 60% of the mean annual rainfall (~1,400 mm) in the uplands around Liang Bua occurs during the austral summer (December–March) due to the northwest monsoon. The remainder falls during the dry season and two monsoon transition months (April and November), and is related to low-level south-easterly tradewinds and storms generated along the southern periphery of the ITCZ. Hydroclimate reconstructions covering the *H. floresiensis* occupation of Liang Bua indicate that past variations in sea level, insolation and inter-hemispheric temperature gradients had profound influences on regional rainfall[10–13]. Thus, the understanding of keystone fossil taxa discontinuities at Liang Bua requires the assessment of past rainfall and the shifting balance between wet-season and dry-season rainfall at the site.

Much of our current knowledge of the western Flores hydroclimate pertains to the last 50,000 years, and is derived from precisely dated speleothem oxygen-isotope ($\delta^{18}O$) records[14–17]. These highly resolved time series document rainfall $\delta^{18}O$ variability, providing insights into broad-scale monsoon circulation. In low-latitude Australasia, where rainfall patterns are bimodal, however, speleothem $\delta^{18}O$ alone generally cannot be used to definitively infer local rainfall amounts[18–21]. For example, on Flores changes in the relative proportions of convective summer rainfall and tradewind-associated winter rainfall, with contrasting $\delta^{18}O$ values[14,22], can affect speleothem $\delta^{18}O$ without altering the mean annual rainfall. Thus, a critical challenge is to elucidate the histories of both rainfall amount and rainfall seasonality specific to Liang Bua.

Tandem measurement of Mg/Ca and $\delta^{18}O$ in speleothems potentially enables the reconstruction of summer and winter rainfall patterns through time. In optimal karst settings, speleothem Mg/Ca can serve as an independent indicator of past changes in local monsoon rainfall[23–29]. Accumulating evidence shows that prior calcite precipitation (PCP) in karst void spaces, where CO_2 degassing occurs, can increase Mg/Ca in cave dripwaters due to preferential exclusion of Mg^{2+} during calcite formation[30–34]. Reduced rainfall and karst infiltration rates create

conditions favouring PCP, resulting in higher Mg/Ca in the speleothem 'downstream'. In principle, the differences between Mg/Ca and $\delta^{18}O$ records can be used to infer rainfall seasonality. We interpret these differences in terms of the mixing ratio of summer monsoon rainfall (lower $\delta^{18}O$) and winter tradewind rainfall (higher $\delta^{18}O$), which dictates the amount-weighted average speleothem $\delta^{18}O$[35,36]. Ideally, the tandem Mg-^{18}O method should expedite the reconstruction of local summer and winter rainfall amounts, even for tropical settings where annual rainfall and monsoon seasonality change in unexpected ways.

We validate this approach using high-resolution measurements of Mg/Ca and $\delta^{18}O$ for a precisely dated stalagmite from Liang Luar cave, in close proximity to Liang Bua (Fig. 1). Our aim was to construct a season-specific record of local rainfall amounts and monsoon seasonality for the period 91–47 ka, including the critical final phase of the *H. floresiensis* occupation of Liang Bua. This record reveals a progressive 38% reduction in mean annual rainfall from 76 to 55 ka accompanied by season-specific aridity; winter rainfall was 35% lower than at present from 68 to 64 ka, and peak summer aridity (51% lower than at present) occurred at 58–55 ka. The scale of change indicated by our rainfall estimates for Liang Luar agrees well with model simulations of past rainfall on Flores at glacial–interglacial and millennial scales[37,38]. These findings provide a sound scientific basis for the identification of climate change as a potential driver of the disappearance of *H. floresiensis* and *S. florensis insularis* from Liang Bua.

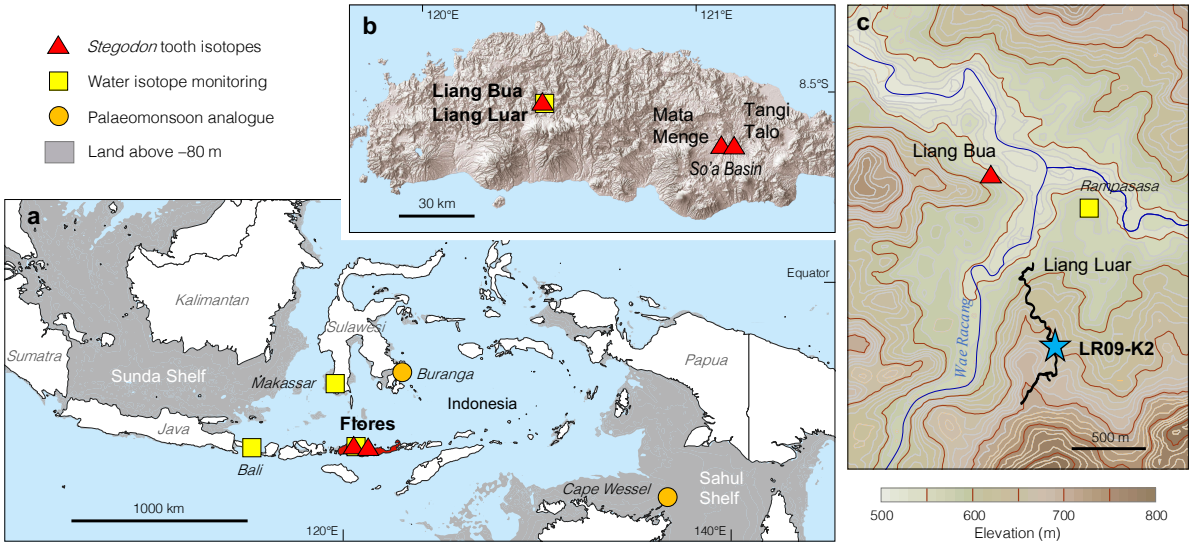

Fig. 1 | Physiographic attributes of the study area. a Location of the island of Flores, Indonesia. Grey shading shows land exposed above the present-day –80 m isobath at the sea-level lowstand around 65 ky BP. **b** Digital elevation map of western Flores with study site locations. **c** Topographic map showing the proximity of Liang Luar and Liang Bua in the Wae Racang river valley. Symbols indicate auxiliary datasets discussed in the text: archaeological sites with *Stegodon* tooth enamel isotope data (triangles); rainfall isotope monitoring sites (squares); and modern rainfall analogues for reconstructed changes in monsoon seasonality (circles). Base maps were created using QGIS software and the GEBCO23 grid[98].

Results

Liang Luar and stalagmite LR09-K2. The entrance to Liang Luar (8° 32' 10.1" S, 120° 26' 45.4" E; 570 m.a.s.l.) is only ~660 m from Liang Bua (8° 31' 50.4" S, 120° 26' 36.9" E; 560 m.a.s.l.). Both caves are situated within low hills of Late Miocene-Early Pliocene dolomitic limestone[39] adjacent to Late Pleistocene alluvial terraces of the Wae Racang river valley (Fig. 1). Stalagmite LR09-K2, the focus of this study, was discovered ~860 m in from the cave entrance as a result of mini-coring and uranium-thorium (U-Th) dating campaigns conducted in 2006 and 2007, and collected in 2009. The straight-line distance between Liang Bua and LR09-K2 is ~1.26 km. LR09-K2 is 1.54 m in length and composed of compact calcite (Supplementary Fig. 1). The chronology for the 50-year resolution Mg-^{18}O record is well constrained by 32 high-precision U-Th dates, with a median age uncertainty of ±0.29 ky (2σ). The record spans 91.4 to 46.8 thousand years before present (ky BP, Supplementary Fig. 2). Mg/Ca and $\delta^{18}O$ were measured on the same precisely dated sample aliquots, ensuring strict temporal alignment of the time series.

Fidelity of the Mg/Ca and $\delta^{18}O$ records. Figure 2 shows the Mg/Ca and $\delta^{18}O$ time series, corrected for the effect of terrestrial ice volume on seawater $\delta^{18}O$ ($\delta^{18}O_{iv}$; see Methods). In general, Mg/Ca and $\delta^{18}O_{iv}$ increased from 91 to 47 ky BP, with coeval maxima around 58–55 ky BP. At times, Mg/Ca and $\delta^{18}O_{iv}$ are tightly coupled, especially during abrupt millennial-scale shifts to lower values, and after ~60 ky BP. However, there are swings in $\delta^{18}O_{iv}$ without Mg/Ca counterparts. Most prominent are divergences to higher values from ~85 to 76 ky BP, and to lower values from ~68 to 62 ky BP. These signals are too large to be attributable to temperature effects on stalagmite Mg/Ca or $\delta^{18}O_{iv}$. For example, a 2–3°C cooling of IPWP sea-surface temperature (and hence tropical surface air temperature) during glacial times would decrease the stalagmite Mg/Ca by ~0.6 mmol/mol[40], negating only 4% of

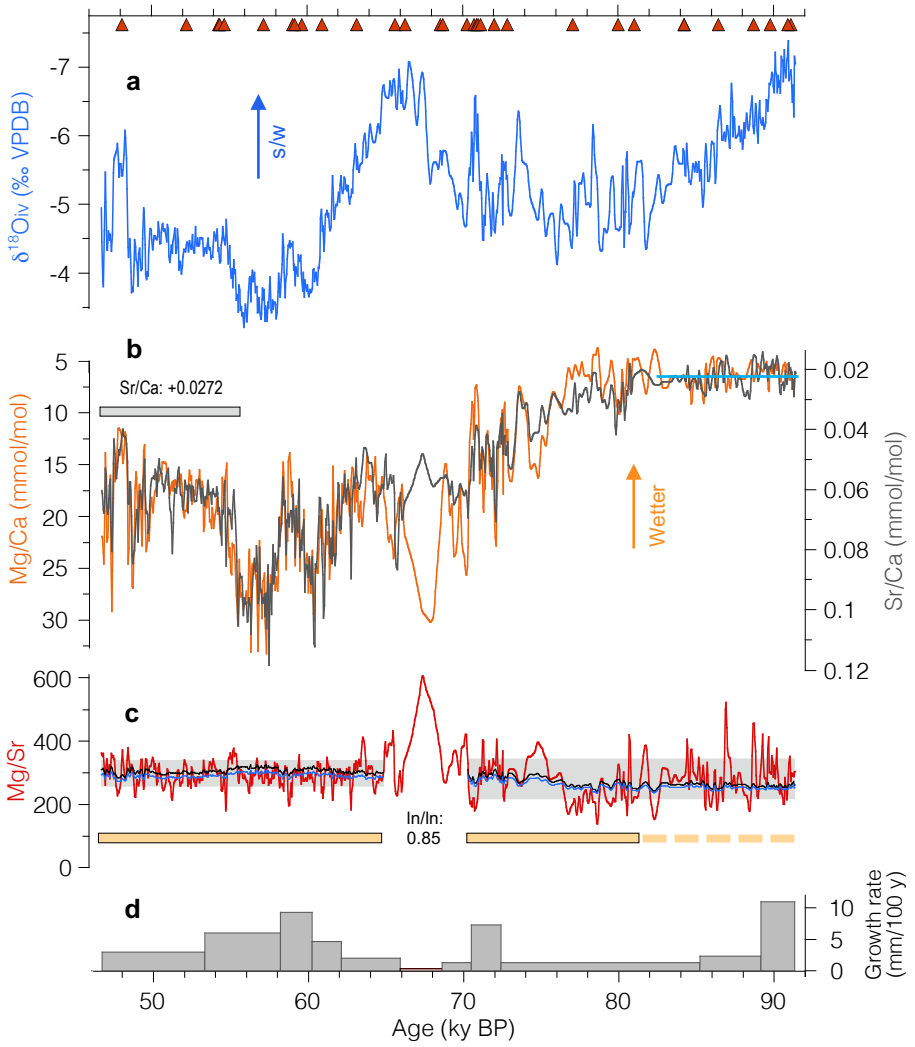

Fig. 2 | $\delta^{18}O$, Mg/Ca, Sr/Ca and PCP results for stalagmite LR09-K2. a $\delta^{18}O$ adjusted for the influence of ice volume-induced changes in the mean $\delta^{18}O$ of seawater ($\delta^{18}O_{iv}$; Methods, Supplementary Fig. 2). Triangles show U-Th dates. **b** Positive covariation between Mg/Ca (orange) and Sr/Ca (grey). The period of near-constant Mg/Ca and Sr/Ca (91.4–81.8 ky BP, blue line) marks stalagmite calcite deposition from dripwaters derived from bedrock (dolomitic limestone) near the onset of PCP. The Sr/Ca values for 55.5–46.8 ky BP have been adjusted by 0.0272 mmol/mol (to higher) to account for a slight offset between the Mg/Ca and Sr/Ca records (see Supplementary Figs. 3, 4). **c** Stalagmite Mg/Sr. Sections of the record with near-constant Mg/Sr (296 ± 37, 1σ; grey shading) are indicative of PCP[33]. The ln(Sr/Ca)/ln(Mg/Ca) slope of 0.85 for the record (excluding 70.3–64.9 ky BP) is diagnostic of PCP[32] (Supplementary Fig. 4). The black curve shows the best fit Mg/Sr profile produced by PCP at a ln/ln slope of 0.85, as determined by Rayleigh fractionation modelling (Supplementary Fig. 5). The blue curve shows the good agreement with Mg/Sr produced by the theoretical PCP ln/ln slope of 0.88 (ref.[32]). **d** Summary of stalagmite growth rates. The PCP signal is uninterrupted across a broad range of growth rates, but overprinted by anomalously high Mg/Sr associated with a slow-growth interval centred at 68.6–65.9 ky BP.

the ~15 mmol/mol increase observed from 76 to 55 ky BP. Additionally, the effects of temperature on $^{18}O/^{16}O$ fractionation in tropical rainfall and stalagmite calcite are in opposite directions, and similar in scale, thus they tend to cancel out[41].

Robust evidence for PCP in the stalagmite K2 record is an essential prerequisite for interpretation of the relationship between Mg/Ca and $\delta^{18}O_{iv}$. The PCP signature is governed by Rayleigh fractionation where Ca^{2+} decreases exponentially in solution relative to Mg^{2+} and Sr^{2+}due to Mg-Ca and Sr-Ca partition coefficients less than one[42]. The associated positive correlation between Mg/Ca and Sr/Ca is a fundamental property of PCP[32]. We used two diagnostic criteria to test for PCP: (1) the presence of positive covariation between Mg/Ca and Sr/Ca and near-constant Mg/Sr[33] and (2) linear correlation between ln(Sr/Ca) and ln(Mg/Ca) within a slope range of 0.88 ± 0.13 (ref.[32]).

The K2 record shows positive covariation and near-constant Mg/Sr, excepting a brief interval of slow growth with anomalously high Mg/Sr (and negative correlation) at 70.3–64.9 ky BP (Fig. 2). The good agreement of the observed ln(Sr/Ca) versus ln(Mg/Ca) slope for the K2 record (0.85, $R^2 = 0.89$) with the theoretical slope of 0.88 ± 0.13 confirms that the time series (without 70.3–64.9 ky BP) is governed by PCP (Supplementary Figs. 3, 4). Rayleigh fractionation modelling, based on the algorithm of Wassenberg et al.[34], further confirms that PCP is well developed in the K2 record; progressive removal of ~80% of Ca^{2+} from solution by PCP is required to produce the observed range in stalagmite Mg/Ca and Sr/Ca (Supplementary Note 1, Supplementary Fig. 5).

Liang Luar is also well suited for oxygen-isotope studies. The cave atmosphere is stabilised by narrow constrictions near its entrance and relative humidity near 100% (inactive surfaces are damp) minimises evaporative effects on stalagmite $\delta^{18}O$. Good replication of contemporaneous stalagmite $\delta^{18}O$ records for Liang Luar demonstrates the lack of karst controls[43] or in-cave effects, particularly PCP on the cave ceiling[44–46], on the $\delta^{18}O$ of infiltrating waters[14–17,47]. Supplementary Figure 2 illustrates the median difference for all 14 coeval stalagmite $\delta^{18}O$ records spanning the last 91 ky (0.09‰; range, 0.00–0.50‰). These differences are small in the context of the 3.5‰ $\delta^{18}O$ range in the K2 record. Further, good reproducibility can only be achieved through consistent recording of the amount-weighted mean annual $\delta^{18}O$ of effective rainfall. No significant difference was observed between the $\delta^{18}O$ values of Liang Luar drip sites and the amount-weighted averages of pool waters collected in May 2007 (–5.4 to –5.5‰ VSMOW, $n = 2$; –5.4 to –5.6‰ VSMOW, $n = 5$; respectively)[48]. Thus, the dripwater residence times in the ~50–60-m-thick bedrock cap above the deep cave interior appear to be sufficient for homogenisation of the seasonal contrast in rainfall $\delta^{18}O$ along flow pathways.

Empirical relationship between Mg/Ca and $\delta^{18}O_{iv}$. A key step in the interpretation of the stalagmite K2 Mg-^{18}O record is to establish the relationship between Mg/Ca, $\delta^{18}O_{iv}$ and rainfall. At Liang Luar, there is a marked difference of ~7‰ between the amount-weighted average $\delta^{18}O$ for convective summer monsoon rainfall (–9‰ VSMOW) and tradewind-associated dry-season rainfall (–2‰ VSMOW; Supplementary Figs. 6, 7). As dry-season rainfall in southern Indonesia has uniformly high $\delta^{18}O$[22] (Supplementary Note 2), we interpret periods of positive covariation between stalagmite Mg/Ca and $\delta^{18}O_{iv}$ in terms of changes in the fraction of low-$\delta^{18}O$ summer rainfall, which would drive PCP, Mg/Ca and $\delta^{18}O_{iv}$ in the same direction.

We optimised the relationship between Mg/Ca and $\delta^{18}O_{iv}$ in the K2 record over three intervals with consistent positive covariation: 91.4–89.6, 75.5–70.3 and 60.3–46.7 ky BP (Fig. 3). These intervals encompass a broad range of climates, including the Marine Isotope Stage 5 (MIS5) interglacial, the MIS4 penultimate glacial, and abrupt millennial-scale shifts during the MIS5/4 transition (75–70 ky BP) and MIS3 (59–47 ky BP). The best-fit log-linear relationship for these periods is $\delta^{18}O_{iv} = 4.822*\log_{10}(1000Mg/Ca) - 10.56$ ($R^2 = 0.91$). This Mg-^{18}O relationship is specific to stalagmite K2 given the spatial differences in bedrock Mg/Ca and Sr/Ca and flow paths with unique dripwater residence times, CO_2 degassing histories and solute compositions.

A fundamental finding from this analysis is that $\delta^{18}O_{iv}$ can be a reliable indicator of local rainfall. Thus, interpretations involving potential competing controls on rainfall $\delta^{18}O$ can be ruled out. Notably, the $\delta^{18}O_{iv}$ variability in the K2 record cannot be attributed to ‘upstream’ changes in evaporative source regions or the rain-out of ^{18}O from air masses en route to the cave site, as proposed for the Asian summer monsoon[49–51]. Instead, rainfall at Liang Luar is sustained primarily by moisture evaporated nearby from the warm Java and Timor seas[14,17], rather

than from distant sources. If rain-out were a dominant factor, the measured $\delta^{18}O_{iv}$ would reflect the integrated rainfall amount upstream of Liang Luar, with no clear counterpart signal in stalagmite Mg/Ca.

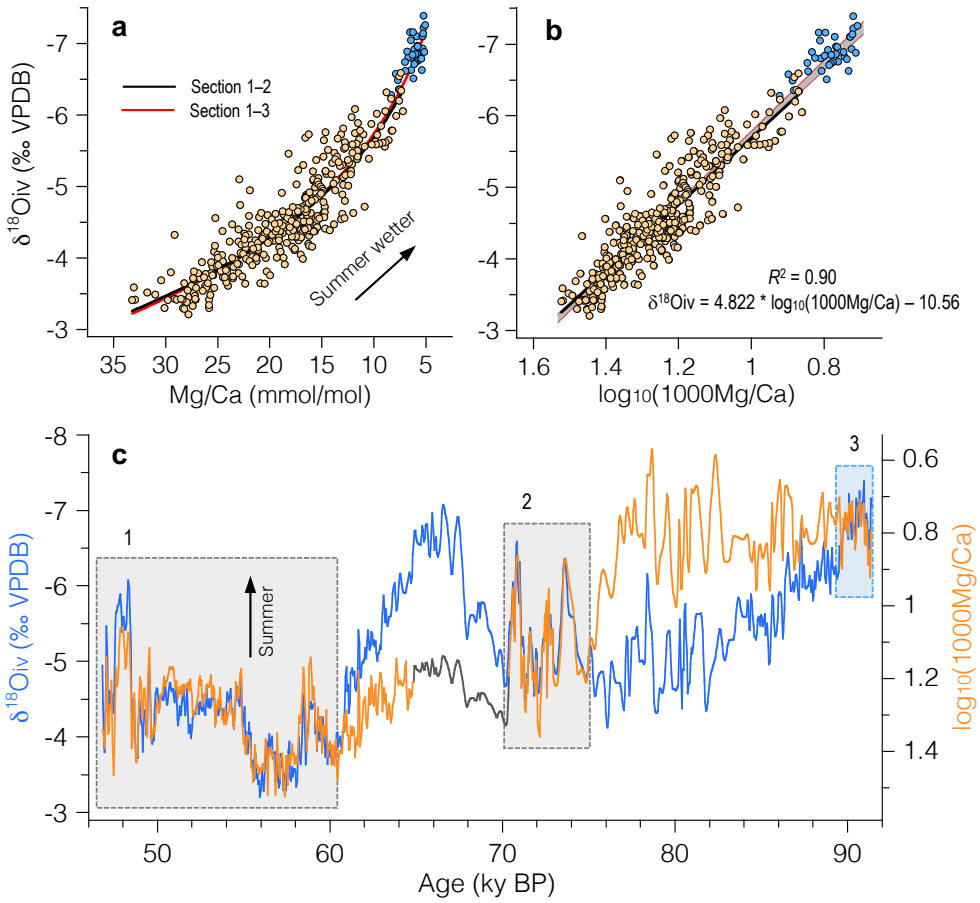

Fig. 3 | Mg/Ca and $\delta^{18}O_{iv}$ systematics for stalagmite LR09-K2. a Calibration of the exponential relationship between stalagmite Mg/Ca and $\delta^{18}O_{iv}$. The best fit is constrained by sections of the records with consistent positive covariation between Mg/Ca and $\delta^{18}O_{iv}$ (sections 1–3 in panel **c**) driven by the common effect of summer rainfall amount on PCP and $\delta^{18}O_{iv}$. **b** Log-linear transformation of the best fit for Mg/Ca and $\delta^{18}O_{iv}$. Colour-coded symbols show the good agreement of the best fits for sections 1–2 (millennial-scale variability, black line) and sections 1–3 (full data range; $R^2 = 0.90$, grey shows 95% confidence interval). **c** Best fit of $\log_{10}(1000Mg/Ca)$ and $\delta^{18}O_{iv}$ through time. The records have been aligned using the log-linear relationship: $\delta^{18}O_{iv} = 4.822*\log_{10}(1000Mg/Ca) - 10.56$. The grey curve shows calculated Mg/Ca values for the slow-growth interval (70.3–64.9 ky BP) overprinted by non-PCP processes (see Methods).

The systematic relationships among Mg/Ca, $\delta^{18}O_{iv}$ and local rainfall at Liang Luar provide insight into the nature of the 'amount effect', where the $\delta^{18}O$ of low-latitude rainfall is inversely related to rainfall amount[52]. Recent studies have shown that the $\delta^{18}O$ of rainfall in Australasia correlates positively with cloud-top temperature and outgoing longwave radiation at the top of the atmosphere, locally and regionally[53–55]. In this context, stronger monsoon moisture convergence and convective rainfall lead to higher cloud formations, and thus lower mean condensation temperatures for rainfall. Conversely, in winter, orographic rainfall and storms associated with low-level southeast tradewinds and local land breezes form at lower altitudes and higher condensation temperatures, resulting in less rainfall with higher $\delta^{18}O$[54,55]. In southern Indonesia, limited cloud heights in winter, together with isotopically uniform water vapour from the subtropical Timor Sea, make winter $\delta^{18}O$ less variable than in summer[22] (Supplementary Fig. 7). Thus, the observed connection between $\delta^{18}O_{iv}$ and the amount effect at Liang Luar likely reflects a lowering of rainfall $\delta^{18}O$ in summer due to well-organised convective systems associated with the ITCZ.

Precession modulation of rainfall seasonality and $\delta^{18}O_{iv}$. Important insights into monsoon seasonality can be gained at times when the stalagmite K2 Mg/Ca and $\delta^{18}O_{iv}$ proxies differ. Two distinct periods of divergence in the Mg-^{18}O record were identified; one centred at ~80 ky BP during the MIS5a interstadial and another at ~66 ky BP during the MIS4 glacial (Fig. 4). The anomalies are in opposite directions and driven primarily by swings in $\delta^{18}O_{iv}$. These excursions are separated by about half of a 23-ky orbital precession cycle, consistent with the interhemispheric response of speleothem $\delta^{18}O$ in Australasia to variations in summer insolation[11,17,35,56].

Traditionally, precession cyclicity in speleothem $\delta^{18}O$ records in monsoonal settings is attributed to summer rainfall[57]. Precession forcing of summer rainfall is evident in the K2 record, but it appears to have had little influence on the Mg/Ca record of the mean annual monsoon hydroclimate (Fig. 4). Instead, the Mg/Ca profile is

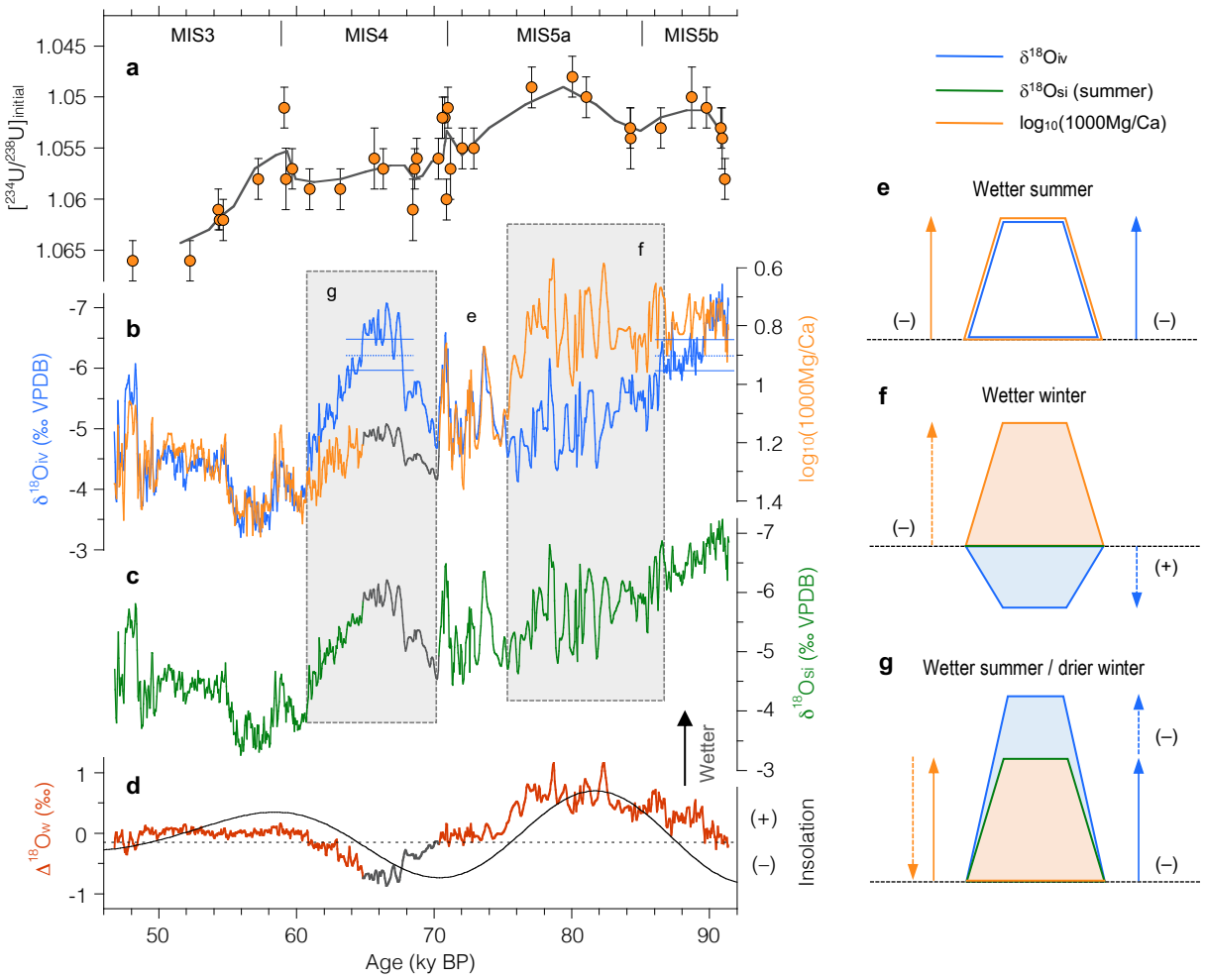

Fig. 4 | Effects of summer and winter rainfall on the LR09-K2 Mg-^{18}O record. a Stalagmite K2 initial $^{234}U/^{238}U$ activity ratios (with 2σ error bars) as indicators of groundwater residence time and karst dryness at Liang Luar (grey curve is the 3-pt running mean). **b** The K2 Mg-^{18}O record. Differences between the Mg/Ca and $\delta^{18}O_{iv}$ curves mark the opposing effects of changes in winter rainfall. Blue lines show the average $\delta^{18}O_{iv}$ (–6.2 ± 0.2‰, 2 SE) for the Common Era[17]. **c** $\delta^{18}O$ of the summer rainfall in-mixing component ($\delta^{18}O_{si}$) after accounting for the effects of winter rainfall on Mg/Ca and $\delta^{18}O_{iv}$ (Supplementary Note 3). **d** Effect of changes in winter rainfall on $\delta^{18}O_{iv}$ ($\Delta^{18}O_w = \delta^{18}O_{iv} - \delta^{18}O_{si}$). The black curve shows precession-scale changes in boreal summer insolation (June–August, 30°N), and the Asian summer monsoon[35,56], as a potential driver of changes in winter tradewind rainfall on Flores (see text). **e-g** Schematic examples of the effects of summer rainfall (solid arrows) and winter rainfall (dashed arrows) on Mg-^{18}O signals: positive covariation with wetter summer (**e**); negative covariation with wetter winter (MIS5a, **f**); and cancelling effect on Mg/Ca with combined effect on $\delta^{18}O_{iv}$ for equally wetter summer and drier winter (MIS4, **g**). Orange and blue shading shows the net effects of winter rainfall on Mg/Ca and $\delta^{18}O_{iv}$, respectively.

dominated by a long-term decline in rainfall from MIS5 to MIS3. Initial $^{234}U/^{238}U$ activity ratios $[^{234}U/^{238}U]_i$ calculated for the U-Th age determinations on stalagmite K2 confirm the decoupling of Mg/Ca from $\delta^{18}O_{iv}$. During drier periods, with reduced karst infiltration rates and longer seepage water residence times, $[^{234}U/^{238}U]_i$ can increase due to preferential leaching of ^{234}U from damaged crystal lattice sites in carbonate bedrock[58]. The positive covariation between stalagmite Mg/Ca and $[^{234}U/^{238}U]_i$ in the K2 record corroborates the drying trend.

The result suggests that the decoupling of Mg/Ca and $\delta^{18}O_{iv}$ is due to the influence of winter rainfall on stalagmite $\delta^{18}O_{iv}$. Gains or losses of winter rainfall, with higher $\delta^{18}O$, would produce opposing trends in the Mg/Ca and $\delta^{18}O_{iv}$ records (Fig. 4, Supplementary Note 3). Recent studies have shown that precession-scale variations of the Australian–Indonesian winter monsoon are in phase with the northern summer monsoon due to their linkage through cross-equatorial flow of surface winds[59–61]. Under this scenario, increased winter rainfall in Flores during MIS5a reflects enhanced moisture flux from the Australian high-pressure belt in response to higher northern summer insolation over the Asian landmass. Conversely, during MIS4, lower northern summer insolation would weaken the interhemispheric thermal contrast and cross-equatorial flow. Exposure of the Greater Australia (Sahul) continental shelf during the –80-m sea-level lowstand in MIS4[62] may have further reduced northward moisture transport from the Timor Sea and winter rainfall in Flores[37,63,64].

Figure 4 shows the decomposition of the K2 record into summer and winter rainfall components after accounting for the opposing effects of winter rainfall on Mg/Ca and $\delta^{18}O_{iv}$. The results indicate that shelf exposure played a key role in the reduction of mean annual and summer rainfall during glacial times, consistent with model studies of sea-level control on atmospheric convection in ISEA[37,64]. In contrast, precession forcing is most pronounced for winter rainfall at Liang Luar, and antiphased with modest precession effects in summer. The net effect of the antiphasing was to reduce rainfall seasonality at Liang Luar during MIS5a, and amplify it during MIS4.

Rainfall amount and palaeomonsoon seasonality. To translate the stalagmite K2 Mg-^{18}O record to rainfall amount, we developed a cave dripwater oxygen-isotope mixing model to determine the contributions of summer (December–March) and winter (April–November) rainfall to $\delta^{18}O_{iv}$ (Supplementary Note 3). The mass balance calculations show that the full range of $\delta^{18}O_{iv}$ in the K2 record can be described by altering the ratio of summer to winter rainfall in the cave dripwaters. Supplementary Figure 8 illustrates the effect of summer rainfall on stalagmite $\delta^{18}O_{iv}$. The modelled $\delta^{18}O$ of convective summer rainfall is allowed to vary systematically in accordance with the regional rainfall 'amount effect'[22]. The wetter interglacial end of the mixing model is scaled to the modern average stalagmite $\delta^{18}O_{iv}$ at Liang Luar (–6.2‰) when the annual fraction of summer rainfall is 62% (Supplementary Figs 2, 6). The $\delta^{18}O$ of non-convective rainfall (in both summer and winter) is set at the modern-day average of –2‰[14,22,55] (Supplementary Fig. 7).

With these boundary conditions in place, the 3.5‰ range in $\delta^{18}O_{iv}$ in the K2 record is accounted for by a conservative range in summer rainfall (44–68% of mean annual rainfall). The modelled range in the $\delta^{18}O$ of summer rainfall is –5.4‰ (MIS3) to –9.4‰ (MIS5b), well within the range at Liang Luar[14]. Furthermore, the 4‰ range is in good agreement with the range in stalagmite $\delta^{18}O_{iv}$ records spanning the last four glacial–interglacial transitions in south-western Sulawesi, near Flores, where $\delta^{18}O_{iv}$ is dictated almost entirely by summer rainfall[28,65]. The model also accounts for the effects of past changes in winter rainfall on stalagmite $\delta^{18}O_{iv}$. Supplementary Figures 9 and 10 illustrate the modelled proportions of winter and summer rainfall in cave dripwaters for periods when the Mg/Ca and $\delta^{18}O_{iv}$ records differ.

Supplementary Note 3 describes the scaling of stalagmite K2 Mg/Ca and $\delta^{18}O_{iv}$ to conservative estimates of annual mean, summer and winter rainfall. Briefly, the modern average stalagmite $\delta^{18}O_{iv}$ (–6.2‰) is set to modern rainfall seasonality at Liang Luar with annual, summer and winter rainfall amounts of 1,400, 870 (62%) and 530 mm, respectively. The lower limit for summer rainfall in the model (265 mm at $\delta^{18}O_{iv}$ = –2‰) occurs under conditions of no convective rainfall. The relationship between K2 stalagmite $\log_{10}(1000Mg/Ca)$ and $\delta^{18}O_{iv}$ defined here (Fig. 3) is used to scale Mg/Ca to mean annual rainfall at Liang Luar. Importantly, the calibrated Mg/Ca record is independent of oxygen-isotope seasonality, whereas $\delta^{18}O_{iv}$ is sensitive to changes in the proportions of summer and winter rainfall. The two relationships can be used to determine the combination of annual, summer and winter rainfall that is uniquely compatible with each Mg-^{18}O data pair in the K2 record (Supplementary Fig. 11).

Mean annual rainfall at Liang Luar declined 38% from 1,560 mm in MIS5 (91.4–76 ky BP ave.) to 960 mm at the onset of MIS3 (58–55 ky BP ave.) (Fig. 5). These amounts are 11% higher and 31% lower than at present. Summer rainfall declined 58‰ from a peak of 1,033 mm in MIS5b (91.4–89 ky BP ave.) to an average low of 429 mm during the dry 58–55 ky BP interval in MIS3 (51% lower than at present). This rainfall decline was punctuated by

abrupt increases in summer rainfall during cold Greenland stadials in the MIS5/4 interglacial-glacial transition (~75–70 ky BP), and prominent wet summers in MIS4 (68–64 ky BP). Rainfall during winter ranged from 809 mm in MIS5a (53% above modern at 83–76 ky BP) to 343 mm in MIS4 (35% below modern at 68–64 ky BP) in tandem with precession-forcing of the northern summer monsoon.

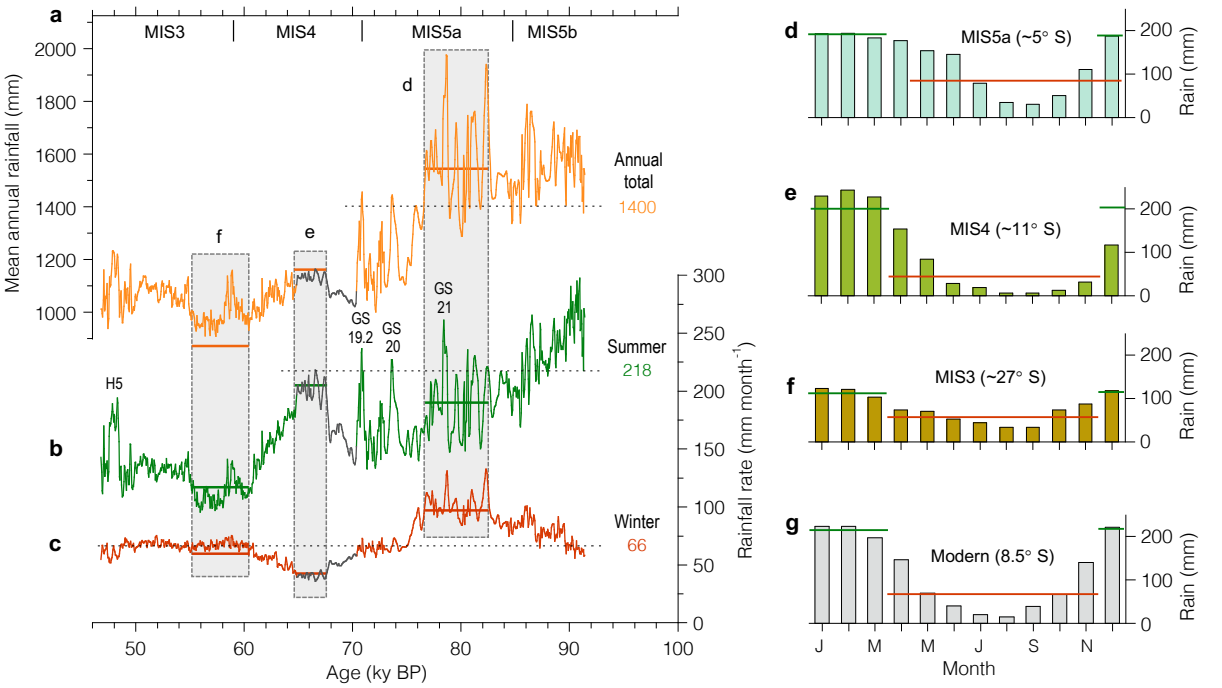

Fig. 5 | History of rainfall amount and seasonality at Liang Luar. a Modelled mean annual rainfall based on the LR09-K2 Mg/Ca record (Supplementary Note 3). **b** Modelled mean monthly rainfall rate for summer (December–March) after accounting for the effects of winter rainfall on Mg/Ca and $\delta^{18}O_{iv}$. **c** Modelled mean monthly rainfall rate for winter (April–November). Dashed lines show present-day (1998–2019 CE) average rainfall values at Liang Luar. GS and H indicate summer rainfall responses to Greenland stadials and Heinrich events. **d-g** Modern analogue rainfall records for past hydroclimate extremes at Liang Luar (grey shading in panels **a**–**c**). **d** Wet tropical Buranga, south-eastern Sulawesi (4.875° S, 122.875° E) with low seasonality (MIS5a). **e** Tropical savanna at Cape Wessel, east Arnhem Land, northern Australia (11.125° S, 136.625° E) with high seasonality (MIS4). **f** Subtropical uplands west of Brisbane, eastern Australia (27.625° S, 153.125° E) with low summer rainfall (onset of MIS3). **g** Modern rainfall at Liang Luar for reference (8.54° S, 12.45° E). Modern analogue averages for mean annual (orange lines), summer (green lines) and winter (dark-orange lines) rainfall are plotted against the proxy records on left (average absolute difference <5%). The best fits with the proxy records were determined using the Global Precipitation Climatology Center (GPCC) monthly rainfall data visualizer (version 2020) based on quality-controlled rain-gauge station records interpolated onto a 0.25° x 0.25° latitudinal-longitudinal grid[99].

The accuracy of the rainfall estimates can be validated with climate model simulations of rainfall seasonality during periods of lowered glacial sea levels and abrupt climate change[37,38]. The K2 record indicates reductions in summer and winter rainfall of –0.5 mm d^{-1} and –0.8 mm d^{-1}, relative to modern values, during the MIS4 glacial (Fig. 5). These values are consistent with the coupled Community Earth System Model version 1.2 (CESM1), which shows modest reductions in summer (December–February, –0.25 to –0.5 mm d^{-1}) and larger reductions in winter (April–November; –0.75 to –1.25 mm d^{-1}) on Flores during the Last Glacial Maximum[37]. Also, a recent transient simulation for Heinrich Stadial 1 (17.5–14.7 ky BP) performed with the CESM1 shows that the rainfall response on Flores was almost entirely restricted to summer[38]. Summer rainfall increased by 2–3 mm d^{-1}, which is essentially the same as the calculated summer increases for Greenland stadials 20 and 19.2 in the K2 record (2.4–2.6 mm d^{-1}).The calculated increase in summer rainfall for Heinrich Event 5 is somewhat smaller (1.6 mm d^{-1}). The data–model agreement confirms that our calculations provide realistic estimates of rainfall seasonality at Liang Luar on glacial–interglacial and millennial scales.

We use the difference between the mean monthly summer and winter rainfall rates (divided by the mean annual rainfall rate)[66] as a simple index of past rainfall seasonality at Liang Luar. The index reflects the combined effects of changes in seasonality (summer versus winter) and mean annual rainfall. The modern-day seasonality value for Liang Luar is 1.3. The stalagmite K2 record yields a wide range of values, with the lowest seasonality during the relatively wet MIS5a (0.65 at 82–76 ky BP, 50% below modern) and the highest seasonality during MIS4 (1.7 at 68–64 ky BP, 31% above modern). To put these results into context, the relatively wet MIS5a, with low seasonality, is akin to the modern-day rainfall pattern in south-eastern Sulawesi, north of Flores, with a relatively high proportion of winter rainfall (Fig. 5). In contrast, the distinctly seasonal climate during MIS4 is akin to monsoonal savanna settings with prolonged dry seasons in subtropical northern Australia. The driest interval, 58–55 ky BP, with exceptionally low summer rainfall, is similar to humid subtropical settings adjacent to the east coast of Australia at the southernmost margin of the Australian summer monsoon.

Discussion

Homo floresiensis and *Stegodon* coexisted on Flores for at least one million years based on the combined fossil record from Liang Bua and from the So'a Basin, ~80 km east of Liang Bua[67–70]. There are two well-documented faunal turnover events. At Tangi Talo, the oldest fossil site in the So'a Basin, the disappearance of *S. sondaari* at ~1,270 ka predates stone artefact evidence of a hominin presence by ~250,000 years[69]. At three younger sites in the basin, Kobatuwa and two fossil-bearing levels at Mata Menge, hominins coexisted with *S. florensis* from ~900 to 700 ka. The second turnover event is the disappearance of *S. florensis insularis* from Liang Bua at ~50 ka, which represents the last known co-occurrence of *H. floresiensis* and *Stegodon* on Flores[4–6]. The only evidence for hominin subsistence strategies, such as hunting or scavenging, is at Liang Bua in the form of butchery marks on juvenile *Stegodon* remains[5]. Notably, the *Stegodon* fossil assemblages at Liang Bua and Tangi Talo both largely represent juvenile individuals (86–94%)[5,69], but the bias at Tangi Talo cannot be due to selective predation by hominins[69]. At the lower Mata Menge level (~770 ka), with a hominin presence, the age profile of the *Stegodon* death assemblage resembles a living population, indicative of a mass-death environmental event. Thus, non-human causes of *Stegodon* mortality on Flores, such as reduced water availability and catastrophic volcanic events, need to be considered.

A consistent pattern of declining rainfall and freshwater availability led into the last appearances of *H. floresiensis* and *Stegodon* at Tangi Talo (~1,270 ka), Mata Menge (~700 ka) and Liang Bua (~50 ka) (Fig. 6). The results are based on analysis of $\delta^{18}O$ in fossil *Stegodon* tooth enamel from the three sites[67,69,71] (see Methods), and the stalagmite K2 record. The enamel $\delta^{18}O$ reflects the mean annual $\delta^{18}O$ of the animals' drinking water, which in turn reflects the site-specific $\delta^{18}O$ of precipitation, modified by surface evaporation[72–74]. The *Stegodon* enamel from the terminal occupations of Tangi Talo and Mata Menge shows significant increases in $\delta^{18}O$ (1.3–1.9‰) relative to stratigraphically older material. A similar shift to higher $\delta^{18}O$ in the stalagmite K2 record (1.6‰) leads into the terminal phase of *H. floresiensis* and *Stegodon* coexistence at Liang Bua. Additionally, tandem measurements of $\delta^{13}C$ in the same tooth samples reveal no flexibility in *Stegodon* feeding behaviour in response to climate change[67,69,71] (Fig. 6). In the So'a Basin, *S. sondaari* continued its preference for a mixture of leafy C_3 plants and C_4 grasses, and *S. florensis* specialised in C_4 grazing. *S. florensis insularis* at Liang Bua was also a C_4 grazer.

The new stalagmite Mg-^{18}O record provides a precisely dated chronological framework for examining the disappearance of *H. floresiensis* and *Stegodon* at Liang Bua alongside major climate change. Fossil evidence places modern humans (*H. sapiens*) on a southern dispersal route from continental Asia (Sunda) by ~75–63 ka[75], with initial arrival on Sahul by ~70–60 ka[76]. The eastward dispersal trajectory is aligned with the Lesser Sunda island chain, including Flores, potentially leaving time for modern human impacts at Liang Bua through hunting or habitat alteration[77–79]. However, the earliest signs of modern humans on Flores date to ~46 ka[4]. Thus, while modern human agency cannot be ruled out entirely, environmental change and/or hominin-faunal interactions may have contributed to the extirpations.

Analysis of numerous *Stegodon* remains at Liang Bua indicates that *H. floresiensis* subsisted to some extent by hunting or scavenging juveniles in particular[5]. Dry-season access to surface water would have been critical to the survival of coexisting hominins and stegodonts, as predominant to obligate drinkers like modern humans and proboscideans[80]. The vulnerability of proboscideans, as megaherbivores, to past hydroclimate change is well documented[9]. In monsoonal settings, groundwater recharge in hard-rock aquifers and river base-level flows are mainly fed by summer rainfall[81]. However, even in the current climate at Liang Bua, the base-level flow in the small rainfall catchment of the Wae Racang river does not persist year-round in drier years. Therefore, water-dependent stegodonts may have been vulnerable to hunting near critical dry-season water sources.

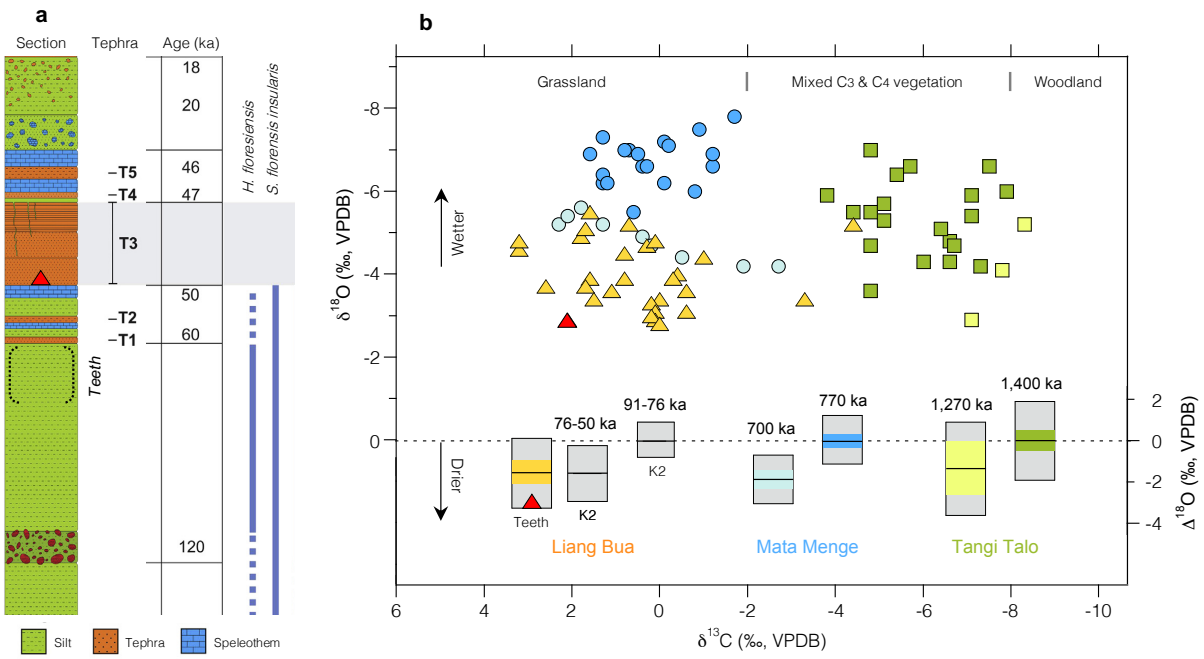

Fig. 6 | $\delta^{18}O$ and $\delta^{13}C$ in fossil *Stegodon* tooth enamel from the So'a Basin and Liang Bua. a Partial stratigraphic summary for Liang Bua with approximate ages (after Sutikna et al.[4,6]). Dashed brackets indicate the approximate position of *S. florensis insularis* tooth samples used for isotope analysis, mostly within the fossil-rich layer below volcanic tephra T1[5,6]. The red triangle represents a *S. florensis insularis* tooth sample excavated from T3[71] marking the termination of *H. floresiensis*. **b** Mean $\delta^{18}O$ and $\delta^{13}C$ of the carbonate phase in *Stegodon* tooth enamel excavated at Tangi Talo and Mata Menge in the So'a Basin, and at Liang Bua[67,69,71]. Approximate environmental boundaries for palaeovegetation diet types (based on analysis of tooth enamel $\delta^{13}C$) are shown at the top. *S. florensis insularis* was primarily a C_4 grazer at Liang Bua. Boxplots show the relative differences in tooth enamel $\delta^{18}O$ between the older and younger stratigraphic phases of *S. sondaari* (~1,400–1,270 ka) and *S. florensis* (~770–700 ka). The similar difference between the wetter and drier phases in the stalagmite K2 $\delta^{18}O$ record (not corrected for the ice-volume effect) is shown for reference. The range of the tooth enamel $\delta^{18}O$ data for *S. florensis insularis* is shown relative to the K2 data for 76–50 ka. Grey shading is the 2σ range. Non-overlapping means (black lines) with colour-coded 95% confidence envelopes (±2 SE) show significant increases in $\delta^{18}O$ (1.3–1.9‰) leading into each disappearance, suggesting a role for landscape aridification.

The stalagmite K2 Mg-^{18}O evidence for record low summer rainfall during the terminal phase of *H. floresiensis* and *Stegodon* coexistence at Liang Bua provides a measure of surface water transience, and thus the potential for interaction around dwindling river base-flow sources. The K2 palaeomonsoon reconstruction reveals three season-specific hydroclimates with implications for surface-water availability (Fig. 7). During Phase 1 (92–76 ky BP), mean annual rainfall was higher than at present and seasonality was low. Using the current climate as a guide, the favourable MIS5 rainfall regime would have sustained perennial base-flow in the Wae Racang river. This is consistent with stratigraphic indicators[82] and the murine rodent fossil assemblage[83] at Liang Bua, both of which reflect relatively wet, forested conditions at this time, thus freshwater availability was likely unconstrained.

The switch to Phase 2 (76–61 ky BP) marked by falling sea-levels and drier conditions was punctuated by abrupt increases in summer rainfall at 74, 71 and ~68–62 ky BP during cold Greenland stadials and MIS4. Exceptionally high rainfall seasonality and dry-season aridity at ~68–62 ky BP may have promoted the development of 'sub-tropical' open-grazing habitats supporting *S. florensis insularis*. The fossil record at Liang Bua supports this; the rodent assemblage shows a significant increase in open-habitat adapted species around 69–62 ka[83], and the concentration of *H. floresiensis* and *Stegodon* remains peaks at ~74–61 ka[4–6,82]. The results are consistent with the possibility that *H. floresiensis* and *Stegodon* were compromised by dry-season water stress, with intensified interaction as they aggregated near restricted, but still reliable, river-bed water resources fed by high summer rainfall.

Phase 3 (61–47 ky BP) encompasses the relatively dry MIS3 onset and lowest mean annual and summer rainfall on record (58–55 ky BP). An abrupt change in the rodent size distribution at Liang Bua around 60 ka indicates a return to more closed habitats[83], consistent with a return to lower rainfall seasonality. However, unlike Phase 2, persistently low summer rainfall likely led to critically low river base flows and challenging conditions for both species. The stalagmite K2 [$^{234}U/^{238}U]_i$ and Mg/Sr records of groundwater residence time reflect the impact of aridity, with increases to record highs starting at ~55 ky BP, during the final occupation phase (Fig. 7). The cumulative effects of landscape aridification and intensified human-faunal interaction around dwindling resources may have ultimately led to site abandonment.

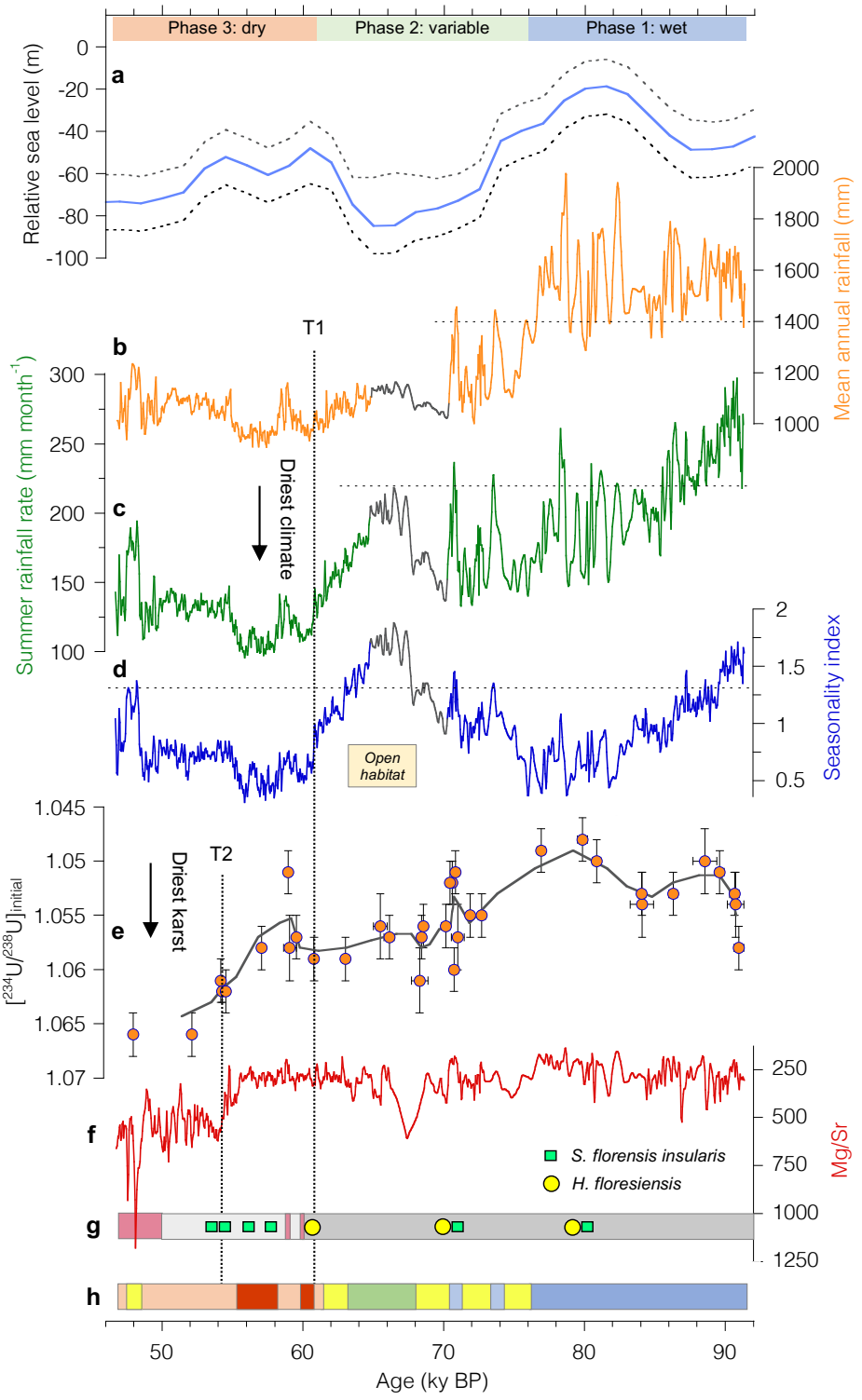

Fig. 7 | Chronology of climate change and *H. floresiensis* at Liang Bua. a For reference, relative sea level and the associated confidence interval, as determined by Waelbroeck et al.[94]. **b** Mean annual rainfall at Liang Bua based on the LR09-K2 Mg/Ca record. **c** Mean monthly rainfall rate for summer (December–March). **d** Monsoon seasonality index based on average rainfall rates for summer versus winter (April–November). Yellow box marks the 68–62 ky BP interval with strong seasonality, open habitat[83] and intensive use of Liang Bua[5,6]. Dashed lines in **b**–**d** indicate average climatic values at present (1998–2019 CE). **e** K2 $[^{234}U/^{238}U]_i$ values (with 2σ error bars) as indicators of groundwater residence time and karst dryness (grey curve is the 3-pt running mean). **f** K2 Mg/Sr showing a step-change decrease in Sr around 54 ky BP due to non-PCP processes. **g** Chronology of *H. floresiensis* and *S. florensis insularis* at Liang Bua[4]. The grey bar shows the occupation period and average ages for three U-Th dated *H. floresiensis* bones (yellow dots). The pale grey bar indicates the terminal occupation period (~60–50 ky BP) with associated stone artefacts and U-Th dated *S. florensis insularis* remains (green squares indicate average ages). The pink bars mark the approximate ages of volcanic tephra layers in the stratigraphic sequence. **h** Schematic summary of dry-season water stress at Liang Bua (blue = lowest stress, red = highest stress). Coloured bars at the top of the figure mark three associated climate phases: (1) wet with low seasonality (91–76 ky BP); (2) variable with dry-season aridity (76–61 ky BP); and (3) year-round dryness (61–49 ky BP). T1 marks a step-change into the driest interval on record (~61–55 ky BP). T2 marks step-change increases in $[^{234}U/^{238}U]_i$ and Mg/Sr (*y* axes reversed) during the terminal phase of *H. floresiensis* and *S. florensis insularis*.

The final disappearance of *H. floresiensis* and *Stegodon* from the Liang Bua stratigraphic succession is capped by a ~0.75-m-thick volcanic tephra layer (T3) dating to ~50–47 ka[4] (Fig. 6). Thus, local volcanism, and perhaps water supply contamination, may have further motivated site abandonement[6]. However, there is no unusual change in the stalagmite K2 Mg-^{18}O relationship around 50–47 ky BP, thus the environmental impact of T3 was limited on the decadal scale. But the step-changes to higher $[^{234}U/^{238}U]_i$ and Mg/Sr around 54 ky BP require further investigation. These shifts fall within the time interval encompassing five tephra layers (T1–T5) at Liang Bua, beginning around 60 ka[4], and may signal a more persistent presence of volcanic ash after 54 ky BP.

Our findings point to climate change, possibly in synergistic combination with predator-prey behaviour, as a likely contributor to the disappearance of *H. floresiensis* and *Stegodon* at Liang Bua. One scenario is that dry-season water stress forced *Stegodon* to relocate to better-watered habitats[84], and potentially *H. floresiensis* in search of its preferred prey. On the other hand, if *H. floresiensis* and *Stegodon* were both compromised by climate-induced water stress, even low intensity hunting could have triggered a critical population decline[8,85]. Thus, the final reduction in the species' numbers at Liang Bua after ~60 ka may reflect inexorable over-hunting of *Stegodon* and the migration of *H. floresiensis* to more favourable habitats. Whether *H. floresiensis* and *Stegodon* interacted with modern humans elsewhere on Flores remains uncertain. Our precisely dated rainfall record establishes a firm environmental framework for future research to examine the extinctions of these iconic species in the context of major climate change.

Methods

^{230}Th dating and age model. Reconnaissance ^{230}Th dating of mini-cores extracted discretely from the bases and tops of Liang Luar stalagmites *in situ* was performed at the University of Queensland, Australia, before we collected LR09-K2. This was done to optimise the age-range of the specimens while minimising the number collected. The LR09-K2 chronology is based on 32 ^{230}Th dates determined by multi-collector inductively coupled plasma mass spectrometry (MC-ICP-MS) at the University of Minnesota, USA and the University of Melbourne, Australia (Supplementary Table 1). Solid samples for dating were extracted adjacent to the Mg-^{18}O sampling track along the main growth axis of LR09-K2 using a small, diamond-coated circular-saw blade fitted to an air drill. The calcite blocks, weighing 190–300 mg, were dissolved and equilibrated with a mixed ^{229}Th–^{233}U–^{236}U tracer before U and Th were chemically separated and purified[86]. The MC-ICP-MS analytical procedures performed in the two laboratories are broadly similar[87,88] and yielded consistent results. ^{230}Th ages were calculated using the half-lives for ^{234}U (245,620 ± 70 years) and ^{230}Th (75,584 ± 30 years) determined by Cheng et al.[88], and converted to ky BP (with 'present' being 1950 CE).

As all of the samples have high ^{230}Th /^{232}Th values, the effect of detrital ^{230}Th on the calculated ages is very small. We determined corrected ^{230}Th ages using the bulk Earth ^{230}Th/^{232}Th activity ratio of 0.82, with an arbitrary uncertainty of 50%. The median age adjustment is 10 years to younger. Application of a large ^{230}Th/^{232}Th activity ratio of 7 ± 2, the maximum used in previous studies of Liang Luar material[14,16,17], shifted the median age by only

87 years to younger. The corrected ^{230}Th ages from both laboratories have a fully propagated 2σ median uncertainty of ±287 years.

The age-depth model for the LR09-K2 record was calculated using the OxCal (version 4.3) module, a Bayesian chronological modelling tool that employs Markov chain Monte Carlo[89,90]. Three of the 35 available ^{230}Th ages (LR09-K2-05, LR09-K2-M9, LR09-K2-M19) were slightly inconsistent with the age-depth trend defined by surrounding dates, and were excluded from the age model (Supplementary Fig. 1, Supplementary Table 1). The ages of five sample pairs analysed in the two laboratories agree within measurement uncertainty and were averaged into single age determinations, leaving a total of 27 precise control points to anchor the age model.

OxCal accounts for the non-uniform nature of stalagmite growth between ^{230}Th age control points using a P-sequence Poisson-process depositional model. The model was run with a prior outlier probability of 0.05 using *ko* = 1 mm^{-1}, *k* = 0.06 mm^{-1} and *U*(2,2). The interpolation rate value (*ko*) determines the rigidity of the model and enables trade-off between less interpolated age uncertainty (high *ko*, high rigidity) and stricter adherence to ^{230}Th ages (low *ko*, low rigidity). As a *ko* value of 1 mm^{-1} gives a relatively flexible age model, we consider the confidence envelope to be highly conservative. The age–depth model was interpolated linearly to the depths of individual isotope measurements.

Oxygen isotope analysis. In preparation for δ^{18}O analysis, the 1.54-m-long stalagmite LR09-K2 was cut into manageable 300–400 mm sections at 45° angles perpendicular to the intended sampling slab (Supplementary Fig. 1). Contiguous 20-mm-thick slabs were then cut using a water-cooled diamond saw. The slabs were polished, and sampling transects were positioned on the central growth axis and offset slightly across each 45° cut to ensure temporal overlap and time-series continuity. Powder samples for δ^{18}O analysis were then milled in a pre-cleaned narrow groove (1-mm depth and width). Sampling was continuous to simplify recovery of the milled powder and prevent aliasing in the record.

The average growth rate for LR09-K2 from 91.4 to 46.8 ky BP is 3.45 mm/100 years, based on the OxCal age model. The sampling interval was set at 1.5 mm, which yielded an average age resolution of 43 years (10–90% quantile range = 10–72 years) for a total of 1,026 δ^{18}O determinations. Sub-samples of the calcite powders were weighed to 180–220 µg and analysed for δ^{18}O at the Research School of Earth Sciences, ANU on a Finnigan MAT-251 dual-inlet mass spectrometer equipped with an automated Kiel I carbonate reaction device. CO_2 was liberated for isotopic analysis by reaction under vacuum with anhydrous 105% H_3PO_4 at 90°C. The results were normalised to the Vienna Peedee Belemnite (VPDB) scale such that in-run measurements on the NBS-19 and NBS-18 standards yielded values of −2.20‰ and −23.0‰ for δ^{18}O, respectively. The original delta values for NBS-19 and NBS-18 were used to maintain the consistency of results through time in the, RSES, ANU Stable Isotope Facility. The analytical precision (2σ) for 232 in-run measurements of δ^{18}O on the primary standard, NBS-19, was ±0.08‰.

Thirty-eight additional samples were milled continuously at higher resolution (0.4–0.5 mm) to obtain an age resolution of ~83 years (versus ~276 years) across a slow-growing (0.37 mm/100 years) section of LR09-K2 spanning 68.79–65.64 ky BP. A sideways clear-cut was made at each increment to remove overlap caused by the curvature of the 1-mm-diameter end-mill bit. These sub-samples were weighed to 110–160 µg and analysed for δ^{18}O at RSES, ANU on a Thermo MAT-253 mass spectrometer coupled to a Kiel IV carbonate device operating at 70°C. The analytical precision (2σ) for 12 in-run measurements of δ^{18}O on NBS-19 was ±0.10‰. The mean δ^{18}O value for coeval data produced by the MAT-251 and MAT-253 is in excellent agreement (MAT-253 is only 0.03‰ lower). Based on this result, the 38 high-resolution data points were substituted into the time series at 68.79–65.64 ky BP.

Mg/Ca and Sr/Ca analysis. Mg/Ca and Sr/Ca were measured on splits of the sample powders analysed for δ^{18}O using simultaneous inductively coupled plasma atomic emission spectrophotometry (ICP-AES; Varian Vista) at RSES, ANU and the Australian Nuclear Science and Technology Organisation (ANSTO). At ANU, 258 initial measurements on every fourth sample in the record were made following the reference solution data normalisation procedure of Schrag[91]. Then, 639 measurements were made at ANSTO following the intensity ratio calibration method of de Villiers et al.[92]. The resulting dataset provides full resolution of the millennial variability from 84 to 46.8 ky BP. Every second sample was measured in the relatively fast-growing section of LR09-K2 predating 84 ky BP.

At ANU, sample aliquots weighing ~0.5 mg were transferred to acid-washed vials and dissolved in 5 mL of 2% (v/v) HNO_3 to yield a consistent Ca concentration of 39 ± 5 ppm (2σ). One blank vial with 2% HNO_3 was analysed

at the start of each sample batch. Measurement of a Ca matrix-matched 'bracketing' reference solution in 2% HNO_3 was performed to standardise the Mg/Ca and Sr/Ca of each sample sequentially[91]. The elemental ratios of the reference (Mg/Ca = 5.754 mmol/mol, Sr/Ca = 8.983 mmol/mol) were determined by thermal ionisation mass spectrometry at RSES, ANU. The median standard error of the means for the reference solution pairs (n = 258) bracketing the samples was 0.004 mmol/mol for Mg/Ca and 0.0033 mmol/mol for Sr/Ca. Ten replicate measurements were made on each sample solution and the normalised (blank-corrected) averages are reported for the result.

At ANSTO, ~1 mg sample aliquots were dissolved in 5 mL of 3% (v/v) Merck Suprapure HNO_3 to yield a consistent Ca concentration of 76 ± 6 ppm (2σ). Four blank vials with 3% HNO_3 were analysed at the start of each sample batch, and a Ca matrix-matched reference solution was run between blocks of five samples to correct for any instrument drift. The in-run precision (1σ) for 132 corrected measurements of the reference Mg/Ca (19.992 mmol/mol) and Sr/Ca (0.1025 mmol/mol) was 0.040 mmol/mol (0.20%, RSD) and 0.0003 mmol/mol (0.30%, RSD), respectively. To ensure accuracy, in-run measurements were performed on three Ca matrix-matched standard solutions prepared gravimetrically from certified single-element National Institute of Standards and Technology (NIST) reference materials. The solutions covered the range of values in stalagmite LR09-K2 (Mg/Ca, 4–30 mmol/mol; Sr/Ca, 0.07–0.5 mmol/mol). The results were calculated by regressing the measured ICP-AES Mg/Ca and Sr/Ca intensity ratios (corrected for blank intensity) against the Mg/Ca and Sr/Ca (mmol/mol) of the standard solutions[92].

Agreement between the two laboratories is excellent for Mg/Ca (the primary element of interest): in-run measurements on the JCp-1 standard yielded average Mg/Ca values of 4.248 mmol/mol (ANU) and 4.246 mmol/mol (ANSTO), both within the 1σ uncertainty of the certified value (4.199 ± 0.065 mmol/mol, ref.[93]). However, the average Sr/Ca value of the ANU data is consistently offset by 0.0307 mmol/mol (39%) to higher relative to the fully calibrated ANSTO data. The Sr concentration of the ANU 'coral' reference solution bracketing each sample is ~180 times higher than that for the stalagmite K2 calcite samples, thus the instrument rinse time was probably too brief to clear the ICP spray chamber of Sr prior to the onset of each low-Sr sample measurement. Nevertheless, the offset between datasets is remarkably consistent, and our 0.0307-mmol/mol adjustment of the ANU dataset (to lower) produced excellent fine-scale agreement.

Data refinement. To compare the stalagmite trace element and $\delta^{18}O$ time series, the datasets were binned at 50-year resolution. Prior to binning, the data were interpolated at 1-year resolution in MATLAB using a piece-wise cubic Hermite spline, creating a weighted average throughout each 50-year bin to ensure equal representation of data points. The 1-year data were averaged to the mid-point of each 50-year bin and then adjusted to account for changes in the mean $\delta^{18}O$ of seawater due to changes in terrestrial ice-volume. We use the global ocean $\delta^{18}O$ reconstruction based on a composite benthic foraminiferal $\delta^{18}O$ record corrected for changes in deep-ocean temperature[94], with a 0.085‰ change in seawater $\delta^{18}O$ equating to 10 m sea level. The 1,500-year resolution ocean $\delta^{18}O$ record was interpolated into 50-year bins and smoothed with a 1,550-year moving average (50-year steps) prior to the adjustment.

In Figure 2, the Sr/Ca data for 55.5–46.8 ky BP have been adjusted by 0.0272 mmol/mol to higher to account for a consistent offset relative to Mg/Ca. This interval shows good evidence for PCP (near-constant Mg/Sr; ln/ln slope 0.84; Supplementary Figs. 3, 4). A switch to prior aragonite precipitation due to aridity (and high Mg/Ca in dripwaters) around 55.5 ky BP would decrease Sr/Ca, but with negative covariation with Mg/Ca[95]. Laboratory experiments have shown that the Sr-Ca distribution coefficient in calcite is growth-rate dependent[96], but the growth of stalagmite K2 did not change notably around 55.5 ky BP. Evaluation of the potential effects of changes in Sr availability from soil[97] or volcanic activity near Liang Luar after ~60 ky BP[4] is beyond the scope of this study.

Mg/Ca data points have been reconstructed across the interval of anomalously high Mg/Sr spanning the first half of MIS4 (70.3–64.9 ky BP), where the underlying PCP signal has been overprinted by non-PCP processes. However, the Mg/Ca and $\delta^{18}O_{iv}$ are well correlated before 70.3 ky BP, and also during the second half of MIS4 (64.9–60 ky BP), when the PCP signal is uninterrupted. And the pattern of change in $\delta^{18}O_{iv}$ across the full length of MIS4 is symmetrical. Therefore, we applied the best fit relationship between Mg/Ca and $\delta^{18}O_{iv}$ for the second half of MIS4 [$\log_{10}(1000Mg/Ca) = 0.0845*\delta^{18}O_{iv} + 1.727$ ($R^2 = 0.67$)] to infill PCP-compatible Mg/Ca data across the first half of MIS4.

Analysis of modern rainfall and oxygen-isotope climatology. Establishing the relationship between Mg/Ca and $\delta^{18}O_{iv}$ in stalagmite LR09-K2 and past rainfall requires site-specific information on modern mean annual

rainfall, rainfall seasonality and the $\delta^{18}O$ of rainfall. Supplementary Note 2 describes our analysis of the modern rainfall and oxygen-isotope climatology. Briefly, in 2006–2007, the isotopic composition of rainfall was monitored at a collection site established ~700 m from Liang Luar and Liang Bua (Fig. 1). The rainfall amounts and $\delta^{18}O$ and $\delta^{2}H$ values determined for 39 days with rainfall are summarised in Griffiths et al.[14]. We scaled the short-term dataset to the longer-term rainfall climatology of western Flores using data from the NASA Tropical Rainfall Measuring Mission (TRMM) and rain-gauge data from the Global Historical Climatology Network (GHCN). The mean annual rainfall at Liang Luar was determined to be 1,405 ± 33 mm (2 SE) with a summer (December–March) contribution of 61.7 ± 0.6% (2 SE) (Supplementary Fig. 6). Given the uncertainties in this estimate, we rounded the result to 1,400 mm and allocated 870 mm (62%) to summer and 530 mm to the rest of the year ('winter', April–November) to scale the rainfall history for Liang Luar.

Supplementary 7 shows that the rainfall seasonality and $\delta^{18}O$ seasonality at Liang Luar and the neighbouring islands of Bali and Sulawesi[22] are closely linked. The divisions between summer and winter, as defined here, align with conspicuous shifts in rainfall $\delta^{18}O$ marking the start and end of summer monsoon convection. The cave dripwater oxygen-isotope mixing model was scaled to summer and winter rainfall amounts on the grounds that the good reproducibility of Liang Luar stalagmite $\delta^{18}O$ records is due to consistent recording of the effect of changes in rainfall seasonality on the amount-weighted mean annual $\delta^{18}O$ of rainfall (Supplementary Fig. 2).

Stable isotope analysis of *Stegodon* tooth enamel. The analytical approach for measurements of $\delta^{18}O$ and $\delta^{13}C$ in the carbonate phase of fossil *Stegodon* tooth enamel samples from the So'a Basin is described elsewhere[69]. The new measurements reported here for *Stegodon* tooth samples from Liang Bua were conducted at the University of Wollongong School of Earth, Atmospheric and Life Sciences[71]. Prior to sampling, the outer tooth surfaces were cleaned using a rotary hand-held device to minimise contamination. Approximately 100 mg of powdered enamel was then obtained using a diamond-coated burr on a Dremel hand drill. The enamel was drilled across the tooth from top to bottom to obtain an annual average isotope signal. The enamel powder was pre-treated with 2% sodium hypochlorite to oxidise organic residues and 0.1 M acetic acid to remove exogenous carbonates. The samples were rinsed with deionised water and dried following each chemical treatment. Approximately 5 mg of pre-treated sample powder was reacted under vacuum with 105% H_3PO_4 at 90°C in a MultiPrep device. The liberated CO_2 was analysed using a Micromass PRISM III dual-inlet mass spectrometer, and the data were normalised to the VPDB scale via NBS-18 ($\delta^{18}O$, –23.01‰; $\delta^{13}C$, –5.04‰), NBS-19 ($\delta^{18}O$, –2.20‰; $\delta^{13}C$, 1.95‰), NBS-20 ($\delta^{18}O$, –4.14‰; $\delta^{13}C$, –1.06‰) and in-house laboratory standards.

Milk molars belonging to juvenile *Stegodon* individuals were omitted from the analysis of the So'a Basin fossil assemblage, which contains adult molars, to avoid the inclusion of lactating or weaning individuals. However, they were included in the analysis of Liang Bua, where 94% of the assemblage represents juveniles. The pooled average $\delta^{18}O$ values for prenatal, juvenile and adult tooth enamel samples from Liang Bua were found to be in good agreement (–3.94 ± 0.18‰, 2σ; Supplementary Fig. 12).

Acknowledgements

We dedicate this article to the late Wahyoe S. Hantoro (1953–2023) and Neil Anderson (1943–2019), both of whom were foundational team-members for our speleothem research in Liang Luar. This work was carried out in collaboration with the Indonesian Institute of Sciences (LIPI) under LIPI permit number 2748/SU.3/KS/2007 and Kementerian Negara Riset dan Teknologi (RISTEK) permit number 04/TKPIPA/FRP/SM/IV/2009. We are grateful to the people of Rampasasa village who generously supported our team in the field, and to Russell Drysdale, Jodie Rutledge, Eko Yulianto, Michael Griffiths, Sophie Lewis, Emma St Pierre, Dan Zwartz, and Julie Mazerat, who provided caving expertise and technical support. We also thank Joe Cali, Linda McMorrow and Chris Vardanega for support in the stable isotope and ICP-OES laboratories. Professor Naoyuki Kurita (Nagoya University) kindly provided access to water isotope-precipitation data for sites in Indonesia monitored by the Institute of Observational Research for Global Change (IORGC)/Japan Agency for Marine-Earth Science and Technology (JAMSTEC). The *Stegodon* fossil excavations were authorised by the Geological Agency and conducted under RISTEK permit numbers 0107/SIP/FRP/SM/VI/2010 and 300/SIP/FRP/SM/VIII/2013, and were executed in collaboration with the Museum Geologi and Pusat Survei Geologi in Bandung and Pusat Penelitian Arkeologi Nasional (ARKENAS) in Jakarta. This research would not have been possible without the support of the late Michael J. Morwood (1950–2013), collaborators in the field, and their institutions that approved the stable isotope analysis of fossil tooth enamel. For this we thank: (1) the former directors of Museum Geologi Bandung and research staff (Iwan Kurniawan, Fachroel Aziz, Erick Setyabudi, Makmur, Unggul Prasetyo, Halmi Insani, Hani Oktariani and Ifan Y.

P. Suharyogi) and (2) the former directors of ARKENAS and research staff (Jatmiko, Thomas Sutikna, E. Wahyu Saptomo and the late Rokus Due Awe). Allan Chivas kindly supported the stable isotope analysis at the University of Wollongong. Both research streams were funded by Australian Research Council (ARC) Discovery Project grants DP0663274, DP1095673 and DP180103762 to M.K.G., W.S.H., J.-x.Z., J.C.H., R.L.E. and H.C., DP0770234 to the late M. J. Morwood, and a Future Fellowship (FT1010384) to G.vdB; U.S. National Science Foundation (NSF) grant 2202913 to R.L.E.; and National Natural Science Foundation of China (NSFC) grants 41731174 and 41888101 to H.C.

Author contributions

M.K.G.: conceptualization, methodology, fieldwork, investigation, validation, formal analysis, resources, supervision, visualisation, writing – original draft, writing – review & editing, project administration, data curation. L.K.A.: methodology, fieldwork, investigation, validation, formal analysis, writing – review & editing. N.S.: investigation, validation, formal analysis, writing – review & editing. W.S.H.: resources, fieldwork, project administration, writing – original draft. M.R.P.: methodology, investigation, validation, formal analysis, writing – review & editing, data curation. G.vdB.: fieldwork, resources, investigation, supervision, project administration, writing – review & editing. H.S.-G.: fieldwork, investigation, validation, visualisation, writing – review & editing. S.A.C.: formal analysis, writing – review & editing. R.L.E.: investigation, validation, writing – review & editing. H.C.: investigation, validation, writing – review & editing. J.-x.Z.: investigation, validation, writing – review & editing. J.C.H.: investigation, validation, writing – review & editing. A.K.K.: validation, visualisation, writing – review & editing. M.J.G.: formal analysis, writing – review & editing. B.W.S.: fieldwork, resources, writing – review & editing. J.A.C.: investigation, writing – review & editing. B.C.D.: investigation, writing – review & editing. G.K.S.: fieldwork, investigation, writing – review & editing. N.A.: fieldwork, investigation. H.W.: investigation, validation, writing – review & editing. H.R.: fieldwork, writing – review & editing.

References

1. Brown, P. *et al.* A new small-bodied hominin from the Late Pleistocene of Flores, Indonesia. *Nature* **431**, 1055–1061 (2004).
2. Morwood, M. J. *et al.* Archaeology and age of a new hominin from Flores in eastern Indonesia. *Nature* **431**, 1087–1091 (2004).
3. Roberts, R. G. *et al.* Geochronology of cave deposits at Liang Bua and of adjacent river terraces in the Wae Racang valley, western Flores, Indonesia: a synthesis of age estimates for the type locality of *Homo floresiensis*. *J. Hum. Evol.* **57**, 484–502 (2009).
4. Sutikna, T. *et al.* Revised stratigraphy and chronology for *Homo floresiensis* at Liang Bua in Indonesia. *Nature* **532**, 366–369 (2016).
5. van den Bergh, G. D. *et al.* The Liang Bua faunal remains: a 95 k.yr. sequence from Flores, East Indonesia. *J. Hum. Evol.* **57**, 527–537 (2009).
6. Sutikna, T. *et al.* The spatio-temporal distribution of archaeological and faunal finds at Liang Bua (Flores, Indonesia) in light of the revised chronology for *Homo floresiensis*. *J. Hum. Evol.* **124**, 52–74 (2018).
7. Bird, M. I., O'Grady, D. & Ulm, S. Humans, water, and the colonization of Australia. *Proc. Natl Acad. Sci. U.S.A.* **113**, 11477–11482 (2016).
8. Saltré, F. *et al.* Climate-human interaction associated with southeast Australian megafauna extinction patterns. *Nat. Commun.* **10**, 5311, doi.org/10.1038/s41467-019-13277-0 (2019).
9. Cantalapiedra, J. L. *et al.* The rise and fall of proboscidean ecological diversity. *Nat. Ecol. Evol.* **5**, 1266–1272 (2021).
10. Tachikawa, K. *et al.* The precession phase of hydrological variability in the Western Pacific Warm Pool during the past 400 ka. *Quat. Sci. Rev.* **30**, 3716–3727 (2011).
11. Carolin, S. A. *et al.* Varied response of Western Pacific hydrology to climate forcings over the Last Glacial period. *Science* **340**, 1564–1566 (2013).
12. Liu, Y. *et al.* Obliquity pacing of the western Pacific Intertropical Convergence Zone over the past 282,000 years. *Nat Commun.* **6**, 10018, doi: 10.1038/ncomms10018 (2015).

13. Windler, G., Tierney, J. E., DiNezio, P. N., Gibson, K. & Thunell, R. Shelf exposure influence on Indo-Pacific Warm Pool climate for the last 450,000 years. *Earth Planet. Sci. Lett.* **516**, 66–76 (2019).

14. Griffiths, M. L. *et al.* Increasing Australian-Indonesian monsoon rainfall linked to early Holocene sea-level rise. *Nat. Geosci.* **2**, 636–639 (2009).

15. Lewis, S. C. *et al.* High-resolution stalagmite reconstructions of Australian-Indonesian monsoon rainfall variability during Heinrich Stadial 3 and Greenland Interstadial 4. *Earth Planet. Sci. Lett.* **303**, 133–142 (2011).

16. Ayliffe, L. K. *et al.* Rapid interhemispheric climate links via the Australasian monsoon during the last deglaciation. *Nat. Commun.* **4**, 2908, doi: 10.1038/ncomms3908 (2013).

17. Scroxton, N. *et al.* Antiphase response of the Indonesian-Australian monsoon to millennial-scale events of the last glacial period. *Sci. Rep.* **12**, 20214, doi.org/10.1038/s41598-022-21843-8 (2022).

18. Cobb, K. M., Adkins, J. F., Partin, J. W. & Clark, B. Regional-scale climate influences on temporal variations of rainwater and cave dripwater oxygen isotopes in northern Borneo. *Earth Planet. Sci. Lett.* **263**, 207–220 (2007).

19. Baker, A. J., *et al.* Seasonality of westerly moisture transport in the East Asian summer monsoon and its implications for interpreting precipitation $\delta^{18}O$. *J. Geophys. Res: Atmos.* **120**, 5850–5862 (2015).

20. Konecky, B. L., Noone, D. C. & Cobb, K. M. The influence of competing hydroclimate processes on stable isotope ratios in tropical rainfall. *Geophys. Res. Lett.* **46**, 1622–1633 (2019).

21. Wolf, A., Roberts, W. H. G., Ersek, V., Johnson, K. R. & Griffiths, M. L. Rainwater isotopes in central Vietnam controlled by two oceanic moisture sources and rainout effects. *Sci. Rep.* **10**, 16482, doi.org/10.1038/s41598-020-73508-z (2020).

22. Kurita, N., Ichiyanagi, K., Matsumoto, J., Yamanaka, M. D. & Ohata, T. The relationship between the isotopic content of precipitation and the precipitation amount in tropical regions. *J. Geochem. Explor*. **102**, 113–122 (2009).

23. Cruz, F. W. *et al*. Evidence of rainfall variations in Southern Brazil from trace element ratios (Mg/Ca and Sr/Ca) in a Late Pleistocene stalagmite. *Geochim. Cosmochim. Acta* **71**, 2250–2263 (2007).

24. Griffiths, M. L. *et al.* Evidence for Holocene changes in Australian-Indonesian monsoon rainfall from stalagmite trace element and stable isotope ratios. *Earth Planet. Sci. Lett.* **292**, 27–38 (2010).

25. Liu, Y-H. et al. Links between the East Asian monsoon and North Atlantic climate during the 8,200 year event. *Nat. Geosci.* **6**, 117–120 (2013).

26. Cheng, H. *et al.* Climate variations of Central Asia on orbital to millennial timescales. *Sci. Rpt.* **6**, 36975, doi:10.1038/srep36975 (2016).

27. Zhang, H. *et al.* East Asian hydroclimate modulated by the position of the westerlies during Termination I. *Science* **362**, 580–583 (2018).

28. Kimbrough, A. K. *et al.* Multi-proxy validation of glacial-interglacial rainfall variations in southwest Sulawesi. *Commun. Earth Environ*. **4**, 210, doi.org/10.1038/s43247-023-00873-8 (2023).

29. Wolf, A. *et al.* Deciphering local and regional hydroclimate resolves contradicting evidence on the Asian monsoon evolution. *Nat. Commun.* **14**, 5697, doi.org/10.1038/s41467-023-41373-9 (2023).

30. Fairchild, I. J. *et al.* Controls on trace element (Sr-Mg) compositions of carbonate cave waters: implications for speleothem climatic records. *Chemical Geology* **166**, 255–269 (2000).

31. Johnson, K. R., Hu, C., Belshaw, N. S. & Henderson, G. H. Seasonal trace-element and stable-isotope variations in a Chinese speleothem: The potential for high-resolution paleomonsoon reconstruction. *Earth Planet. Sci. Lett.* **244**, 394–407 (2006).

32. Sinclair, D. *et al.* Magnesium and strontium systematics in tropical speleothems from the Western Pacific. *Chem. Geol.* **294-295**, 1–17 (2012).

33. Tremaine, D. M. & Froelich, P. N. Speleothem trace element signatures: A hydrologic geochemical study of modern cave dripwaters and farmed calcite. *Geochim. Cosmochim. Acta* **121**, 522–545 (2013).

34. Wassenburg, J. A. *et al.* Calcite Mg and Sr partition coefficients in cave environments: Implications for interpreting prior calcite precipitation in speleothems. *Geochim. Cosmochim. Acta* **269**, 581–596 (2020).

35. Wang, Y. J. *et al.* A high-resolution absolute-dated Late Pleistocene monsoon record from Hulu Cave, China. *Science* **294**, 2345–2348 (2001).

36. Cheng, H. *et al.* Ice age terminations. *Science* **326**, 248–252 (2009).

37. DiNezio, P. N. *et al.* The climate response of the Indo-Pacific warm pool to glacial sea level. *Paleoceanography* **31**, 866–894 (2016).

38. Buckingham, F. L. *et al.* Termination 1 millennial-scale rainfall events over the Sunda Shelf. *Geophys. Res. Lett.* **49**, e2021GL096937, doi.org/10.1029/2021GL096937 (2022).

39. van Bemmelen, R. W. General geology of Indonesia and adjacent archipelagoes. In van Bemmelen (ed.), *The Geology of Indonesia* (Government Printing Office, The Hague, 1949).

40. Lea, D. W., Pak, D. K. & Spero, H. J. Climate impact of Late Quaternary equatorial Pacific sea surface temperature variations. *Science* **289**, 1719–1724 (2000).

41. McDermott, F. Paleo-climate reconstruction from stable isotope variations in speleothems: a review. *Quat. Sci. Rev.* **23**, 901–918 (2004).

42. Huang, Y. & Fairchild, I. J. Partitioning of Sr^{2+} and Mg^{2+} into calcite under karst-analogue experimental conditions. *Geochim. Cosmochim. Acta* **65**, 47–62 (2001).

43. Treble, P. C. *et al.* Ubiquitous karst hydrological control on speleothem oxygen isotope variability in a global study. *Commun. Earth Environ*. **3**, 29, doi.org/10.1038/s43247-022-00347-3 (2022).

44. Deininger, M. *et al.* Are oxygen isotope fractionation factors between calcite and water derived from speleothems sytematically biased due to prior calcite precipitation? *Geochim. Cosmochim. Acta* **305**, 212–227 (2021).

45. Skiba, V. & Fohlmeister, J. Contemporaneously growing speleothems and their value to decipher in-cave processes–A modelling approach. *Geochim. Cosmochim. Acta* **348**, 381–396 (2023).

46. Patterson, E. W. *et al.* Local hydroclimate alters interpretation of speleothem $\delta^{18}O$ records. *Nat. Commun.* **15**, 9064, doi.org/10.1038/s41467-024-53422-y (2024).

47. Griffiths, M. L. *et al.* Australasian monsoon response to Dansgaard-Oeschger event 21 and teleconnections to higher latitudes. *Earth Planet. Sci. Lett.* **369–370**, 294–304 (2013).

48. Griffiths, M. L. *et al.* Younger Dryas-Holocene temperature and rainfall history of southern Indonesia from $\delta^{18}O$ in speleothem calcite and fluid inclusions. *Earth Planet. Sci. Lett.* **295**, 30–36 (2010).

49. Yuan, D. *et al.* Timing, duration, and transitions of the Last Interglacial Asian monsoon. *Science* **304**, 575–578 (2004).

50. Pausata, F. S. R., Battisti, D. S., Nisancioglu, K. H. & Bitz, C. M. Chinese stalagmite $\delta^{18}O$ controlled by changes in the Indian monsoon during a simulated Heinrich event. *Nat. Geosci.* **4**, 474–480 (2011).

51. Battisti, D. S., Ding, Q. & Roe, G. H. Coherent pan-Asian climatic isotopic response to orbital forcing of tropical insolation. *J. Geophys. Res Atmos.* **119**, 11,997–12,020 (2014).

52. Dansgaard, W. Stable isotopes in precipitation. *Tellus* **16**, 436–468 (1964).

53. Moerman, J. W. *et al.* Diurnal to interannual rainfall $\delta^{18}O$ variations in northern Borneo driven by regional hydrology. *Earth Planet. Sci. Lett.* **369–370**, 108–119 (2013).

54. Cai, Z. & Tian, L. Atmospheric controls on seasonal and interannual variations in the precipitation isotope in the East Asian Monsoon region. *J. Climate* **29**, 1339–1352 (2016).

55. Permana, D. S., Thompson, L. G. & Setyadi, G. Tropical West Pacific moisture dynamics and climate controls on rainfall isotopic ratios in southern Papua, Indonesia. *J. Geophys. Res. Atmos.* **121**, 2222–2245 (2016).

56. Cheng, H. *et al.* The Asian monsoon over the past 640,000 years and ice age terminations. *Nature* **534**, 640–646 (2016).

57. Cheng, H., Sinha, A., Wang, X. F., Cruz, F. W. & Edwards, R. L. The global paleomonsoon as seen through speleothem records from Asia and the Americas. *Clim. Dyn.* **39**, 1045–1062 (2012).

58. Hellstrom, J. C. & McCulloch, M. T. Multi-proxy constraints on the climatic significance of trace element records from a New Zealand speleothem. *Earth Planet. Sci. Lett.* **179**, 287–297 (2000).

59. Mohtadi, M. *et al.* Glacial to Holocene swings of the Australian-Indonesian monsoon. *Nat. Geosci.* **4**, 540–544 (2011).

60. Xue, F., Wang, H. & He, J. Interannual variability of Mascarene High and Australian High and their influences on East Asian summer monsoon. *J. Meteorol. Soc. Japan* **82**, 1173–1186 (2004).

61. Zhuang, M. & Duan, A. Revisiting the cross-equatorial flows and Asian summer monsoon precipitation associated with the Maritime Continent. *J. Clim.* **32**, 6803–6821 (2019).

62. Lambeck, K. & Chappell, J. Sea level change through the last glacial cycle. *Science* **292**, 679–686 (2001).

63. Dubois, N. *et al.* Indonesian vegetation response to changes in rainfall seasonality over the past 25,000 years. *Nat. Geosci.* **7**, 513–517 (2014).

64. Yan, M. I. *et al.* Understanding the Australian Monsoon change during the Last Glacial Maximum with a multi-model ensemble. *Clim. Past* **14**, 2037–2052 (2018).

65. Krause, C. E. *et al.* Spatio-temporal evolution of the Australasian monsoon hydroclimate over the last 40,000 years. *Earth Planet. Sci. Lett.* **513**, 103–112 (2019).

66. Wang, B. & Ding, Q. Global monsoon: Dominant mode of annual variation in the tropics. *Dynam. Atmos. Oceans* **44**, 165–183 (2008).

67. Brumm, A. *et al.* Age and context of the oldest known hominin fossils from Flores. *Nature* **534**, 249–253 (2016).

68. van den Bergh, G. D. *et al. Homo floresiensis*-like fossils from the early Middle Pleistocene of Flores. *Nature* **534**, 245–248 (2016).

69. van den Bergh, G. D. *et al.* An integrative geochronological framework for the Pleistocene So'a basin (Flores, Indonesia), and its implications for faunal turnover and hominin arrival. *Quat. Sci. Rev.* **294**, 107721. doi.org/10.1016/j.quascirev.2022.107721 (2022).

70. Kaifu, Y. *et al.* Early evolution of small body size in *Homo floresiensis*. *Nat. Commun.* **15**, 6381, doi.org/ 10.1038/s41467-024-50649-7 (2024).

71. Puspaningrum, M. R. *Proboscidea as Palaeoenvironmental Indicators in Southeast Asia*. PhD thesis, School of Earth and Environmental Sciences, University of Wollongong, 2016. https://ro.uow.edu.au/theses/4944.

72. Ayliffe, L. K., Lister, A. M., Chivas, A. R. The preservation of glacial-interglacial climatic signatures in the oxygen isotopes of elephant skeletal phosphate. *Palaeogeogr. Palaeoclimatol. Palaeoecol.* **99**, 179–191 (1992).

73. Ayliffe, L. K., Chivas, A. R., Leakey, M. G. The retention of primary oxygen isotope compositions of fossil elephant skeletal phosphate. *Geochim. Cosmochim. Acta* **58**, 5291–5298 (1994).

74. Blumenthal, S. A. *et al.* Aridity and hominin environments. *Proc. Natl Acad. Sci. U.S.A.* **114**, 7331–7336 (2017).

75. Westaway, K. E. *et al.* An early modern human presence in Sumatra 73,000–63,000 years ago. *Nature* **548**, 322–325 (2017).

76. Clarkson, C. *et al.* Human occupation of northern Australia by 65,000 years ago. *Nature* **547**, 306–310 (2017).

77. Barnosky, A. D., Koch, P. L., Feranec, R. S., Wing, S. L. & Shabel, A. B. Assessing the causes of Late Pleistocene extinctions on the continents. *Science* **306**, 70–75 (2004).

78. Braje, T. J. & Erlandson, J. M. Human acceleration of animal and plant extinctions: a Late Pleistocene, Holocene, and Anthropocene continuum. *Anthropocene* **4**, 14–23 (2013).

79. Sandom, C., Faurby, S., Sandel, B. & Svenning, J.-C. Global late Quaternary megafauna extinctions linked to humans, not climate change. *Proc. R. Soc. B* **281**, 20133254, doi.org/10.1098/rspb.2013.3254 (2014).

80. Lüdecke, T. *et al.* Carbon, nitrogen, and oxygen stable isotopes in modern tooth enamel: A case study from Gorongosa National Park, central Mozambique. *Front. Ecol. Evol.* 10, 958032. doi: 10.3389/fevo.2022.958032 (2022).

81. Asoka, A., Wada, Y., Fishman, R. & Mishra, V. Strong linkage between precipitation intensity and monsoon season groundwater recharge in India. *Geophys. Res. Lett.* **45**, 5536–5544 (2018).

82. Westaway, K. E. *et al. Homo floresiensis* and the late Pleistocene environments of eastern Indonesia: defining the nature of the relationship. *Quat. Sci. Rev.* **28**, 2897–2912 (2009).

83. Veatch, E. G. *et al.* Temporal shifts in the distribution of murine rodent body size classes at Liang Bua (Flores, Indonesia) reveal new insights into the paleoecology of *Homo floresiensis* and associated fauna. *J. Hum. Evol.* **130**, 45–60 (2019).

84. O'Connell, J. F. & Allen, J. Restaurant at the end of the universe: modelling the colonisation of Sahul. *Aust. Archaeol.* **74**, 5–17 (2012).

85. Brook, B. W. & Johnson, C. N. Selective hunting of juveniles as a cause of the imperceptible overkill of the Australian Pleistocene megafauna. *Alcheringa* **30**, 39–48 (2006).

86. Edwards, R. L., Chen, J. H. & Wasserberg, G. J. ^{238}U-^{234}U-^{230}Th-^{232}Th systematics and the precise measurement of time over the past 500,000 years. *Earth Planet. Sci. Lett.* **81**, 175–192 (1987).

87. Hellstrom, J. Rapid and accurate U/Th dating using parallel ion-counting multi-collector ICP-MS. *J. Anal. Atom. Spectrom.* **18**, 1346–1351 (2003).

88. Cheng, H. *et al.* Improvements in ^{230}Th dating, ^{230}Th and ^{234}U half-life values, and U-Th isotopic measurements by multi-collector inductively coupled plasma mass spectrometry. *Earth Planet. Sci. Lett.* **371**, 82–91 (2013).

89. Bronk Ramsey, C. Deposition models for chronological records. *Quat. Sci. Rev.* **27**, 42–60 (2008).

90. Bronk Ramsey, C. & Lee, S. Recent and planned developments of the program OxCal. *Radiocarbon* **55**, 720–730 (2013).

91. Schrag, D. P. Rapid analysis of high-precision Sr/Ca ratios in corals and other marine carbonates. *Paleoceanography* **14**, 97–102 (1999).

92. de Villiers, S., Greaves, M. & Elderfield, H. An intensity ratio calibration method for the accurate determination of Mg/Ca and Sr/Ca of marine carbonates by ICP-AES. *Geochem. Geophys. Geosyst.* **3**, 1–14 (2002).

93. Hathorne, E. C. *et al.* Interlaboratory study for coral Sr/Ca and other element/Ca ratio measurements. *Geochem. Geophys. Geosyst.* **14**, 3730–3750 (2013).

94. Waelbroeck, C. *et al.* Sea-level and deep water temperature changes derived from benthic foraminifera isotopic records. *Quat. Sci. Rev.* **21**, 295–305 (2002).

95. Wassenberg, J. A. *et al.* Climate and cave control on Pleistocene/Holocene calcite-to-aragonite transitions in speleothems from Morocco: Elemental and isotopic evidence. *Geochim. Cosmochim. Acta* **92**, 23–47 (2012).

96. Lorens, R. B. Sr, Cd, Mn and Co distribution coefficients in calcite as a function of calcite precipitation rate. *Geochim. Cosmochim. Acta* **45**, 553–561 (1981).

97. Fairchild, I. J. & Treble, P. C. Trace elements in speleothems as recorders of environmental change. *Quat. Sci. Rev.* **28**, 449–468 (2009).

98. GEBCO Compilation Group, *GEBCO* 2023 Grid, doi.org/10.5285/f98b053b-0cbc-6c23-e053-6c86abc0af7b (2023).

99. Schneider, U., Becker, A., Finger, P., Rustemeier, E. & Ziese, M. GPCC full data monthly product version 2020 at 0.25°: monthly land-surface precipitation from rain-gauges built on GTS-based and historical data, doi.org/10.5676/DWD_GPCC/FD_M_V2020_025 (2020).

Supplementary Information

This file contains:

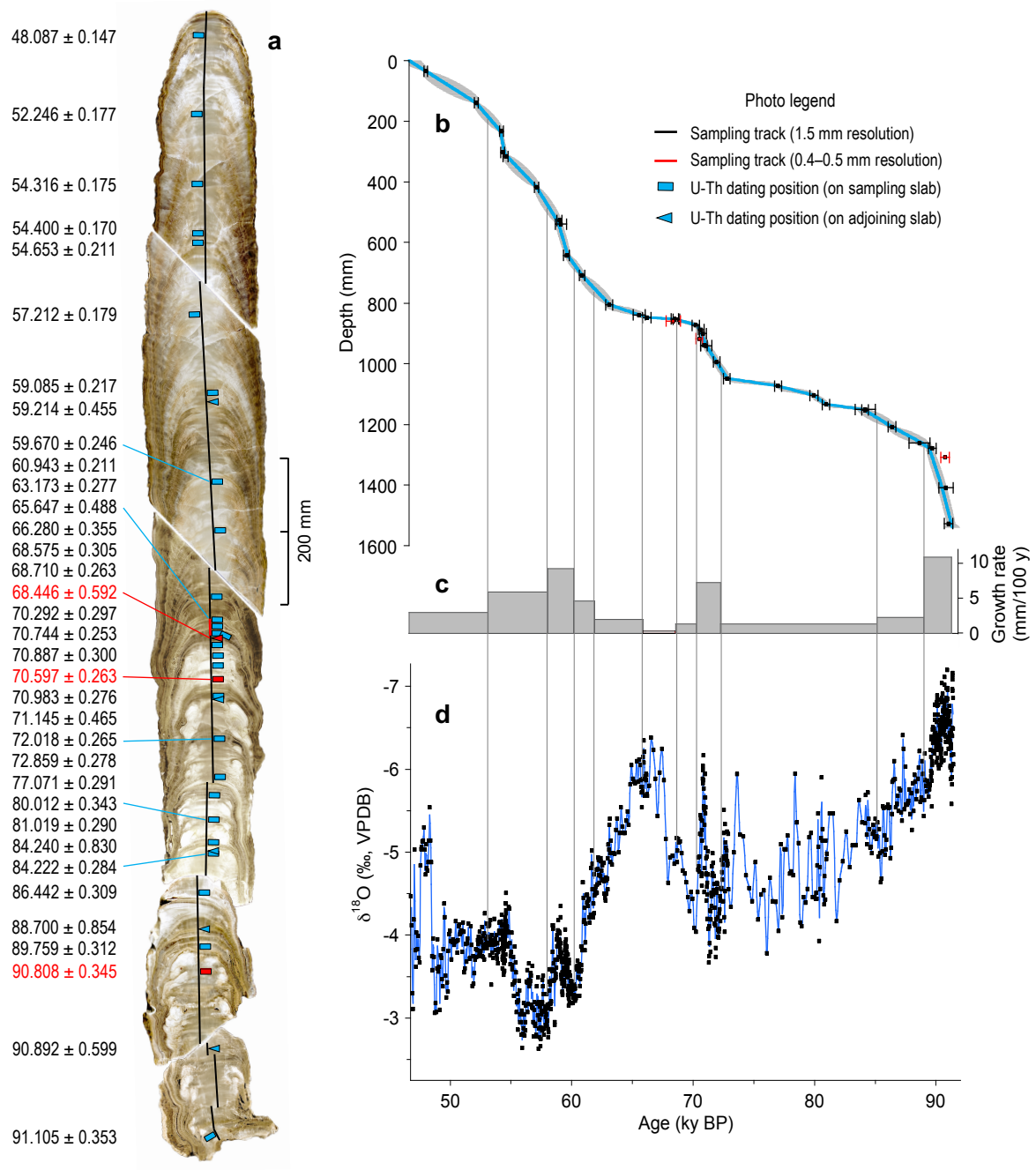

Supplementary Figure 1 | Age model, growth rates and sampling resolution for stalagmite LR09-K2. a Image of polished slab of the stalagmite cut parallel to the central growth axis. The positions of ^{230}Th dates (expressed as ky BP ± 2σ errors) are shown alongside the sampling tracks. **b** Age-depth model (blue line) with 95% confidence interval (grey shading) computed using the OxCal analysis module (version 4.3)[1,2]. Three outlier dates (in red) were excluded to fine tune the age model. **c** Summary of stalagmite growth rates. **d** Sampling resolution as a function of growth rate. The blue curve shows the fit of the resampled 50-year resolution stalagmite δ^{18}O record to the raw δ^{18}O data (black dots). Supplementary Table 1 contains details of the ^{230}Th age data.

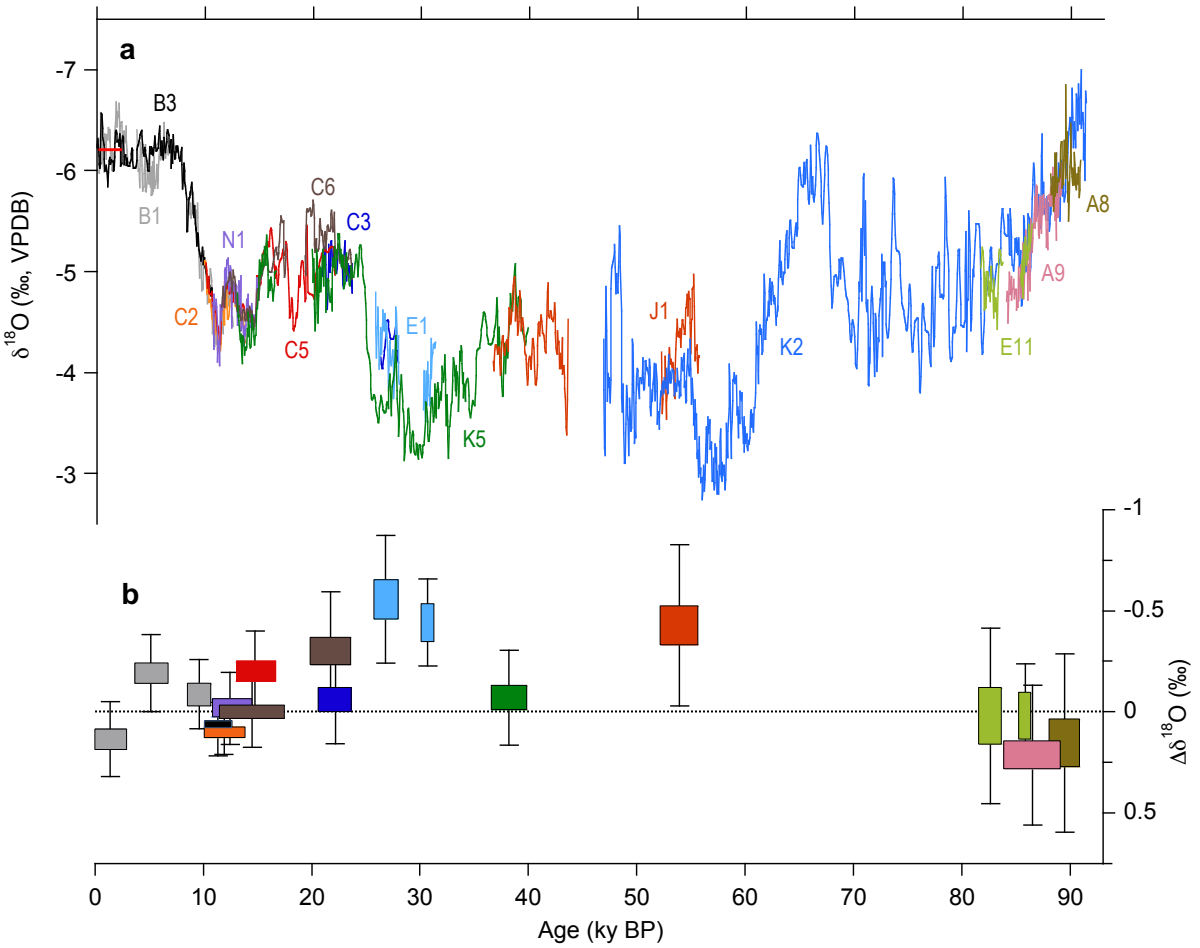

Supplementary Figure 2 | Reproducibility of Liang Luar stalagmite $\delta^{18}O$ records over the past 91,000 years. a Comparison of Liang Luar stalagmite calcite $\delta^{18}O$ records at 50-year resolution (binned data from Scroxton et al.[3]). The new LR09-K2 record is shown in blue. Previously reported records are from Griffiths et al.[4] (LR06-B1, B3), Lewis et al.[5] (LR07-E1), Ayliffe et al.[6] (LR07-C2, C3, C5, C6), Griffiths et al.[7] (LR07-A8, A9, E11) and Scroxton et al.[3] (LR09-N1, J1; LR11-K5). The onset and termination of the LR07-E11 record were not included in the comparison due to the effects of low sample resolution and chronological uncertainties[7]. The section of the LR09-J1 record spanning 52.1–43.6 ky BP was excluded because it is composed of recrystallised, non-primary calcite subject to isotopic overprinting by diagenetic fluids[3]. The red line shows the amount-weighted average stalagmite $\delta^{18}O$ value (–6.2 ± 0.2‰, 2 SE) for summer and winter rainfall conditions at Liang Luar during the Common Era. **b** Summary of differences in stalagmite $\delta^{18}O$ records across overlapping intervals. Colour-coded box plots show the average difference in $\delta^{18}O$ (±2 SE) for 18 intervals ('whiskers' indicate the 2σ range of the differences between individual data points within each interval). The median absolute difference for 13 overlapping intervals among the 14 stalagmites is 0.09‰ (range, 0.00–0.50‰). The average absolute difference for the three intervals of overlap between the K2 record and the A8, A9 and E11 records (90.875–81.673 ky BP) is 0.13‰. The difference between the K2 and J1 records across 55.675–55.225 ky BP is 0.43‰. These differences are small in the context of the 3.5‰ range in $\delta^{18}O$ for the new K2 record. The good reproducibility of the 14 $\delta^{18}O$ records (derived from widely separated dripwater sites and stalagmites with a broad range of growth rates) shows that they are not compromised by karst controls or in-cave effects in Liang Luar over the last 91,000 years.

Supplementary Note 1. Rayleigh fractionation modelling of the PCP process at Liang Luar

Supplementary Figures 3 and 4 below illustrate the evidence for prior calcite precipitation (PCP) provided by the stalagmite LR09-K2 Mg/Ca, Sr/Ca and Mg/Sr data. The geochemical signature of PCP is governed by Rayleigh fractionation, with Ca^{2+} decreasing exponentially relative to Mg^{2+} and Sr^{2+} in solution[8]. Critically, PCP drives the dripwater concentration of each element away from its initial dissolved bedrock value strictly according to Mg-Ca and Sr-Ca distribution coefficients less than one[9]. We used the Excel-based PCP model developed by Wassenberg et al.[10] to assess the extent of PCP in the LR09-K2 record (Supplementary Fig. 5). The model calculates change in the Mg^{2+} and Sr^{2+}concentrations in dripwater (and the stalagmite) as a consequence of progressive removal of Ca^{2+} by PCP.

The best fit of the model and stalagmite K2 data was achieved using a dolomitic limestone starting composition (52% dolomite) for Liang Luar with an accordingly low Sr concentration (170 ppm), consistent with measurements of Sr in dolomitic limestones[11]. The onset of PCP was assumed to occur at the lowest average Mg/Ca (6.340 mmol/mol) and Sr/Ca (0.0250 mmol/mol) in the K2 record from 91.4 to 82 ky BP. We then tuned the distribution coefficients for Mg/Ca (D_{Mg}) and Sr/Ca (D_{Sr}) to maximise the model fit for the 'target' ln(Sr/Ca) versus ln(Mg/Ca) slope of 0.85 across the full range of the K2 dataset. The best fit for Mg/Ca (range, 6.340–33.535 mmol/mol) requires an initial dolomitic limestone dripwater value of 220 mmol/mol, reaction temperature of 23.5°C, and D_{Mg} of 0.029. The reaction temperature (and hence D_{Mg}) for the calculation was set at an average value of 23.5°C, ~1.5°C below the average pre-industrial air temperature at Liang Luar, as indicated by sea-surface temperature reconstructions for 92–47 ky BP in the Indo-Pacific Warm Pool region[12]. The best fit for Sr/Ca (range, 0.0250–0.1086 mmol/mol) requires an initial dolomitic limestone dripwater value of 0.17 mmol/mol and D_{Sr} of 0.147. The modelled values for D_{Mg} and D_{Sr} fall well within the observed ranges for calcite (0.012–0.06 for D_{Mg}, 0.02–0.3 for D_{Sr}), as summarised by Huang and Fairchild[9] and Sinclair et al.[8].

The model results indicate that PCP is well developed in the K2 record; 82% of Ca^{2+} must be removed from solution to produce the range in Mg/Ca and Sr/Ca observed from 91.4 to 70.3 ky BP and 64.9 to 46.8 ky BP (Supplementary Fig. 5). The modelled best-fit ln(Sr/Ca) versus ln(Mg/Ca) slope (0.88) and observed slope of the K2 data (0.85) are in good agreement, and both ln/ln slopes fall squarely within the theoretical envelope of 0.88 ± 0.13 (ref.[8]).

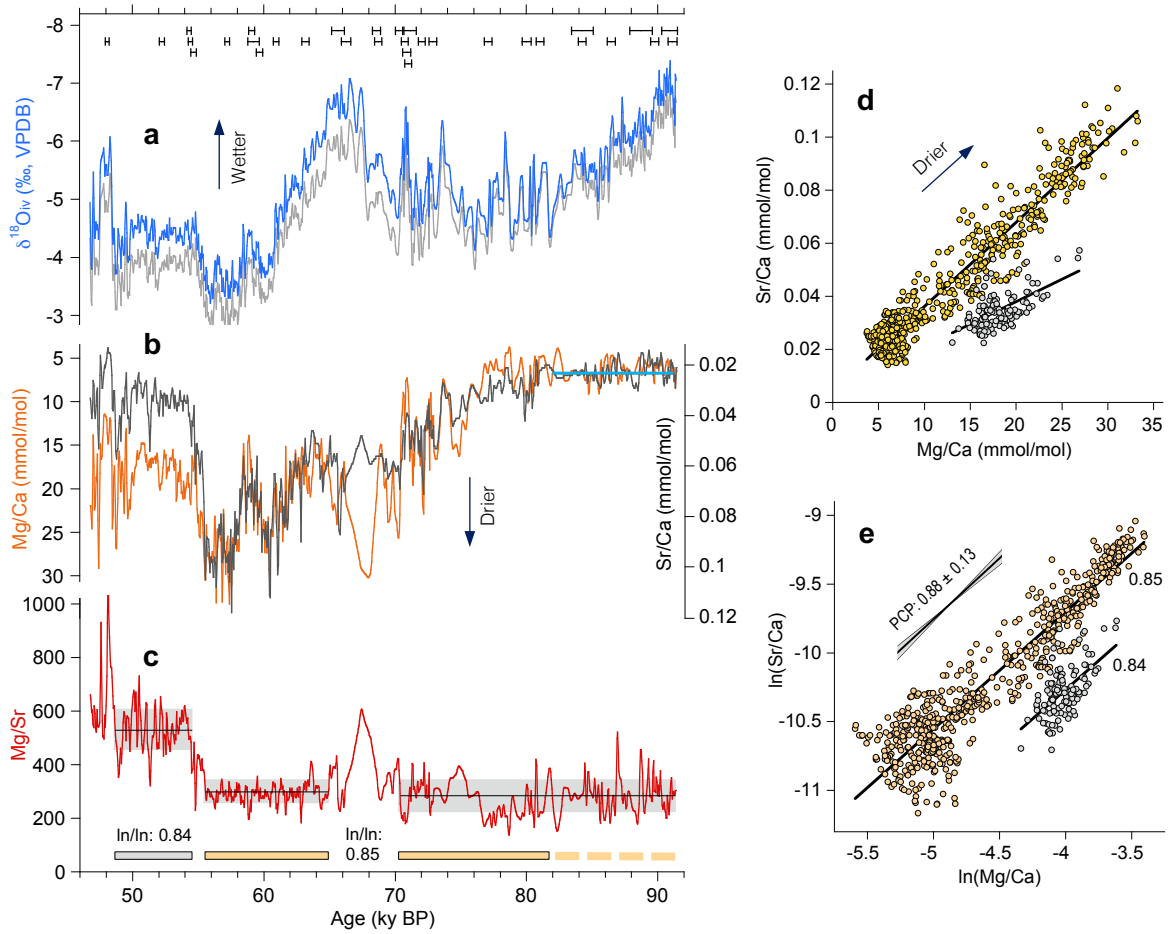

Supplementary Figure 3 | $\delta^{18}O$, Mg/Ca and Sr/Ca and initial PCP analysis for stalagmite LR09-K2. a Adjustment of the 50-year $\delta^{18}O$ record (grey) for the influence of ice volume-induced changes in the mean $\delta^{18}O$ of seawater ($\delta^{18}O_{iv}$, blue). **b** Positive covariation between the 50-year Mg/Ca (orange) and Sr/Ca (grey) records. The best fit across the full range of the data occurs when Mg/Sr is set to 290 (see **c**). Near-constant Mg/Ca and Sr/Ca values between 91.4 and 81.8 ky BP (blue line) mark stalagmite calcite deposition from dripwater with average bedrock Mg/Sr at the initiation of PCP. **c** Stalagmite Mg/Sr. Sections of the record with near-constant Mg/Sr (grey shading is ±1σ) and positive correlation between Mg/Ca and Sr/Ca are indicative of PCP, whereas intervals with anomalous Mg/Sr are influenced by non-PCP processes. The period 70.3–64.9 ky BP, with anomalously high Mg/Sr (and negative correlation between Mg/Ca and Sr/Ca), cannot be interpreted in terms of PCP. Bars at the bottom of the plot show intervals with ln(Sr/Ca) versus ln(Mg/Ca) slopes indicative of PCP. The grey bar shows the PCP-indicative ln/ln slope (0.84) for 54.4–48.6 ky BP, with higher Mg/Sr. **d** Mg/Ca versus Sr/Ca for the intervals with positive correlation and near-constant Mg/Sr (grey is for 54.4–48.6 ky BP). **e** Comparison of ln(Sr/Ca) versus ln(Mg/Ca) with the theoretical PCP slope of Sinclair et al.[8]. The good agreement of the observed slopes (0.84–0.85) with the theoretical slope (0.88 ± 0.13) confirms that most of the LR09-K2 record is controlled by PCP.

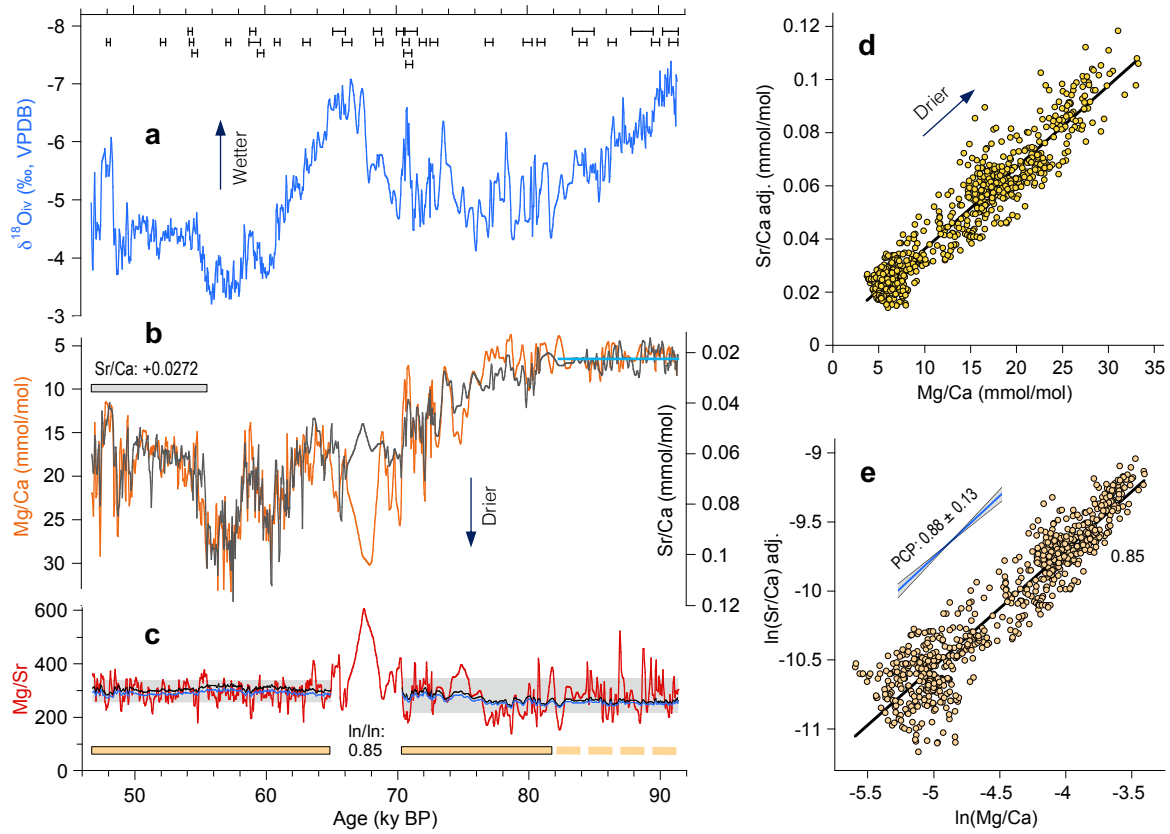

Supplementary Figure 4 | Adjusted $\delta^{18}O$, Mg/Ca and Sr/Ca and refined PCP analysis for stalagmite LR09-K2. a The ice-volume corrected $\delta^{18}O$ record. **b** Comparison of positive correlation between the Mg/Ca (orange) and adjusted Sr/Ca (grey) records. The Sr/Ca values for 54.4–46.8 ky BP have been adjusted to higher by 0.0272 mmol/mol for alignment with Mg/Ca (see Methods). The adjoining section (55.5–54.4 ky BP) was adjusted by linear interpolation. **c** Adjusted stalagmite Mg/Sr. The adjustment of Sr/Ca aligns Mg/Sr at a best-fit mean value of 296 ± 37 (1σ, grey shading) from 64.9 to 46.8 ky BP. The ln(Sr/Ca) versus ln(Mg/Ca) slope of 0.85 for the adjusted record (excluding 70.3–64.8 ky BP) is diagnostic of PCP. The black curve shows the least-squares best fit of Mg/Sr for the range of Mg/Ca and Sr/Ca values produced by PCP at ln/ln = 0.85. For comparison, the blue curve shows the good agreement with Mg/Sr produced by PCP at the theoretical ln/ln slope of 0.88, as determined by Rayleigh fractionation modelling (see Supplementary Fig. 5e). **d** Adjusted Sr/Ca versus Mg/Ca for the intervals with positive covariation and near-constant Mg/Sr in the K2 record (R^2 = 0.91, excluding 70.3–64.9 ky BP). **e** Comparison of adjusted ln(Sr/Ca) versus ln(Mg/Ca) with the theoretical PCP slope of Sinclair et al.[8]. The good agreement of the observed slope (0.85, R^2 = 0.89) and theoretical slope (0.88 ± 0.13) confirms that the full length of the LR09-K2 record (excluding 70.3–64.9 ky BP) is controlled by PCP.

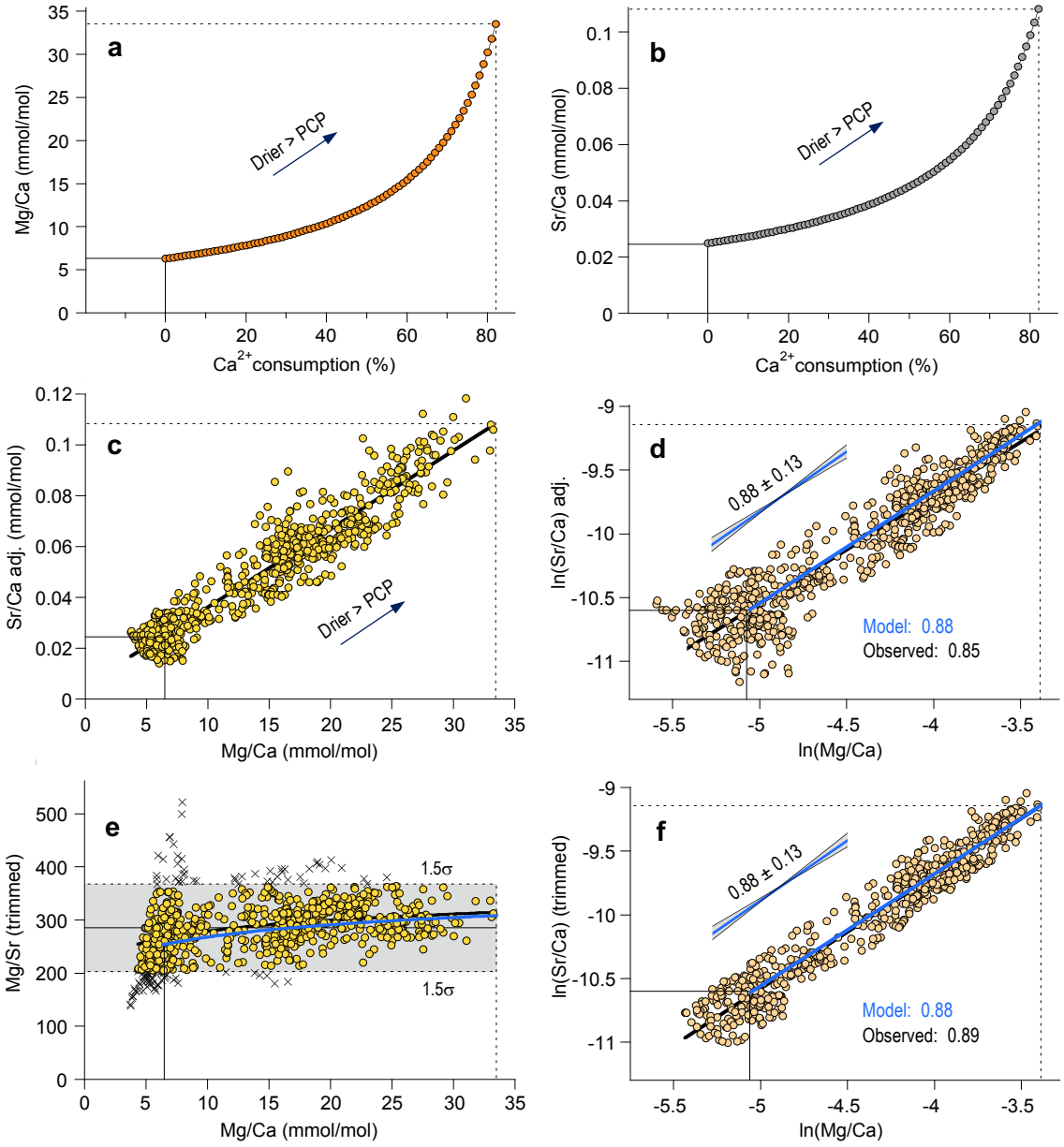

Supplementary Figure 5 | PCP Rayleigh fractionation model for Mg/Ca, Sr/Ca and Mg/Sr in stalagmite LR09-K2. a Stalagmite Mg/Ca as a function of Ca^{2+} consumption from the Excel-based PCP model of Wassenberg et al.[10]. The best fit for Mg/Ca in the K2 record (range, 6.340–33.535 mmol/mol) requires an initial dolomitic limestone dripwater value of 220 mmol/mol, reaction temperature of 23.5°C, and D_{Mg} of 0.029. **b** PCP model for stalagmite Sr/Ca. The best fit for Sr/Ca (range, 0.0250– 0.1086 mmol/mol) requires an initial dolomitic limestone dripwater value of 0.17 mmol/mol and D_{Sr} of 0.147. The model shows that 82% of Ca^{2+} must be removed from solution by PCP to produce the observed range in Mg/Ca and Sr/Ca in the K2 record. **c** Positive correlation between adjusted Sr/Ca and Mg/Ca (R^2 = 0.91, excluding 70.3–64.8 ky BP). **d** As for **c**, but for adjusted ln(Sr/Ca) versus ln(Mg/Ca). The agreement of the observed slope (0.85, R^2 = 0.89), model slope (0.88) and theoretical PCP slope (0.88 ± 0.13, ref.[8]) confirms that the K2 record is controlled by PCP. **e** Optimisation of the ln/ln model–data fit using stalagmite Mg/Sr. The PCP model (blue curve) shows the subtle logarithmic increase in Mg/Sr as a function of PCP-induced changes in Mg/Ca at ln/ln = 0.88 (mean Mg/Sr, 273; range, 254–310). The K2 stalagmite Mg/Sr also increases with Mg/Ca (black curve), but with more scatter in the data (mean Mg/Sr, 285; range, 139–522). The outlier Mg/Sr values reflect non-PCP processes. 'Trimming' of the K2 Mg/Sr dataset at the 1.5σ level (±80, black crosses) to reduce non-PCP effects optimises the data–model alignment. **f** Comparison of the trimmed and modelled ln(Sr/Ca) versus ln(Mg/Ca). The trimming optimises the data–model fit at ln/ln 0.88–0.89 near the mid-point of the theoretical ln/ln slope envelope (0.88 ± 0.13).

Supplementary Note 2. Modern rainfall and oxygen-isotope climatology at Liang Luar

Establishing the relationship between Mg/Ca and $\delta^{18}O_{iv}$ in stalagmite LR09-K2 and past rainfall requires site-specific information on modern mean annual rainfall, rainfall seasonality and the $\delta^{18}O$ of rainfall at Liang Luar. Previous work has shown that the annual cycles of rainfall and rainfall $\delta^{18}O$ at Liang Luar[4], and elsewhere in southern Indonesia[17], are closely linked. Therefore, it is important to document the modern proportions of summer rainfall (December–March) and 'winter' rainfall (April–November) at Liang Luar contributing to the amount-weighted mean annual $\delta^{18}O$ of cave dripwaters. The approach is valid at Liang Luar where the seasonal contrast in rainfall $\delta^{18}O$ is homogenised in dripwaters, thus allowing stalagmites to consistently record the mean annual $\delta^{18}O$, as demonstrated by good reproducibility of the records (Supplementary Fig. 2).

Rainfall sampling and water-isotope analysis

As no local observational data were available when we began our palaeoclimate investigation in 2006, a rainfall measurement and collection campaign was established for an entire summer monsoon season from September 2006 to April 2007. The rainfall amounts and $\delta^{18}O$ and $\delta^{2}H$ values determined for 39 days with rainfall are summarised in Griffiths et al.[4]. The monitoring site was located adjacent to Rampasasa village, ~700 m from Liang Luar and Luar Bua (see Fig. 1). Rainfall was collected using a standard open-air measuring cylinder and amounts were logged each rain day. Sealed aliquots of the samples were analysed for $\delta^{18}O$ and $\delta^{2}H$ using standard laboratory techniques[4]. All isotopic data are reported as permil (‰) deviations relative to Vienna Standard Mean Ocean Water (VSMOW). The analytical precision (2σ) for replicate measurements of in-run standards was ±0.2‰ for $\delta^{18}O$ and ±2‰ for $\delta^{2}H$.

The 8-month rainwater record for Liang Luar is too short to accurately document the local rainfall climatology so we use monthly rainfall estimates from the NASA Tropical Rainfall Measuring Mission (TRMM) area-averaged satellite product (3B43 V6, 0.25° x 0.25° grid) for context. TRMM data for 1998–2019 are available through the NASA GES DISC Giovanni online data system (https://giovanni.gsfc.nasa.gov/giovanni/) developed by Acker and Leptoukh[13] and Huffman et al.[14]. We also obtained limited rain-gauge data for western Flores from the Global Historical Climatology Network (GHCN) website[15] (version 4; https://ncei.noaa.gov/data/ghcnm/v4beta/access/). Further context is provided by daily rainfall isotope data available for the neighbouring island of Bali spanning 2002–2009 compiled by the Institute of Observational Research for Global Change/Japan Agency for Marine-Earth Science and Technology, most of which has been described by Kurita et al.[16].

Analysis of modern rainfall seasonality

The TRMM rainfall datasets for 1998–2019 provide a reliable measure of rainfall seasonality in western Flores, and were used as a proxy for the rainfall climatology at Liang Luar (Supplementary Fig. 6). However, the area-averaged rainfall seasonality in the TRMM grid-square containing Liang Luar (centred on 8.625° S) is biased by the high proportion of winter rainfall in southern Flores. To prevent bias, we analysed data for adjacent grid squares centred on 8.375° S. These squares provide a reliable measure of the summer-dominated rainfall seasonality immediately to the north and 'upstream' of Liang Luar.

Supplementary Figure 6 illustrates the good reproducibility of the percentages of summer rainfall contributing to the mean annual rainfall for the five contiguous grid squares nearest to Liang Luar. The summer rainfall percentage (62.3%) recorded at GHCNv4 World Meteorological Organization (WMO) station 97284002 (Papang, 8.45° S, 12.03° E) is in good agreement with that recorded for the adjacent TRMM grid square (62.6%), supporting the use of the TRMM data as a proxy. Based on this result, the pooled mean monthly rainfall for the five TRMM datasets (61.7 ± 0.6%, 2 SE) is used as the contribution of summer rainfall to the amount-weighted mean annual $\delta^{18}O$ of cave dripwaters in the oxygen-isotope mixing model described below in Supplementary Note 3.

Determination of modern mean annual rainfall

The available gridded climate products provide disparate estimates of mean annual rainfall in western Flores,

likely due to the complex island topography. Even at fine scale (0.25–0.5°), the effective resolution of the products is determined by the interpolation algorithm and availability of rain-gauge records for calibration. For example, the rain-gauge record for the 0.25° TRMM grid square containing Liang Luar is from Ruteng, which is at higher elevation (1,200 m.a.s.l.) and receives much more rainfall [3,540 mm annually during 53 complete years for 1915–1976 at GHCNv4 WMO station 97284000 (8.65° S, 120.47° E)]. Thus, the TRMM area-averaged mean annual rainfall of 2,099 mm for the grid square is likely too high (Supplementary Fig. 6a).

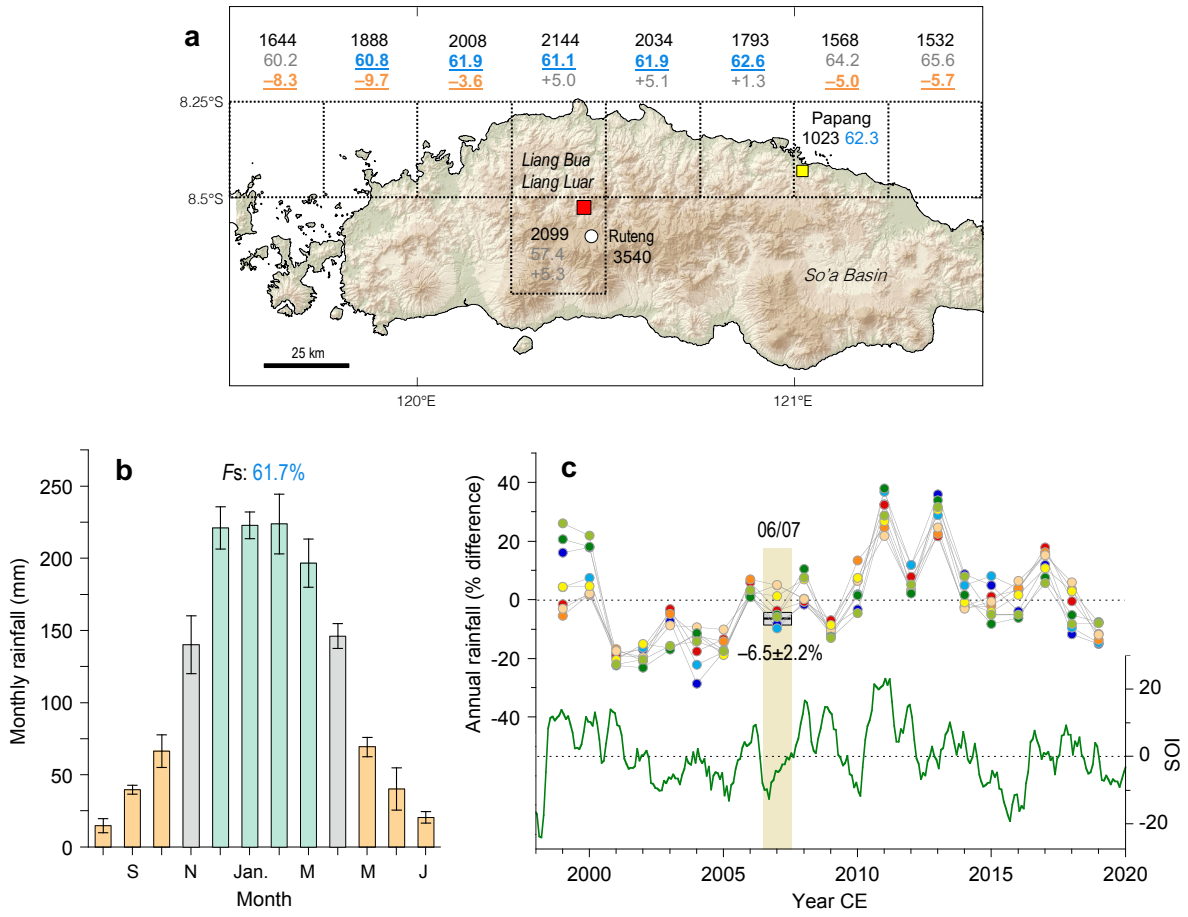

Supplementary Figure 6 | Analysis of rainfall seasonality and mean annual rainfall at Liang Luar. a Locations of rainfall records and summary of rainfall statistics. Black lines indicate 0.25° grid squares for monthly-averaged TRMM satellite records for 1998–2019 (refs.[13,14]). Key rainfall statistics are shown for the eight squares centred on 8.375° S and 119.625–121.375° E used in the analysis: mean annual rainfall (black), summer rainfall percentage (D–M, blue), and percentage difference between annual rainfall in 2006–07 and the long-term mean (orange). For comparison, the yellow square marks the location of rain-gauge data for Papang (WMO station 97284002; 8.45° S, 121.03° E), available from the GHCNv4 website[15] for 1931–1941. The Papang data are in good agreement with TRMM for summer rainfall percentage (blue), but up to ~50% lower than TRMM for mean annual rainfall (black). **b** Modelled rainfall seasonality at Liang Luar. The consistent summer rainfall percentages for the five TRMM records nearest Liang Luar averages 61.7 ± 0.6% (2 SE) (underlined blue values in **a**). The pooled means of the monthly rainfall amounts in these records were used as a proxy for rainfall seasonality at Liang Luar (histogram with black bars showing 2σ range, as scaled below). Grey bars indicate abrupt monsoon transitions in November and April. **c** Determination of mean annual rainfall. In 2006–07, 1,289 mm of rainfall was recorded at Liang Luar, equating to an annual total of 1,313 mm based on the monthly rainfall distribution in **b**. The result was scaled to mean annual rainfall using the difference between the 2006–07 TRMM data and the longer-term TRMM mean for records centred on 8.375° S. Five records converge on slightly drier conditions in 2006–07 (–6.5 ± 2.2%, 2 SE), consistent with a weak El Niño and negative Southern Oscillation Index (SOI, tan bar). Thus, we adjusted the 2006–07 data by +7%. The resulting mean annual rainfall for Liang Luar is 1,405 ± 33 mm (2 SE).

The TRMM rainfall estimate for September 2006–August 2007 is 1,780 mm, whereas only 1,289 mm was recorded for during September 2006–April 2007 at Liang Luar. This equates to an annual total of 1,313 mm (26% less than the TRMM estimate), based on the modelled average monthly distribution of rainfall at Liang Luar (Supplementary Fig. 6b).

Fortunately, the interannual variability across different gridded rainfall products is highly consistent in western Flores. Supplementary Figure 6c shows this strong coherence for 1998–2019 across eight contiguous TRMM records centred on 8.375° S. Therefore, to put the observed rainfall at Liang Luar into context, we scaled the available data for 2006–07 using the difference in mean annual rainfall for 2006–07 (in the TRMM records) and the longer-term TRMM mean.

The year 2006–07 was fairly typical for western Flores in the context of the impact of the El Niño-Southern Oscillation on rainfall. The average difference between the TRMM mean annual rainfall estimates for 2006–07 and the mean for 1998–2019 is –2.6 ± 4.1% (2 SE; range, –9.7 to 5.1%). Five of the records converge on slightly drier conditions in 2006–07 (–6.5 ± 2.2%, 2 SE), consistent with a weak El Niño and negative Southern Oscillation Index. Therefore, to be conservative in our estimates of past aridity, we adjusted the 2006–07 rainfall amount for Liang Luar (1,313 mm) upward by 7% to 1,405 ± 33 mm (2 SE) in accordance with these records. Given the uncertainties in the estimate, we round the results of the analysis to 1,400 mm and allocate 870 mm (62%) to summer (December–March) and 530 mm to 'winter' (April–November) to scale the rainfall history for Liang Luar.

Modern rainfall oxygen-isotope seasonality

We note that the collection of rainfall in an open-air cylinder near Liang Luar entails the risk of day-time evaporation and isotopic enrichment of the samples. However, the $\delta^{18}O$ and $\delta^{2}H$ dataset is orderly and indicates that the daily volumes of collected rainwater were sufficient to mitigate any evaporation effect (Supplementary Fig. 7a). Even dry-season rain-day amounts at Liang Luar between September and November 2006 (n = 15 days) were sizeable, ranging from 3.5 to 40.5 mm d^{-1} (mean, 15.7 mm d^{-1}). The good alignment of $\delta^{18}O$ and $\delta^{2}H$ values for the dry-season samples with the Global Meteoric Water Line indicates that any enrichment of ^{18}O and ^{2}H before collection (or during storage) was negligible (see review by Putnam et al.[17]).

Supplementary Figure 7 shows three key features in the annual cycle of rainfall $\delta^{18}O$ at Liang Luar and in Bali (~700 km west of Flores) that are relevant to the dripwater oxygen-isotope mixing model for the K2 record.

(1) *Dry season uniformity*: The $\delta^{18}O$ of non-convective dry-season rainfall is isotopically uniform at both locations. At Liang Luar, the average $\delta^{18}O$ for non-convective rainfall in September–November 2006 was –1.9‰ VSMOW, similar to the long-term amount-weighted average dry-season value for Bali (–2.6‰ VSMOW for May 2003 to November 2009). The narrow range in $\delta^{18}O$ (–1.7 to –2.6‰) across the large range of the dry-season rainfall in Bali (15–94 mm $month^{-1}$) confirms that a uniform $\delta^{18}O$ value of –2‰ is appropriate for modelling the 40–110 mm $month^{-1}$ range in dry-season rainfall calculated for the K2 record (see Supplementary Note 3).

(2) *Step-changes at monsoon transitions*: Conspicuous shifts to lower (higher) $\delta^{18}O$ occur at the summer monsoon transitions in November (April), signalling the start and end of Intertropical Convergence Zone rainfall associated with deep atmospheric convection. At Liang Luar, the start of the 2006–07 monsoon was accompanied by a ~7‰ decrease in $\delta^{18}O$. These season-specific isotopic domains form the basis for the designation of December–March as summer and April–November as 'winter' in the dripwater mixing model.

(3) *Summer variability*: Although generally low, the $\delta^{18}O$ of daily rainfall in summer at Liang Luar (and at Bali) is highly variable, presumably because of the wide range of daily rainfall amounts and rainfall types in summer. Deep convective rainfall can result in daily mean $\delta^{18}O$ values as low as –15‰ VSMOW, while non-convective rain on very low rainfall days in summer can have positive $\delta^{18}O$ (likely due to enrichment by sub-cloud evaporation[17]). Thus, the dripwater mixing model allows for variation in the $\delta^{18}O$ of convective summer rainfall, in accordance with these 'amount effects'.

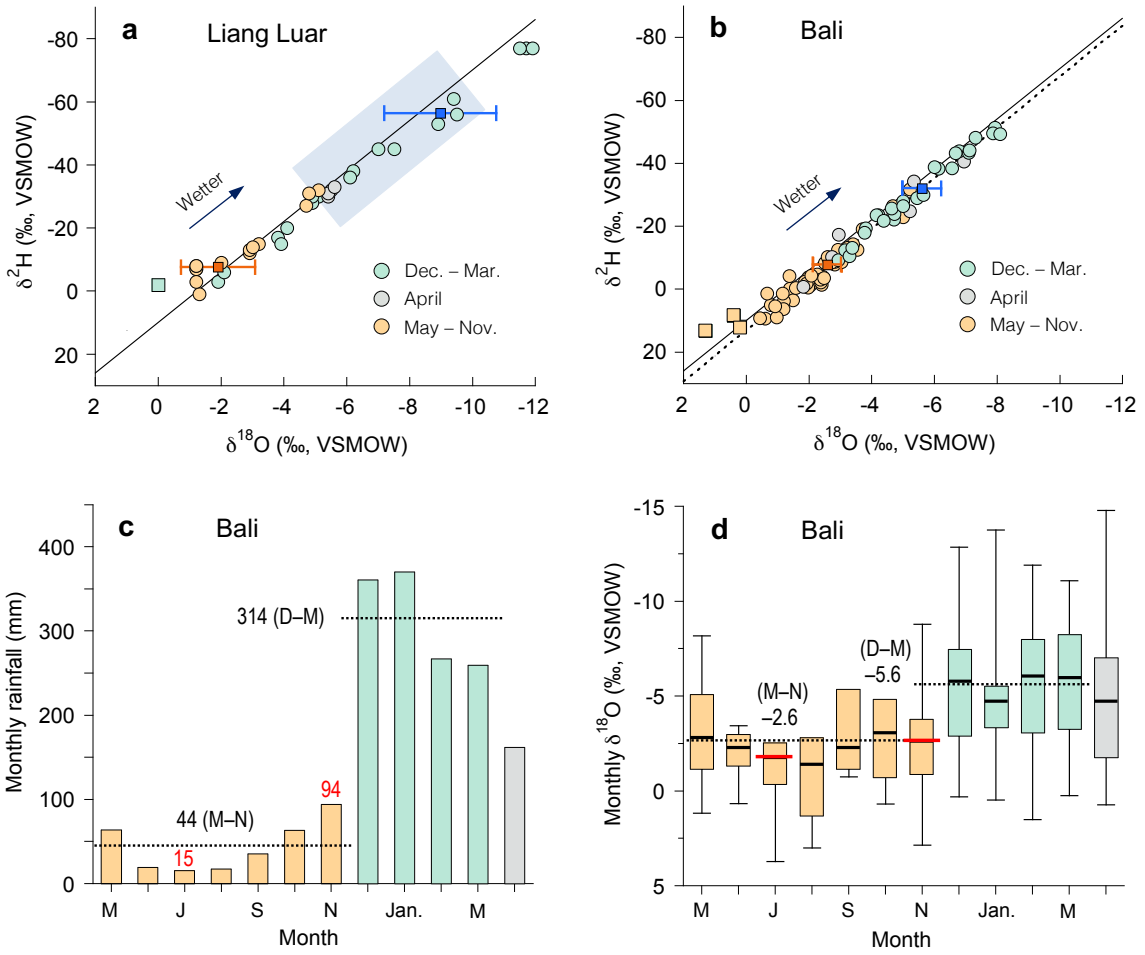

Supplementary Figure 7 | Relationship between rainfall seasonality and δ^{18}O. a Seasonal contrast in δ^{18}O and δ^{2}H at Liang Luar based on 39 rain days between September 2006 and April 2007 (data from Griffiths et al.[4]). The amount-weighted average δ^{18}O values are –9.0 ± 1.8‰ (2 SE) for summer (blue bar) and –1.9 ± 1.2‰ (2 SE) for winter (orange bar). Early April was unusually wet in 2007 and was excluded from the winter analysis (grey circles). Blue shading shows the modelled δ^{18}O range of summer rainfall (–5.0 to –9.6‰) required to produce the range of δ^{18}Oiv in the K2 record (see modelling in Supplementary Note 3). **b–d** Extended analysis of daily rainfall and δ^{18}O measured over seven monsoon cycles in Bali (~700 km west of Flores) for November 2002–November 2009 (based on monitoring data near Denpasar; 8.8 °S, 115.12° E; 1 m.a.s.l.[16]). **b** Cross-plot of monthly average δ^{18}O and δ^{2}H of rainfall. Good alignment of the Bali (and Liang Luar) datasets with the Global Meteoric Water Line (black) indicates minimal ^{18}O enrichment of dry-season rainfall (due to sub-cloud evaporation[17]). The dashed local meteoric water line for Bali is shown because the record exceeds the minimum recommended length of 48 months[17]. Only four rain-day samples (squares) show slightly elevated δ^{18}O; these were small amounts (0.6–13 mm) and of no significance for the amount-weighted averages. **c** Monthly average rainfall based on daily observations near the rainfall isotope monitoring site (WMO station 97230; 8.749 °S, 115.167 °E; GHCNv4[15]). April is wetter in Bali than in Flores and was excluded from the δ^{18}O seasonality analysis. **d** Monthly amount-weighted average δ^{18}O of rainfall (horizontal bars, boxes indicate ranges). Vertical bars indicate range for daily samples. As for Flores, a prominent step-change decrease in δ^{18}O occurs at the summer monsoon transition in November. The amount-weighted average dry-season δ^{18}O is –2.6‰, close to the value of –1.9‰ for Flores. Red bars in June and November show the narrow range in δ^{18}O (–1.7 to –2.6‰) across the full range of dry-season rainfall in Bali (15–94 mm month^{-1} in **c**). Unpublished rainfall isotope data for Bali (January 2007–November 2009) were kindly provided by Professor Naoyuki Kurita (Nagoya University) on behalf of the Institute of Observational Research for Global Change/Japan Agency for Marine-Earth Science and Technology.

Supplementary Note 3. Dripwater oxygen-isotope mixing model and calculation of rainfall amounts

Supplementary Figures 8–11 below summarise our analysis of the relationships between Mg/Ca and $\delta^{18}O_{iv}$ in stalagmite LR09-K2 and rainfall amounts at Liang Luar. Supplementary Figure 8 illustrates an idealised dripwater oxygen-isotope mixing model used to calculate the effect of summer (December–March) rainfall on stalagmite $\delta^{18}O_{iv}$. The summer in-mixing model applies at times with positive covariation of Mg/Ca and $\delta^{18}O_{iv}$ in the K2 record (see Fig. 3). This model forms the basis for the development of a generalised mixing model to calculate the opposing effects of variable amounts of summer and winter (April–November) rainfall on Mg/Ca and $\delta^{18}O_{iv}$ (Supplementary Figs. 9, 10). Supplementary Figure 11 summarises the resulting relationships between Mg/Ca and $\delta^{18}O_{iv}$ and annual, summer and winter rainfall amounts.

Overview and boundary conditions for the summer in-mixing model

To start, the relationship between stalagmite $\delta^{18}O_{iv}$ and summer rainfall was examined in the context of an array of binary dripwater $\delta^{18}O$ mixing lines (Supplementary Fig. 8). Periods of positive covariation of Mg/Ca and $\delta^{18}O_{iv}$ in the K2 record can be described by in-mixing of variable amounts of summer rainfall with a relatively uniform amount of winter rainfall. The following boundary conditions were applied for the summer and winter rainfall contributions to the summer in-mixing model:

(1) The winter baseline was set to 530 mm (the modern average at Liang Luar, Supplementary Fig. 6) with an average $\delta^{18}O$ of –2‰ VSMOW, consistent with the modern-day isotopic average value of non-convective winter rainfall at Liang Luar[4] and at low-elevation sites in the region[16,18] (Supplementary Fig. 7).

(2) The $\delta^{18}O$ of the summer rainfall contribution was allowed to vary inversely with summer rainfall amount, in accordance with rainfall $\delta^{18}O$ data for Liang Luar[4] and elsewhere in southern Indonesia[16].

A generic two end-member oxygen-isotope mass balance equation is sufficient to describe the effect of variable contributions of summer and winter rainfall on stalagmite $\delta^{18}O_{iv}$ at any point within the mixing line array:

$$\delta^{18}O_{iv}\,(\mathrm{VPDB}) = F_w * \delta^{18}O_w\,(\mathrm{VPDBe}) + F_s * \delta^{18}O_s\,(\mathrm{VPDBe}) \quad (1)$$

where $\delta^{18}O_{iv}$ is the amount-weighted annual average $\delta^{18}O$ (VPDB) of stalagmite calcite (corrected for the ice-volume effect); F_w and F_s are the winter and summer rainfall fractions contributing to stalagmite $\delta^{18}O_{iv}$, respectively; and $\delta^{18}O_w$ and $\delta^{18}O_s$ are the amount-weighted average $\delta^{18}O$ values for winter [–2‰ Vienna Peedee Belemnite equivalent (VPDBe)] and summer (VPDBe) rainfall, respectively.

Under summer in-mixing alone, F_s, $\delta^{18}O_s$ (and $\delta^{18}O_{iv}$) in Eq. 1 are co-dependent on the amount of summer rainfall. Thus, each binary mixing line in the array is associated with a specific summer rainfall amount linked to a compatible value of $\delta^{18}O_s$ (Supplementary Fig. 8). The relationship between stalagmite $\delta^{18}O_{iv}$ and summer rainfall in the array was scaled using two conditions:

(1) The modern-day relationship between stalagmite $\delta^{18}O_{iv}$ and rainfall seasonality at Liang Luar was used to scale the wetter interglacial end of the mixing model. In Supplementary Figure 8, the modern mixing line is set to intersect the modern amount-weighted average $\delta^{18}O_{iv}$ (–6.2‰) at $F_s = 0.6214$ (defined by 870/1,400 mm) (Supplementary Figs. 2, 6).

(2) The start point for summer in-mixing was set under the condition of no convective summer monsoon rainfall, such that the $\delta^{18}O$ values of summer and winter rainfall are equal (–2‰) when the average summer rainfall rate (over 4 months) is equal to the average winter rainfall rate (over 8 months). At this point, $F_s = 0.333$ (defined by 265/795 mm) and stalagmite $\delta^{18}O_{iv}$ = –2‰.

We note that Liang Luar stalagmite calcite $\delta^{18}O$ values (on the VPDB scale) are essentially equivalent to rainfall $\delta^{18}O$ values (on the VSMOW scale), and thus comparable for the purposes of the model. Hence, water-isotope $\delta^{18}O$ values are denoted as VPDBe (VPDB equivalent). Previous work has shown that the numerical difference in $\delta^{18}O$ between modern dripwaters and stalagmite calcite at Liang Luar is only 0.6‰. The average $\delta^{18}O$ for dripwaters and pool waters collected at Liang Luar during the 2007 dry season ($n = 7$) is –5.49 ± 0.04‰

VSMOW (± SE)[19]. Similarly, the average $\delta^{18}O$ for modern stalagmite calcite in Liang Luar is –6.06 ± 0.05‰ VPDB (± SE, n = 2 measurements performed at the ANU Research School of Earth Sciences)[6].

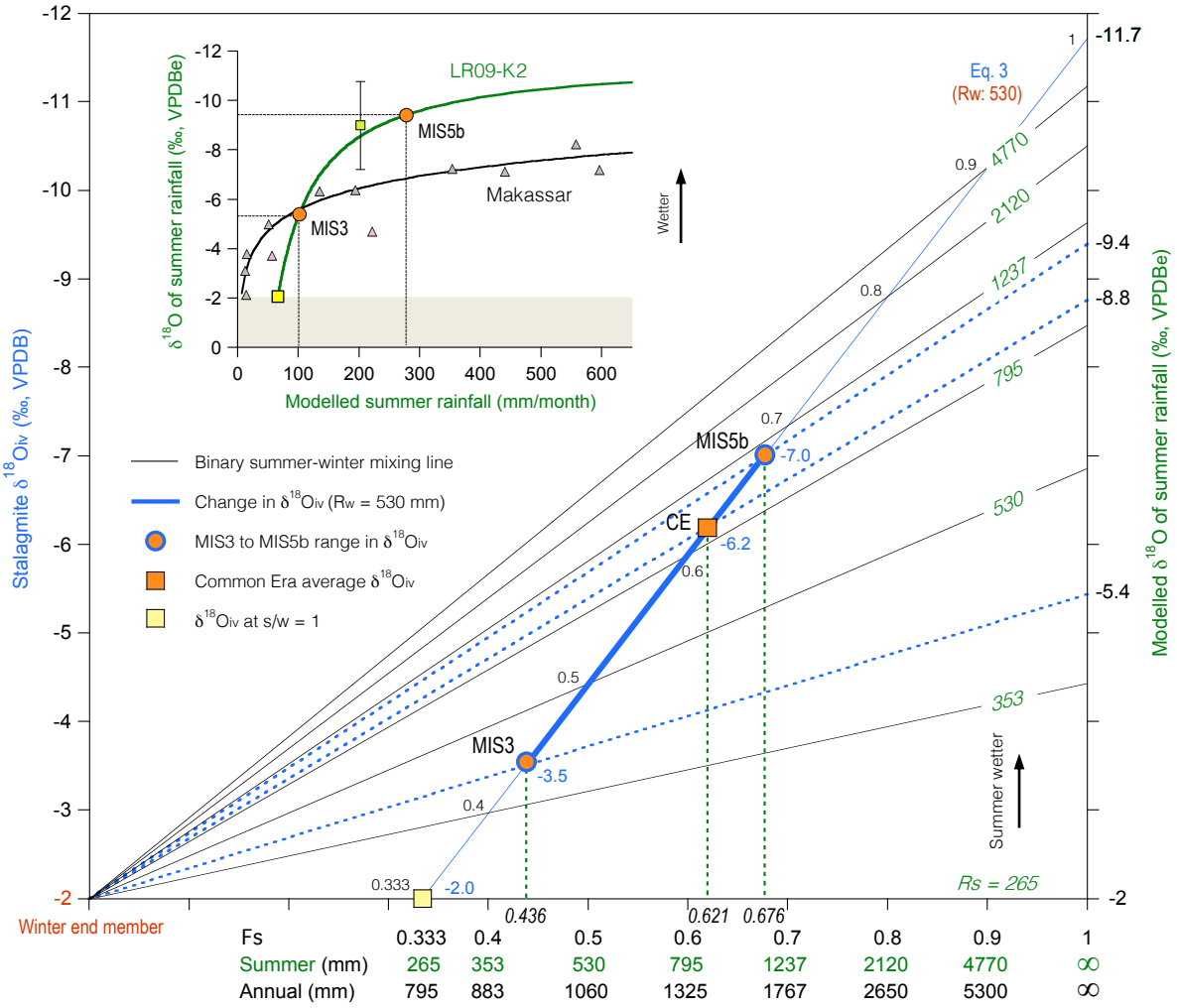

Supplementary Figure 8 | Summer rainfall in-mixing model for stalagmite LR09-K2. The relationship between stalagmite $\delta^{18}O_{iv}$ and summer rainfall for times of positive covariation in Mg/Ca and $\delta^{18}O_{iv}$ is shown in the context of an array of binary dripwater $\delta^{18}O$ mixing lines (grey). The slopes of the lines are set by in-mixing of summer rainfall (R_s) with variable $\delta^{18}O$ (y axis on right) with winter rainfall (R_w) at 530 mm and $\delta^{18}O$ = –2‰. The relationship between $\delta^{18}O_{iv}$ and summer rainfall (bold blue line) is scaled to the modern average stalagmite $\delta^{18}O_{iv}$ (–6.2‰) at F_s = 0.6214 (870/1,400 mm) (orange square). The yellow square marks the start point for measureable summer in-mixing at F_s = 0.333 (265/795 mm) and $\delta^{18}O_{iv}$ = –2‰ (when the summer and winter rainfall rates are equal, s/w = 1). The resulting relationship is: $\delta^{18}O_{iv} = -14.58F_s + 2.86$ (see Eq. 3). Corresponding summer (green) and annual (black) rainfall amounts are scaled to F_s on the x axis. Each binary mixing line is associated with a specific summer rainfall amount (green) linked to a compatible summer rainfall $\delta^{18}O$ value (y axis on right). The inset plot shows the logarithmic relationship between the modelled $\delta^{18}O$ of summer rainfall and modelled summer rainfall amount (green curve, see Eq. 7). The model curve (at –8.8‰) is in close agreement with the modern amount-weighted mean summer rainfall $\delta^{18}O$ value (–9.0 ± 1.8‰, 2 SE, pale green square with bars) recorded at Liang Luar[4]. For comparison, the black curve shows the modern-day logarithmic relationship between mean monthly rainfall and rainfall $\delta^{18}O$ at Makassar, south-western Sulawesi, for November 2002–December 2006 (ref.[16]). Pink triangles mark high $\delta^{18}O$ outliers in October and November (end of the dry season) that were not included in the regression. The results illustrate the sensitivity of rainfall $\delta^{18}O$ to rainfall amount in drier climates, and its limitations under conditions of high rainfall produced by well-organised deep atmospheric convection. The relatively dry hydroclimate at Liang Luar between MIS5b and MIS3 falls well within the model's viable range.

Adjustment of the K2 $\delta^{18}O_{iv}$ (VPDB) values by 0.6‰ to higher would slightly increase the sensitivity of the modelled rainfall amounts to changes in $\delta^{18}O_{iv}$ (Supplementary Fig. 8). Thus, for conservative reconstruction, $\delta^{18}O_{iv}$ values remain on the VPDB scale. Also, we do not correct for the non-identical scaling of delta values on the VPDB and VSMOW scales[20], given that the net distortion is exceedingly small over the 3.5‰ range in $\delta^{18}O_{iv}$ in the K2 record (always <0.11‰). Equation 1 validates the approach, as the modelled $\delta^{18}O$ for modern summer rainfall ($\delta^{18}O_s$, –8.8‰ VPDBe) is in good agreement with the modern amount-weighted mean $\delta^{18}O_s$ at Liang Luar (–9.0 ± 1.8‰ VSMOW, 2 SE)[4], with $\delta^{18}O_{iv}$ and F_s set at –6.2‰ and 0.6214.

Numerical description and validation of the summer in-mixing model

The relationship between stalagmite $\delta^{18}O_{iv}$ and the evolving fractions of summer and winter rainfall in cave dripwaters forms the basis for the calculation of rainfall amount. Based on Supplementary Figure 8, the relationship for in-mixing of summer rainfall (with a set amount of winter rainfall) can be expressed as:

$$\delta^{18}O_{iv} = 2.86F_w - 11.72F_s \quad (2)$$

Substitution of $(1 - F_s)$ for F_w in Eq. 2 yields $\delta^{18}O_{iv}$ as a linear function of F_s:

$$\delta^{18}O_{iv} = -14.58F_s + 2.86 \quad (3)$$

Equation 3 defines the position and slope of the summer rainfall in-mixing line in the mixing line array in Supplementary Figure 8. Recall that the lower limit on F_s is 0.333 under conditions of no convective summer monsoon rainfall (when the summer and winter rainfall rates are equal), and at this point stalagmite $\delta^{18}O_{iv}$ equates to –2‰. Thus Eq. 3 shows, in principle, that the theoretical range for Liang Luar stalagmite $\delta^{18}O_{iv}$ (50-year average) due to summer rainfall alone extends from –2‰ to –11.7‰ (VPDB) for F_s = 0.333 to 1.

The relatively small range in $\delta^{18}O_{iv}$ in the K2 record (–3.5‰ to –7‰) can be produced by a conservative range in summer monsoon rainfall (44–68% of mean annual rainfall). To check the validity of this result, the range of modelled $\delta^{18}O_s$ values required to account for $\delta^{18}O_{iv}$ in the K2 record can be calculated for comparison with observational and palaeo-data for $\delta^{18}O_s$ in the region. First, Eq. 1 is solved for F_s as a function of $\delta^{18}O$:

$$F_s = \frac{\delta^{18}O_{iv} - \delta^{18}O_w}{\delta^{18}O_s - \delta^{18}O_w} \quad (4)$$

Substitution of Eq. 3 into Eq. 4 yields the relationship among $\delta^{18}O_s$, $\delta^{18}O_{iv}$ and $\delta^{18}O_w$ at any point on the summer in-mixing line:

$$\delta^{18}O_s = \frac{\delta^{18}O_{iv}(14.58 - \delta^{18}O_w) - 11.72\delta^{18}O_w}{2.86 - \delta^{18}O_{iv}} \quad (5)$$

Substitution of –2‰ (VPDBe) for $\delta^{18}O_w$ in Eq. 5 yields the relationship between $\delta^{18}O_s$ and $\delta^{18}O_{iv}$:

$$\delta^{18}O_s = \frac{23.44 + 16.58\delta^{18}O_{iv}}{2.86 - \delta^{18}O_{iv}} \quad (6)$$

Note that for the model, $\delta^{18}O_s$ is expressed as a function of the ice-volume corrected $\delta^{18}O_{iv}$, and relative to the $\delta^{18}O$ of modern seawater. Thus, the true values of $\delta^{18}O_s$ would be slightly higher. Equation 6 shows that the –3.5‰ to –7‰ range in $\delta^{18}O_{iv}$ in the K2 record requires mixing lines with summer $\delta^{18}O_s$ values of –5.4‰ to –9.4‰ (Supplementary Fig. 8). The 4‰ range is well within the range of modern-day $\delta^{18}O_s$ at Liang Luar[4] and in southern Indonesia[16]. Further, the result is consistent with the glacial-interglacial range in $\delta^{18}O_{iv}$ in stalagmite records for south-western Sulawesi (~3.5‰), immediately to the north of Flores, where $\delta^{18}O_{iv}$ is controlled almost entirely by summer rainfall[21,22].

The mixing line array also can be checked by comparing the modelled $\delta^{18}O_s$ and modelled summer rainfall with observational data. Substitution of Eq. 3 into Eq. 6 yields the relationship of $\delta^{18}O_s$ to F_s in Eq. 7. Substitution of (R_s / R_s + R_w) for F_s yields $\delta^{18}O_s$ in terms of summer rainfall (R_s), with winter rainfall (R_w) set to 530 mm:

$$\delta^{18}O_s = \frac{4.86}{Fs} - 16.58 = 4.86\left(\frac{Rw}{Rs}\right) - 11.72 = 4.86\left(\frac{530}{Rs}\right) - 11.72 \quad (7)$$

Note that the modelled relationship between $\delta^{18}O_s$ and summer rainfall is not linear; $\delta^{18}O_s$ changes rapidly under drier climates and becomes less sensitive to changes in R_s under wetter conditions (Supplementary Fig. 8 inset). The modern-day relationship between rainfall $\delta^{18}O$ and mean monthly rainfall at Makassar, south-western Sulawesi[16], confirms this non-linear response. The seasonal range in rainfall at Makassar is exceptionally large (0–600 mm month^{-1}) and dominated strongly by changes in convective summer rainfall. The reduction in the rate of change in $\delta^{18}O_s$ as summer rainfall increases lends support to an association between the 'amount effect' and the intensity of convective monsoon rainfall[18,23]. This mechanism would rapidly decrease the $\delta^{18}O$ of rainfall at the onset of atmospheric convection. On the other hand, the physical limit on convective cloud height would ultimately limit the lowering of $\delta^{18}O_s$ during exceptionally wet times. In the case of the K2 record, however, the relatively dry hydroclimate at Liang Luar from 91 to 47 ky BP means that $\delta^{18}O_{iv}$ is sensitive to the model-predicted rainfall amounts.

Generalised mixing model and determination of rainfall amounts

Supplementary Figures 9 and 10 below illustrate the generalised mixing model used to calculate annual, summer and winter rainfall amounts from the K2 Mg-^{18}O record. This model accounts for changes in winter rainfall, with relatively high $\delta^{18}O$, that drive negative covariation of stalagmite Mg/Ca and $\delta^{18}O_{iv}$ (see Fig. 3) and offset $\delta^{18}O_{iv}$ from the idealised summer in-mixing line (where R_w is constant at 530 mm).

The relationship between $\delta^{18}O_{iv}$ and the unique mixture of summer and winter rainfall compatible with each Mg-^{18}O data pair in the K2 record is defined by a binary mixing line within the model array. The generic equation for each mixing line, with F_s expressed as R_s/R_a (where R_a is the mean annual rainfall), is:

$$\delta^{18}O_{iv} = m\left(\frac{Rs}{Ra}\right) - 2 \quad (8)$$

The *y*-intercept for every line is –2‰ (VPDBe), the regional average $\delta^{18}O$ value for non-convective winter rainfall (as defined in Supplementary Fig. 8). Thus, the key step is to identify the values of *m* (line slope), R_s and R_a that bring the calculated value for $\delta^{18}O_{iv}$ into precise alignment with the measured $\delta^{18}O_{iv}$. The identification of compatible binary mixing lines is required for all 893 Mg-^{18}O data pairs in the K2 record.

Importantly, R_s and *m* are co-dependent because they are both defined by an associated $\delta^{18}O$ value at the point where each mixing line intersects the summer rainfall in-mixing line ($\delta^{18}O_{si}$). Therefore, finding the value of $\delta^{18}O_{si}$ that satisfies each Mg-^{18}O data pair is critical for determining R_s. Once R_s is known, R_w is the difference between R_s and R_a, where R_a is the value specific to each Mg-^{18}O data pair (see Eq. 13 below).

To illustrate the approach, Supplementary Figure 9 shows an example of the relationship between the K2 Mg-^{18}O system and R_a, R_s and R_w. The example scenario is based on modern climate conditions at Liang Luar, but with R_w equal to 0 mm (instead of 530 mm) to show the effects of a reduction in winter rainfall. The initial conditions and final conditions for the scenario are:

Modern climate 'start point':		**'End point' at *R*w = 0:**	
$\delta^{18}O_{iv}$:	–6.20‰ (VPDB)	Measured $\delta^{18}O_{iv}$:	–8.76‰ (VPDB)
$\delta^{18}O_{si}$:	–6.20‰ (VPDB)	$\delta^{18}O_{si}$:	–6.20‰ (VPDB)
R_a:	1,400 mm	R_a:	870 mm
R_s:	870 mm (F_s = 0.6214)	R_s:	870 mm (F_s = 1)
R_w:	530 mm	R_w:	0 mm

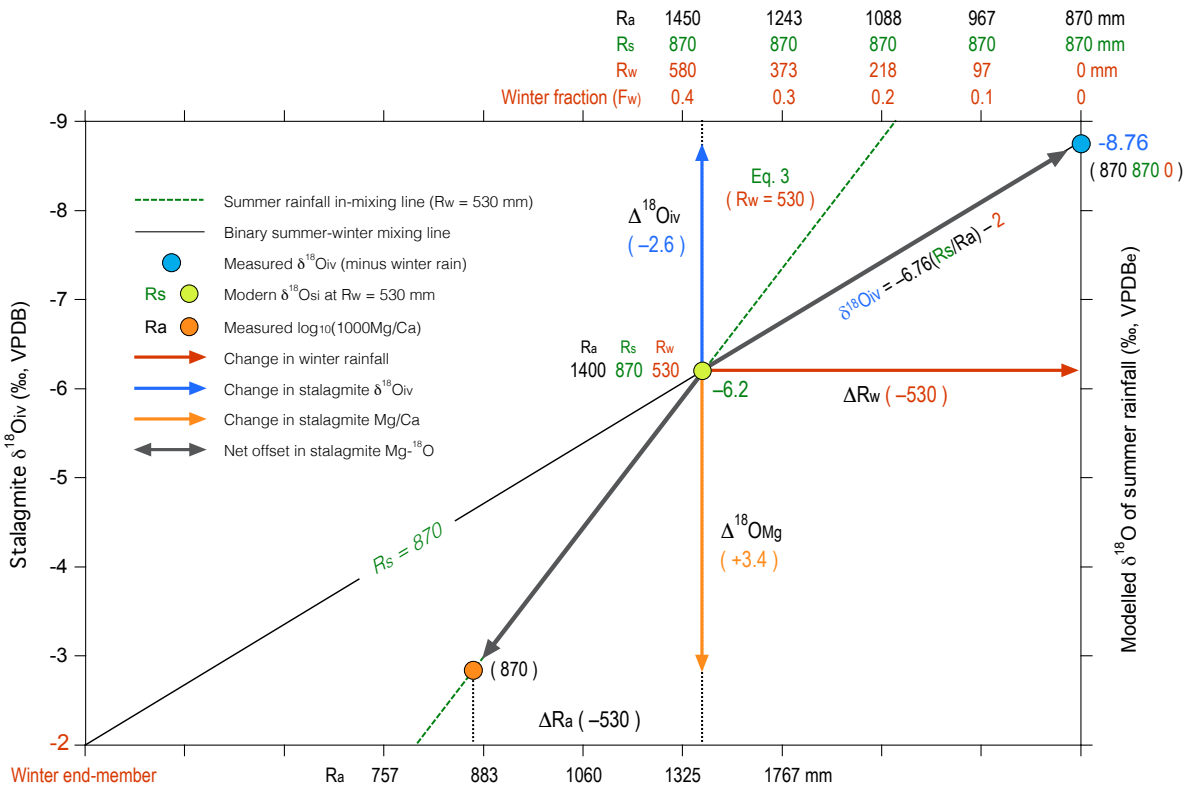

Supplementary Figure 9 | Mg-^{18}O and rainfall systematics for stalagmite LR09-K2. The example is for modern climate at Liang Luar, but with winter rainfall (Rw) at 0 mm to illustrate the effects of a reduction in Rw on Mg/Ca and δ^{18}Oiv. For modern climate conditions, the position of δ^{18}Oiv (–6.2‰) on the summer rainfall in-mixing line (Eq. 3 green line with Rw = 530 mm) is set by the binary mixing line (black) linking Rw (δ^{18}O = –2‰) and the modern summer rainfall (Rs) end member (δ^{18}O = –8.76‰). This point defines δ^{18}Osi (–6.2‰, see Eq. 16), the amount of Rs (870 mm, see Eq. 11), and the binary mixing line slope (–6.76, see Eq. 9). The offset of the measured δ^{18}Oiv along the binary mixing line from the δ^{18}Osi 'start point' is set by the decrease in Rw alone. In this example, when Rw drops to 0 mm the measured δ^{18}Oiv is –8.76‰ (the summer rainfall δ^{18}O value), and Rs and mean annual rainfall (Ra) are both 870 mm. The associated decrease in Ra from 1,400 mm (at the δ^{18}Osi 'start point') to 870 mm (orange circle) is determined by the measured Mg/Ca and Eq. 13 (scaled here to δ^{18}O using the log-linear relationship defined in the main text Fig. 3). The relationship of $\log_{10}$(1000Mg/Ca) to Ra is independent of changes in seasonality, and thus defined by the summer in-mixing line (with Ra scaled on the lower x axis according to Supplementary Fig. 8). The dark orange vector shows the associated change in Rw (ΔRw) scaled on the upper x axis. Grey vectors illustrate how winter rainfall drives δ^{18}Oiv and Mg/Ca in opposite directions from δ^{18}Osi. The vertical blue and orange vectors represent the total offset in δ^{18}O between δ^{18}Oiv and Mg/Ca (6‰), as it would appear in the main text Figures 3 and 4.

The key point of Supplementary Fig. 9 is to show that finding the compatible value of δ^{18}Osi (and associated Rs) that satisfies each Mg-^{18}O data pair is critical to solve Eq. 8. The steps required to identify δ^{18}Osi and the combination of m, Rs and Ra that brings the Eq. 8 solution for δ^{18}Oiv into agreement with the measured δ^{18}Oiv are described below. First, we define m, Rs and Ra in terms of δ^{18}Osi.

The relationship between δ^{18}Osi and Fs in Eq. 3 can be used to derive m in terms of δ^{18}Osi:

$$m = \frac{-14.58(\delta^{18}\mathrm{Osi} + 2)}{\delta^{18}\mathrm{Osi} - 2.86} \quad (9)$$

The calculation of Rs is also based on Eq. 3, with Fs expressed in terms of Rs and Rw:

$$\delta^{18}\mathrm{O_{si}} = -14.58\left(\frac{R_s}{R_s + R_w}\right) + 2.86 \quad (10)$$

Equation 10 serves to scale R_s to $\delta^{18}O_{si}$ along the summer rainfall in-mixing line in Supplementary Figures 8 and 9. Substitution of 530 mm for R_w and rearrangement of Eq. 10 yields R_s as a function of $\delta^{18}O_{si}$:

$$R_s = \frac{1515.8 - 530\delta^{18}\mathrm{O_{si}}}{\delta^{18}\mathrm{O_{si}} + 11.72} \quad (11)$$

Addition of 530 mm (R_w) to Eq. 11 yields R_a:

$$R_a(^{18}\mathrm{O}) = \frac{7727.4}{\delta^{18}\mathrm{O_{si}} + 11.72} \quad (12)$$

Importantly, Eq. 12 provides a means to calibrate the relationship between stalagmite Mg/Ca and R_a, which is independent of changes in seasonality. The log-linear relationship $\delta^{18}O_{iv} = 4.822*\log_{10}(1000\mathrm{Mg/Ca}) - 10.56$ (defined in the main text Fig. 3) is used for the transformation. Substitution of this relationship for $\delta^{18}O_{si}$ in Eq. 12 yields a general equation for calculating R_a for every Mg-^{18}O data pair in the K2 record:

$$R_a = \frac{1602.5}{\log10(1000\mathrm{Mg/Ca}) + 0.2406} \quad (13)$$

The resulting expanded version of Eq. 8 expressed in terms of $\delta^{18}O_{si}$ and R_a is:

$$\delta^{18}\mathrm{O_{iv}} = \frac{-14.58(\delta^{18}\mathrm{O_{si}} + 2)}{\delta^{18}\mathrm{O_{si}} - 2.86} * \left[\frac{\left(\frac{1515.8 - 530\delta^{18}\mathrm{O_{si}}}{\delta^{18}\mathrm{O_{si}} + 11.72}\right)}{R_a}\right] - 2 \quad (14)$$

In this form, Eq. 14 defines the specific value of $\delta^{18}O_{si}$ (and hence m and R_s) required to solve Eq. 8. Therefore, to find the mixing line specific to each Mg-^{18}O data pair we set Eq. 14 to zero and solve for $\delta^{18}O_{si}$ as a function of the measured $\delta^{18}O_{iv}$ and associated R_a (from Eq. 13):

$$0 = \delta^{18}\mathrm{O_{iv}} - \left[\frac{-14.58(\delta^{18}\mathrm{O_{si}} + 2)}{\delta^{18}\mathrm{O_{si}} - 2.86} * \frac{\left(\frac{1515.8 - 530\delta^{18}\mathrm{O_{si}}}{\delta^{18}\mathrm{O_{si}} + 11.72}\right)}{R_a(\mathrm{Mg})} - 2\right] \quad (15)$$

$$\delta^{18}\mathrm{O_{si}} = \frac{R_a(-11.72\delta^{18}\mathrm{O_{iv}} - 23.44) + 15454.8}{R_a\delta^{18}\mathrm{O_{iv}} + 2R_a - 7727.4} \quad (16)$$

R_s can then be calculated from the resulting $\delta^{18}O_{si}$ (using Eq. 11).

The final step is to determine R_w as the difference between R_a and R_s:

$$R_w = R_a - R_s \quad (17)$$

To illustrate the generalised model as applied to stalagmite K2 Mg-^{18}O data pairs, Supplementary Figure 10 below shows a vector analysis of two contrasting winter rainfall scenarios: a 239-mm decrease in R_w during MIS4 (at 66.525 ky BP) and a 261-mm increase during MIS5a (at 76.075 ky BP). These opposing changes in R_w drive stalagmite $\delta^{18}O_{iv}$ in opposite directions away from the summer rainfall in-mixing line. Note that the impact of R_w on Mg/Ca and $\delta^{18}O_{iv}$ varies as a function of mixing line slope.

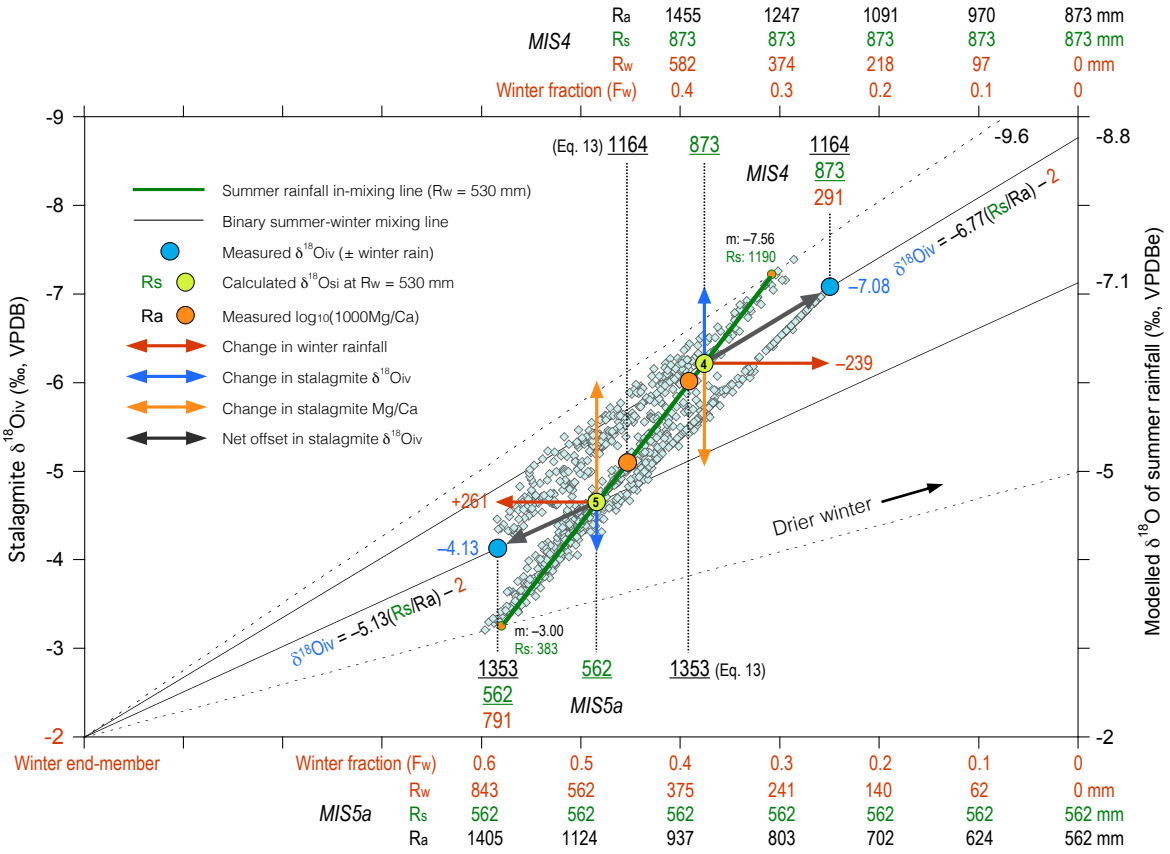

Supplementary Figure 10 | Generalised mixing model for stalagmite LR09-K2. The generalised mixing model accounts for changes in winter rainfall (*R*w) that drive negative covariation of stalagmite Mg/Ca and $\delta^{18}O_{iv}$. Changes in *R*w offset the measured $\delta^{18}O_{iv}$ values (blue diamonds) from the idealised summer in-mixing line (Eq. 3 green line with *R*w constant at 530 mm). The exact position of each $\delta^{18}O_{iv}$ data point in the mixing line array (n = 893 points) is controlled by the change in *R*w along one binary mixing line (grey), each associated with a specific summer rainfall amount (*R*s) and compatible summer rainfall $\delta^{18}O$ value (y axis on right). The resulting $\Delta^{18}O_{iv}/\Delta F$s slopes of the lines change from –3.00 to –7.56 in accordance with the range in *R*s. To account for the effect of these differences on $\delta^{18}O_{iv}$, we identified the specific mixing line slope (Eq. 9), and co-dependent value of $\delta^{18}O_{si}$ (and *R*s) on the summer in-mixing line (Eqs. 16, 17), that reconciled the offset in $\delta^{18}O_{iv}$ from the summer line. To illustrate the method, vector analyses are shown for two contrasting winter rainfall scenarios: a 239-mm decrease in *R*w during MIS4 (the 66.525 ky BP Mg-^{18}O data pair) and a 261-mm increase during MIS5a (the 76.075 ky BP Mg-^{18}O data pair). The grey vectors show how the opposing changes in *R*w drive stalagmite $\delta^{18}O_{iv}$ in opposite directions from the $\delta^{18}O_{si}$ 'start points' (green circles). The x axes highlight the different scales of the changes in *R*w (orange) and *R*a (black) due to the different mixing line slopes for MIS4 (–6.77, upper x axis) and MIS5a (–5.13, lower x axis). Orange circles show the associated (opposing) shifts in mean annual rainfall (*R*a, based on the measured Mg/Ca in Eq. 13) away from the $\delta^{18}O_{si}$ 'start points' along the summer line (scaled to $\delta^{18}O$). Colour-coded text indicates the calculated values of *R*a, *R*s and *R*w that are uniquely compatible with the Mg-^{18}O data pairs defining both scenarios.

The mixing line statistics and values of *R*a, *R*s and *R*w compatible with each Mg-^{18}O data pair in the K2 record are summarised in Supplementary Data 2. Supplementary Figure 11 below illustrates the relationships between *R*a, *R*s and *R*w and the K2 Mg-^{18}O system. The modelled range in *R*a for $\log_{10}$(1000Mg/Ca) values spanning 0.570–1.522 mmol/mol in the K2 record, including variations in *R*w (based on Eq. 13), is 909 mm at 57.375 ky BP (MIS3) to 1977 mm at 78.625 ky BP (MIS5a). The relationship of *R*s and $\delta^{18}O_{iv}$ is shown for times of positive covariation of Mg/Ca and $\delta^{18}O_{iv}$ (based on Eq. 11). The modelled range extends from 378 mm at 55.925 ky BP (MIS3) to 1,255 mm at 90.925 ky BP (MIS5b).

The modelled R_w ranges from 291 mm at 66.525 ky BP (MIS4) to 1,063 mm at 82.325 ky BP (MIS5a), based on the calculated differences between R_a and R_s for each Mg-^{18}O data pair. There is no fixed relationship between R_w and stalagmite $\delta^{18}O_{iv}$ because the impact of R_w on $\delta^{18}O_{iv}$ varies as a function of mixing line slope. However, R_w can be scaled to $\delta^{18}O$ in terms of differences, as follows:

$$\Delta R_w \propto \Delta^{18}O_w \quad (\text{where } \Delta R_w = R_w - 530, \text{ and } \Delta^{18}O_w = \delta^{18}O_{iv} - \delta^{18}O_{si}) \qquad (18)$$

Supplementary Figure 11 shows R_w scaled to the difference between the measured $\delta^{18}O_{iv}$ and the associated value of $\delta^{18}O_{si}$ on the summer in-mixing line ($\Delta^{18}O_w$). The results show that stalagmite $\delta^{18}O_{iv}$ is a factor of ~0.4 less sensitive, on average, to changes in R_w (with constant $\delta^{18}O$) than to changes in R_s (with $\delta^{18}O$ that varies inversely with rainfall amount).

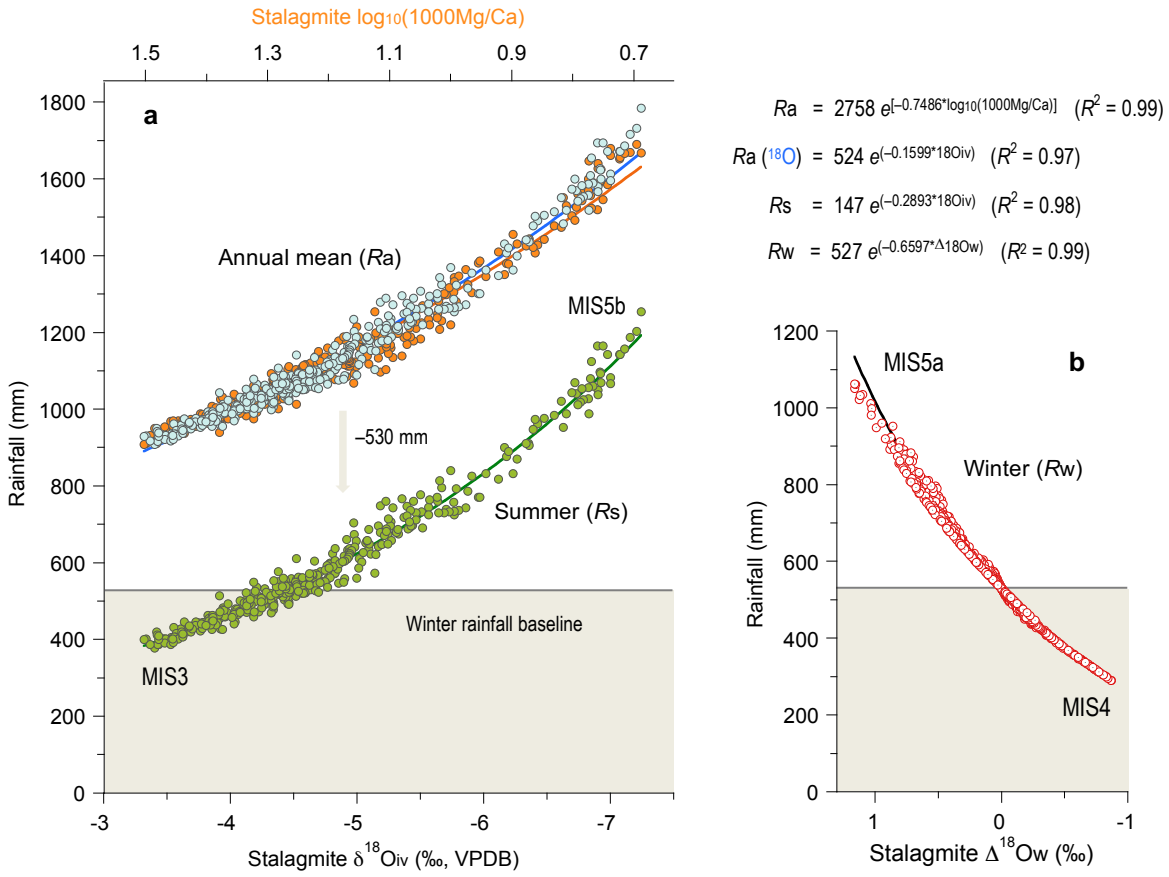

Supplementary Figure 11 | Relationships between stalagmite Mg-^{18}O and annual, summer and winter rainfall at Liang Luar. a Exponential relationships between the stalagmite K2 Mg-^{18}O system and mean annual rainfall (R_a) and summer rainfall (R_s) when winter rainfall (R_w) is constant (530 mm), based on the summer rainfall in-mixing model (Supplementary Fig. 8). Mg/Ca was scaled to $\delta^{18}O_{iv}$ using the log-linear relationship based on the three calibration intervals in the K2 record with positive covariation of Mg/Ca and $\delta^{18}O_{iv}$: 91.375–89.575, 75.475–70.325 and 60.275–46.775 ky BP (see main text Fig. 3). The average absolute difference between R_a(^{18}O) (based on Eq. 12) and R_a (based on Eq. 13) is 38 ± 69 mm (2σ, n = 412 Mg-^{18}O data pairs). The relationship of $\log_{10}$(1000Mg/Ca) and R_a is independent of changes in seasonality and thus represents a general calibration for R_a for every Mg-^{18}O data pair in the K2 record. The lower curve (green) shows the relationship between R_s and stalagmite $\delta^{18}O_{iv}$ (based on Eq. 11) after subtraction of the baseline contribution of winter rainfall (530 mm). **b** Relationship between R_w and the difference between the measured $\delta^{18}O_{iv}$ and associated value of $\delta^{18}O_{si}$ on the summer in-mixing line ($\Delta^{18}O_w$), based on Eq. 18. Marine oxygen-isotope stages (MIS) and associated rainfall amounts are indicated for reference.

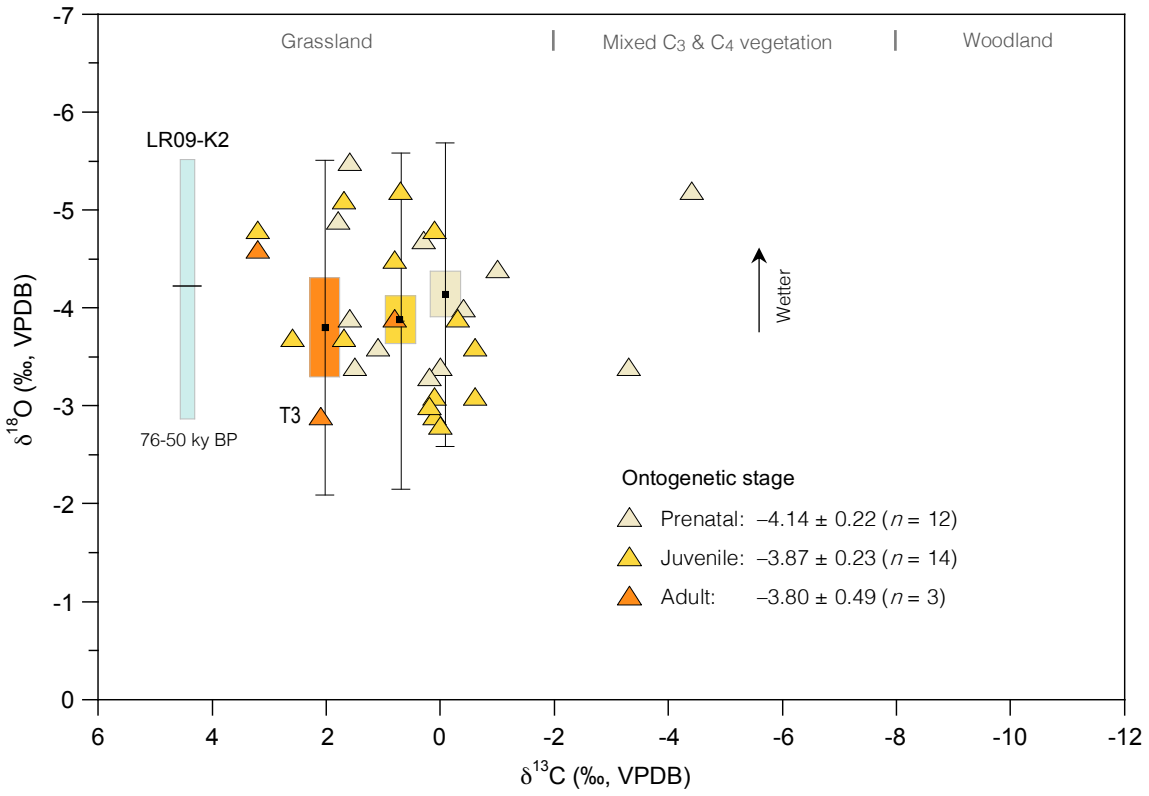

Supplementary Figure 12 | $\delta^{18}O$ and $\delta^{13}C$ in fossil *Stegodon* tooth enamel from Liang Bua at different ontogenetic stages. $\delta^{18}O$ and $\delta^{13}C$ data are shown for the carbonate phase of *S. florensis insularis* tooth enamel formed at prenatal, juvenile and adult ontogenetic stages[24]. "T3" represents an adult molar excavated from tephra T3 at Liang Bua (capping the terminal-stage stratigraphic sequence). Vertical black bars indicate standard deviations (2σ) for each $\delta^{18}O$ dataset. Colour-coded boxes show standard errors of the means. The summary statistics show no significant difference in the mean $\delta^{18}O$ values (±SE) for prenatal, juvenile and adult tooth material. The results demonstrate that the mixed-tooth $\delta^{18}O$ data for Liang Bua can be compared with $\delta^{18}O$ data based exclusively on adult *Stegodon* molar material excavated in the So'a Basin (main text Fig. 6). Blue bar shows the good fit of the range of the Liang Luar stalagmite K2 $\delta^{18}O$ data (mean ±2σ for 76–50 ky BP) and the range of the Liang Bua *Stegodon* tooth $\delta^{18}O$ data (stalagmite $\delta^{18}O$ not corrected for ice-volume effect). The tooth $\delta^{13}C$ values (with the exception of two prenatal samples) indicate that *Stegodon florensis insularis* was primarily a C_4 grazer[24].

Supplementary Table 1: U-Th isotope data for stalagmite LR09-K2

Sample ID	Lab / year	Depth (mm from top)	^{238}U (ppb)	^{232}Th (ppt)	^{230}Th / ^{232}Th (activity)	^{230}Th / ^{238}U (activity)	$\delta^{234}U$* (measured)	^{230}Th age (y) (uncorrected)	^{230}Th age (y)** (corrected)	$\delta^{234}U_{initial}$ (corrected)	^{230}Th age (y BP)*** (corrected)
LR09-K2-M1	UMinn / 2015	35	161.3 ±0.2	198 ±4	948 ±19	0.3790 ±0.0006	57.3 ±1.4	48187 ±146	48152 ±147	66 ±2	**48087 ±147**
LR09-K2-M2	UMinn / 2015	139.5	231.9 ±0.3	164 ±3	1756 ±36	0.4043 ±0.0007	56.7 ±1.6	52328 ±175	52311 ±177	66 ±2	**52246 ±177**
LR09-K2-M3	UMinn / 2015	233	311.4 ±0.4	239 ±5	1661 ±34	0.4147 ±0.0007	51.9 ±1.4	54402 ±174	54381 ±175	61 ±2	**54316 ±175**
LR09-K2-M4	UMinn / 2015	302.5	199.9 ±0.2	85 ±2	2996 ±67	0.4156 ±0.0007	53.0 ±1.3	54477 ±167	54465 ±170	62 ±1	**54400 ±170**
LR09-K2-U02	UMinn / 2013	315.5	176.7 ±0.2	264 ±5	859 ±18	0.4172 ±0.0009	52.9 ±1.6	54755 ±209	54716 ±211	62 ±2	**54653 ±211**
LR09-K2-M5	UMinn / 2015	417	426.0 ±0.6	46 ±1	12136 ±286	0.4302 ±0.0007	49.0 ±1.3	57281 ±178	57277 ±179	58 ±2	**57212 ±179**
LR09-K2-M6	UMinn / 2015	526.5	250.8 ±0.3	129 ±3	2615 ±55	0.4381 ±0.0008	42.8 ±1.7	59165 ±215	59150 ±217	51 ±2	**59085 ±217**
LR09-K2-04	UMelb / 2010	539	440 ±33		1046	0.4417 ±0.0023	48.9 ±2.2	59313 ±451	59274 ±455	58 ±3	**59214 ±455**
LR09-K2-U04	UMinn / 2012	642.5	493.0 ±0.9	146 ±3	4602 ±96	0.4437 ±0.0009	48.0 ±2.0	59742 ±245	59732 ±246	57 ±2	**59670 ±246**
LR09-K2-U06	UMinn / 2012	707.5	265.2 ±0.3	19 ±1	19073 ±1231	0.4515 ±0.0008	49.6 ±1.5	61010 ±211	61005 ±211	59 ±2	**60943 ±211**
LR09-K2-U10	UMinn / 2012	805	161.7 ±0.2	597 ±12	387 ±8	0.4640 ±0.0010	49.0 ±1.9	63336 ±269	63235 ±277	59 ±2	**63173 ±277**
LR09-K2-U17	UMinn / 2012	838.5	52.1 ±0.1	116 ±3	656 ±15	0.4757 ±0.0022	46.2 ±2.5	65771 ±482	65709 ±488	56 ±3	**65647 ±488**
LR09-K2-U19	UMinn / 2013	847	56.2 ±0.1	94 ±2	879 ±21	0.4794 ±0.0016	47.1 ±1.5	66389 ±349	66343 ±355	57 ±2	**66280 ±355**
LR09-K2-U21	UMinn / 2012	852	112.2 ±0.1	10 ±1	17498 ±1959	0.4910 ±0.0012	46.8 ±1.7	68636 ±305	68637 ±305	57 ±2	**68575 ±305**
LR09-K2-M7	UMinn / 2015	853.5	124.2 ±0.1	6 ±1	29195 ±3248	0.4913 ±0.0009	46.0 ±1.7	68775 ±263	68775 ±263	56 ±2	**68710 ±263**
LR09-K2-05	*UMelb / 2010*	*858*	*164 ±12*		*2783*	*0.4922 ±0.0028*	*50.4 ±2.2*	*68513 ±589*	*68506 ±592*	*61 ±3*	***68446 ±592***
LR09-K2-U25	UMinn / 2012	872.5	137.9 ±0.2	35 ±1	6063 ±213	0.4992 ±0.0010	45.6 ±1.9	70362 ±295	70354 ±297	56 ±2	**70292 ±297**
LR09-K2-M8	UMinn / 2015	887.5	184.6 ±0.2	68 ±1	4189 ±92	0.4998 ±0.0008	42.3 ±1.6	70819 ±252	70809 ±253	52 ±2	**70744 ±253**
LR09-K2-U27	UMinn / 2012	900	124.7 ±0.1	47 ±1	4141 ±126	0.5041 ±0.0011	49.2 ±1.7	70956 ±298	70949 ±300	60 ±2	**70887 ±300**
LR09-K2-M9	*UMinn / 2015*	*917.5*	*136.9 ±0.2*	*33 ±1*	*6349 ±191*	*0.4991 ±0.0009*	*42.3 ±1.8*	*70669 ±263*	*70662 ±263*	*52 ±2*	***70597 ±263***
LR09-K2-M10	UMinn / 2015	938.5	216.6 ±0.3	9 ±1	36166 ±2184	0.5007 ±0.0010	41.8 ±1.5	71052 ±276	71048 ±276	51 ±2	**70983 ±276**
LR09-K2-06	UMelb / 2010	940	230 ±17		10030	0.5039 ±0.0020	46.4 ±2.1	71206 ±465	71205 ±465	57 ±3	**71145 ±465**
LR09-K2-M11	UMinn / 2015	993.5	131.5 ±0.2	6 ±1	33479 ±2711	0.5074 ±0.0009	44.7 ±1.5	72083 ±265	72083 ±265	55 ±2	**72018 ±265**
LR09-K2-M12	UMinn / 2015	1048	143.4 ±0.2	27 ±1	8394 ±249	0.5117 ±0.0009	44.9 ±1.7	72929 ±277	72924 ±278	55 ±2	**72859 ±278**
LR09-K2-M13	UMinn / 2015	1073.5	142.9 ±0.1	9 ±1	26866 ±2360	0.5290 ±0.0009	39.2 ±1.6	77138 ±290	77136 ±291	49 ±2	**77071 ±291**
LR09-K2-M14	UMinn / 2015	1104	102.1 ±0.1	33 ±1	5143 ±143	0.5425 ±0.0011	38.7 ±1.7	80087 ±342	80077 ±343	48 ±2	**80012 ±343**
LR09-K2-M15	UMinn / 2015	1133.5	97.6 ±0.1	5 ±1	36192 ±4099	0.5479 ±0.0009	40.1 ±1.4	81084 ±289	81084 ±290	50 ±2	**81019 ±290**
LR09-K2-07	UMelb / 2010	1150	190 ±14		2833	0.5641 ±0.0033	42.8 ±2.5	84315 ±823	84300 ±830	54 ±3	**84240 ±830**
LR09-K2-M16	UMinn / 2015	1152	182.2 ±0.2	2 ±1	132884 ±34774	0.5635 ±0.0009	42.0 ±1.2	84287 ±284	84287 ±284	53 ±2	**84222 ±284**
LR09-K2-M17	UMinn / 2015	1208	156.3 ±0.1	2 ±1	156194 ±60339	0.5731 ±0.0009	41.7 ±1.4	86507 ±309	86507 ±309	53 ±2	**86442 ±309**
LR09-K2-08	UMelb / 2010	1261	128 ±10		1777	0.5813 ±0.0032	39.0 ±2.5	88785 ±849	88760 ±854	50 ±3	**88700 ±854**

Supplementary Table 1 (continued)

Sample ID	Lab / year	Depth (mm from top)	^{238}U (ppb)	^{232}Th (ppt)	^{230}Th / ^{232}Th (activity)	^{230}Th / ^{238}U (activity)	$\delta^{234}U$* (measured)	^{230}Th age (y) (uncorrected)	^{230}Th age (y)** (corrected)	$\delta^{234}U_{initial}$ (corrected)	^{230}Th age (y BP)*** (corrected)
LR09-K2-M18	UMinn / 2015	1278.5	220.5 ±0.2	92 ±2	4325 ±91	0.5860 ±0.0008	39.4 ±1.4	89835 ±310	89824 ±312	51 ±2	**89759 ±312**
LR09-K2-M19	*UMinn / 2015*	*1308*	*182.8 ±0.2*	*219 ±4*	*1516 ±31*	*0.5913 ±0010*	*40.6 ±1.7*	*90906 ±344*	*90873 ±345*	*53 ±2*	***90808 ±345***
LR09-K2-09	UMelb / 2010	1408	251 ±19		428	0.5929 ±0.0020	42.1 ±2.1	91068 ±592	90952 ±599	54 ±3	**90892 ±599**
LR09-K2-M20	UMinn / 2015	1526	252.1 ±0.3	111 ±2	4175 ±88	0.5949 ±0.0010	44.5 ±1.5	91185 ±349	91170 ±353	58 ±2	**91105 ±353**

U decay constants: $\lambda_{238} = 1.55125 \times 10^{-10}$ (ref. 25) and $\lambda_{234} = 2.82206 \times 10^{-6}$ (ref. 26). Th decay constant: $\lambda_{230} = 9.1705 \times 10^{-6}$ (ref. 26).

*$\delta^{234}U = (^{234}U/^{238}U_{activity} - 1) \times 1000$. $\delta^{234}U_{initial}$ was calculated based on ^{230}Th age (T) as follows: $\delta^{234}U_{initial} = \delta^{234}U_{measured} \times e^{\lambda 234 \times T}$.

**Corrected ^{230}Th ages are based on the initial $^{230}Th/^{232}Th$ activity value of 0.82 ± 0.41. This is the value for a material at secular equilibrium, with the bulk earth $^{232}Th/^{238}U$ value of 3.8. Initial $^{230}Th/^{232}Th$ uncertainty is arbitrarily set at 50%. Corrections were applied using the initial Th correction equation of Hellstrom (ref. 27).

***BP stands for before present, where present is defined as the year 1950 CE.

All uncertainties are quoted at 2σ. The three dates in italics are outliers that were not used in the final age-depth model.

Supplementary References

1. Bronk Ramsey, C. Deposition models for chronological records. *Quat. Sci. Rev.* **27**, 42–60 (2008).
2. Bronk Ramsey, C. & Lee, S. Recent and planned developments of the program OxCal. *Radiocarbon* **55**, 720–730 (2013).
3. Scroxton, N. *et al.* Antiphase response of the Indonesian-Australian monsoon to millennial-scale events of the last glacial period. *Sci. Rpt.* 1**2**, 21512, doi.org/10.1038/s41598-022-25810-1 (2022).
4. Griffiths, M. L. *et al.* Increasing Australian-Indonesian monsoon rainfall linked to early Holocene sea-level rise. *Nat. Geosci.* **2**, 636–639 (2009).
5. Lewis, S. C. *et al.* High-resolution stalagmite reconstructions of Australian-Indonesian monsoon rainfall variability during Heinrich Stadial 3 and Greenland Interstadial 4. *Earth Planet. Sci. Lett.* **303**, 133–142 (2011).
6. Ayliffe, L. K. *et al.* Rapid interhemispheric climate links via the Australasian monsoon during the last deglaciation. *Nat. Commun.* **4**, 2908, doi:10.1038/ncomms3908 (2013).
7. Griffiths, M. L. *et al.* Australasian monsoon response to Dansgaard-Oeschger event 21 and teleconnections to higher latitudes. *Earth Planet. Sci. Lett.* **369-370**, 294–304 (2013).
8. Sinclair, D. *et al.* Magnesium and strontium systematics in tropical speleothems from the Western Pacific. *Chem. Geol.* **294-295**, 1–17 (2012).
9. Huang, Y. & Fairchild, I. J. Partitioning of Sr^{2+} and Mg^{2+} into calcite under karst-analogue experimental conditions. *Geochim. Cosmochim. Acta* **65**, 47–62 (2001).
10. Wassenburg, J. A. *et al.* Calcite Mg and Sr partition coefficients in cave environments: Implications for interpreting prior calcite precipitation in speleothems. *Geochim. Cosmochim. Acta* **269**, 581–596 (2020).
11. Kulp, J. L., Turekian, K. & Boyd, D. W. Strontium content of limestones and fossils. *Bull. Geol. Soc. Amer.* **63**, 701–716 (1952).
12. Lea, D. W., Pak, D. K. & Spero, H. J. Climate impact of Late Quaternary equatorial Pacific sea surface temperature variations. *Science* **289**, 1719–1724 (2000).
13. Acker, J. G. & Leptoukh, G. Online analysis enhances use of NASA earth science data. *Eos* **88**, doi:10.1029/2007EO020003 (2007).
14. Huffman, G. *et al.* The TRMM multisatellite precipitation analysis (TMPA): Quasi-global, multiyear, combined-sensor precipitation estimates at fine scales. *J. Hydrometeorol.* **8**, 38–55 (2007).
15. Lawrimore, J. H. *et al.* Global Historical Climatology Network - Monthly (GHCN-M) Version 4. NOAA National Centers for Environmental Information. https://doi.org/10.7289/V5X34VDR (2011).
16. Kurita, N., Ichiyanagi, K., Matsumoto, J., Yamanaka, M. D. & Ohata, T. The relationship between the isotopic content of precipitation and the precipitation amount in tropical regions. *J. Geochem. Explor*. **102**, 113–122 (2009).
17. Putman, A. L., Fiorella, R. P., Bowen, G. J. & Cai, Z. A global perspective on local meteoric water lines: meta-analytic insight into fundamental controls and practical constraints. *J. Water Resour. Res.* **55**, 6896–6910 (2019).
18. Permana, D. S., Thompson, L. G. & Setyadi, G. Tropical West Pacific moisture dynamics and climate controls on rainfall isotopic ratios in southern Papua, Indonesia. *J. Geophys. Res. Atmos.* **121**, 2222–2245 (2016).
19. Griffiths, M. L. *et al.* Younger Dryas–Holocene temperature and rainfall history of southern Indonesia from $\delta^{18}O$ in speleothem calcite and fluid inclusions. *Earth Planet. Sci. Lett.* **295**, 30–36 (2010).
20. Coplen, T. B., Kendall, C. & Hopple, J. Comparison of stable isotope reference samples. *Nature* **302**, 236–238 (1983).
21. Krause, C. E. *et al.* Spatio-temporal evolution of the Australasian monsoon hydroclimate over the last 40,000 years. *Earth Planet. Sci. Lett.* **513**, 103–112 (2019).

22. Kimbrough, A. K. *et al.* Multi-proxy validation of glacial-interglacial rainfall variations in southwest Sulawesi. *Commun. Earth Environ*. **4**, 210, doi.org/10.1038/s43247-023-00873-8 (2023).

23. Cai, Z. & Tian, L. Atmospheric controls on seasonal and interannual variations in the precipitation isotope in the East Asian Monsoon region. *J. Climate* **29**, 1339–1352 (2016).

24. Puspaningrum, M. R. *Proboscidea as Palaeoenvironmental Indicators in Southeast Asia*. PhD thesis, School of Earth and Environmental Sciences, University of Wollongong, 2016. https://ro.uow.edu.au/theses/4944.

25. Jaffey, A. H., Flynn, K. F., Glendenin, L. E., Bentley, W. C. & Essling, A. M. Precision measurements of half-lives and specific activities of ^{235}U and ^{238}U. *Phys. Rev. C* **4**, 1889–1906 (1971).

26. Cheng, H. *et al.* Improvements in ^{230}Th dating, ^{230}Th and ^{234}U half-life values, and U-Th isotopic measurements by multi-collector inductively coupled plasma mass spectrometry. *Earth Planet. Sci. Lett.* **371**, 82–91 (2013).

27. Hellstrom, J. U-Th dating of speleothems with high initial ^{230}Th using stratigraphical constraint. *Quat. Geochron.* **1**, 289–295 (2006).